Nanomechanics: Mechanical response analysis of semiconductor GaAs nanowires by using finite element method and x-ray diffraction techniques

Dissertation
zur Erlangung des Grades eines Doktors der Naturwissenschaften
(Dr. rer. nat)

vorgelegt von

M.Sc. TASEER ANJUM

eingereicht am 13.01.2021 bei der Naturwissenschaftlich-Technischen Fakultät
der Universität Siegen

PRINTED ON AGING RESISTANT, WOOD-FREE AND ACID-FREE PAPER.

Gutachter:

Prof. Dr. Christian Gutt	Universität Siegen
Dr. Anthony Ayari	CNRS Université de Lyon

Prüfer:

Prof. Dr. Thorsten Feldmann	Universität Siegen
Dr. Lisa Michez	CINaM Université d'Aix-Marseille
Prof. Dr. Olivier Thomas	Université d'Aix-Marseille
Dr. Thomas Walter Cornelius	CNRS Université d'Aix-Marseille
Prof. Dr. Ullrich Pietsch	Universität Siegen

Tag der mündlichen Prüfung: 08.04.2021

Zusammenfassung

In den letzten zwei Jahrzehnten wurden durch die Integration von quasi eindimensionalen Nanodrähten enorme Fortschritte bei der Miniaturisierung von opto-elektronischen Bauelementen und sensorbasierten nano-elektromechanischen Systemen erzielt. Für die Entwicklung von Nanodraht basierten Bauelementen der nächsten Generation ist es unerlässlich, die zugrundeliegenden Deformationsmechanismen und deren Mechanik zu untersuchen.
Die vorliegende Arbeit demonstriert die Analyse des mechanischen Verhaltens von Halbleiter Nanodrähten aus Galliumarsenid (GaAs), die mittels Molekularstrahlepitaxie auf Siliziumsubstrat gewachsen sind. Das mechanische Verhalten der Nanodrähte wurde durch in-situ Biegeversuche im Rasterelektronenmikroskop und in Kombination mit Röntgenbeugung untersucht. Infolge der rassanten Entwicklung von Röntgenfokussieroptiken stehen inzwischen an verschiedenen Synchrotronanlagen nanometergroße Röntgenstrahlen zur Verfügung, die es ermöglichen, einen einzelnen Nanodraht zu untersuchen
Das erste Ziel dieses Manuskripts war es, die Auswirkung einer systematischen dynamischen Belastung, d.h. elektromechanisch induzierter Vibrationen, auf einzelne Nanodrähte mit Hilfe der Bragg Beugungsabbildung zu untersuchen. Die parametrische Studie wurde entweder durch die Variation der Amplitude der Resonanz oder der Verweilzeit durchgeführt. Das ex-situ-Experiment, das die kristalline Struktur und die Phasen dieser vibrierenden NWs untersuchen sollte, war für März 2020 geplant, aber aufgrund der Ausbreitung der COVID-19-Pandemie wurde das Experiment von der Synchrotronanlage abgesagt.
Das zweite Ziel dieser Arbeit war es, die anelastische Dehnungsrelaxation der Nanodrähte zu identifizieren, die als direkte Folge von Cantilever-Biegeversuchen und Knickversuchen an freistehenden Be-dotierten GaAs-Nanodrähten beobachtet wurde. Die anelastische Dehnung wurde mit Hilfe eines digitalen Bildkorrelationsalgorithmus abgeleitet. Die Ergebnisse wurden mit FEM-Simulationen unter Berücksichtigung eines Systems von hochgradig gekoppelten nichtlinearen partiellen Differentialgleichungen verglichen. Die Übereinstimmung zwischen FEM-Simulationen und gemessenen Daten bringen die anelastische Relaxation schlüssig mit dem "Gorsky-Effekt" in Nanodrähten in Verbindung.
Be-dotierte GaAs-Nanodrähte wurden weiter in der lateralen Dreipunkt-Biegekonfiguration mit Hilfe des Rasterkraftmikroskops für in-situ nanofokussierte Röntgenbeugung an der Beamline P23 untersucht. Die Biegung der Nanodrähte wurde durch die laterale Bewegung des Rasterkraftmikroskops induziert und in-situ mittels nanofokussierte Röntgenbeugung detektiert. Die Nanodrähte zeigten elastische Deformation, plastische Deformation und eine zeitabhängige anelastische Relaxation. Die anelastische Relaxation hat einen Diffusionskoeffizienten von $2.71 \times 10^{-13} cm^2/s$, was mit dem FEM Modell übereinstimmt und auf das Vorhandensein eines durch den "Gorsky-Effekt" angetriebenen Mechanismus hinweist.

Abstract

During the last two decades, tremendous advances have been made in the miniaturization of opto-electronic devices and sensor-based nano-electromechanical systems by the integration of quasi one-dimensional nanowires. For the development of future generation nanowire-based devices, it is essential to investigate the underlying deformation mechanisms and their mechanics
The present work focuses on the mechanical response analysis of semiconductor gallium arsenide (GaAs) nanowires grown on silicon substrate via molecular beam epitaxy. The mechanical behavior of the nanowires is characterized via in-situ bending tests in a scanning electron microscope and in combination with x-ray diffraction. With the major development of x-ray focusing optics, sub-100 nm sized beams are readily available at synchrotron facilities enabling the study of single nanowires.
The first aim of this work is to investigate the impact of systematic dynamic loading, i.e., electromechanically induced vibrations on single nanowires by using Bragg diffraction imaging. A parametric study is carried out either by varying the amplitude of the vibration or the dwell time. The ex-situ experiment, planned to examine the crystalline structure of these vibrated NWs, was planned for March 2020, but due to the COVID-19 pandemic spread, the experiment has been shifted to a later time by the synchrotron facility.
The second aim of this work is to identify the anelastic strain relaxation of the nanowires which was observed as a direct consequence of cantilever bending tests and buckling tests on free standing Be-doped GaAs nanowires. The anelastic strain is derived by using a digital image correlation algorithm. The results are compared with FEM simulations used to solve a system of highly coupled nonlinear partial differential equations (elasticity and diffusion). The agreement between FEM simulations and measured data conclusively relate the anelastic relaxation in the investigated nanowires to the Gorsky effect, i.e. the coupling between point defects diffusion and stress gradient.
Be doped GaAs nanowires are further examined in the lateral three-point bending configuration by employing the Scanning Force Microscope for in situ Nanofocused X-ray diffraction (SFINX) and x-ray diffraction at beamline P23 at PETRA III. The bending of the nanowires was induced by the lateral movement of the tip of SFINX . The nanowires demonstrate elastic deformation, plastic deformation, and time-dependent anelastic relaxation. The anelastic relaxation yields a diffusion coefficient of $2.71 \times 10^{-13} cm^2/s$ and is consistent with a Gorsky effect.

Contents

1 Introduction 1
1.1 Mechanical properties at nanoscale 1
1.2 State of the art nanomechanics 2
1.3 Thesis Structure 8

2 Semiconductor Nanowires 10
2.1 Epitaxy and crystal growth techniques 10
2.2 Be-doped GaAs nanowires 17
2.3 Elastic properties of GaAs 18

3 Kinematic X-ray Diffraction 21
3.1 Crystal planes and reciprocal lattice 22
3.2 X-ray diffraction 24
3.3 Bragg Coherent Diffraction Imaging 27
3.4 Scanning x-ray diffraction microscopy 30

4 Experimental methods 32
4.1 Dual Beam Focused Ion Beam / Scanning Electron Microscopy (FIB/SEM) system . . 32
4.2 Scanning force microscopy of *in-situ* nano-focused X-ray diffraction 34
4.3 P23 beamline at PETRAIII 37

5 Electromechanical Resonance In Nanowires 38
5.1 Fundamental theory of Resonance 39
5.2 Damping and its impact on quality factor 41
5.3 Electromechanical resonance in FIB/SEM 44

6 Anelasticity In Semiconductor Nanowires 49
6.1 Anelasticity in semiconductor nanowires 50
6.2 Anelasticity tests in FIB/SEM system 51
6.3 Mathematical Modeling 57
6.4 Finite element method modelling 62
6.5 Results and discussion 67

7 Three point bending test on Be doped GaAs nanowires 71
7.1 Introduction and objective 71
7.2 Sample preparation: Be-doped GaAs Nanowires 72
7.3 Lateral three-point bending test by symmetric X-ray diffraction experiment 72

7.4 Results and postmortem of nanowires in FIB/SEM 74
8 Conclusion **85**
References **99**

Publications

PAPER I

Ali Al Hassan, Jonas Lähnemann, Arman Davtyan, Mahmoud Al-Humaidi, Jesús Herranz, Danial Bahrami, **Taseer Anjum**, Florian Bertram, Arka Bikash Dey, Lutz Geelhaar and Ullrich Pietsch. **Beam damage of single semiconductor nanowires during X-ray nano beam diffraction experiments.** *Journal of Synchrotron Radiation,* 2020 DOI

PAPER II

A. Davtyan, D. Kriegner, V. Holý, A. AlHassan, R. B. Lewis, S. McDermott, L. Geelhaar, D. Bahrami, **T. Anjum**, Z. Ren, C. Richter, D. Novikov, J. Müller, B. Butz and U. Pietsc. *Journal of Applied Crystallography*, 2020 **X-ray diffraction reveals the amount of strain and homogeneity of extremely bent single nanowires.** DOI

PAPER III

AlHassan, Ali; Salehi, Waheed; Lewis, Ryan; **Anjum, Taseer**; Sternemann, Christian; Geelhaar, Lutz; Pietsch, Ullrich. **Transition from elastic to plastic strain release in core-shell nanowires revealed by in-plane X-ray diffraction.** *Submitted*.

PAPER IV

Bahrami, Danial; Al Hassan, Ali; Davtyan, Arman; Zhe, Ren; **Anjum, Taseer**; Herranz, Jesus; Geelhaar, Lutz; Novikov, Dmitri; Timm, Rainer; Pietsch, Ullrich. **Impact of electrical current on single GaAs nanowire structure.** *Submitted*.

Listing of figures

1.1 **a.** Scanning electron micrograph of a SiGe island. **b.** Schematic illustration of the mechanical loading of a SiGe island using the AFM-tip and simultaneous X-ray diffraction. **c.** X-ray diffraction patterns for 6 consecutive pressures applied on an individual SiGe island. The Si (004) and SiGe Bragg reflections are marked by arrows while the CTRs originating from the island side facets are highlighted by black lines, and the substrate CTR is encircled. **d.** Normalized resonance frequencies of the AFM tuning fork. The resonance curves corresponding to the diffraction maps from panel **c.** are indicated by Roman numerals I to VI. **e.** Variation of the SiGe island lattice parameter (red) and the tuning fork resonance frequency as a function of the sample displacement Δz. Taken from Refs.[1] 4

1.2 **a.** SEM image of Au nano-crystal prepared by dewetting of a 45[nm] Au thin film on a sapphire substrate. The inset illustrates the *in-situ* indentation and the green arrow represents the direction of the incident X-ray beam. The facets are highlighted by black solid lines. **b.** Cut through a 3D coherent X-ray diffraction pattern and **c.** reconstructed electron density of the Au nanocrystal shown in panel (a). Taken from Refs.[2] 6

1.3 **a.** Reconstructed electron density drawn at 15% of the maximum value. The drop in the electron density indicates the position of the dislocation loop. Reconstructed u_{111} displacement field in **b.** the (110), **c.** the (112), and **d.** the (111) planes which intercept the loop in two locations. Taken from Refs.[2] 7

1.4 **a.** Displacement and **b.** full width of half maximum (FWHM) of the Au 111 Bragg peak in reciprocal space during the *in-situ* three-point bending test. **c.** Bending and **d.** torsion of the NW during the nano-mechanical test inferred from the displacement of the Au 111 Bragg peak is shown in part **a.** Taken from Refs[3] 7

2.1 Vapor-liquid-solid mechanism growth. The position of the catalyst particle is defining the position of the NW growth. **a.** shows the non selective area growth of the NW. Image **b.** illustrate different structural phases that may appear during the growth process: polytypism. 12

2.2 ZB unit cells in three dimension. The diagonal axis [111] is the growth axis. 13

2.3 WZ unit cells in three dimension. Here the growth axis is along [0001] 14

2.4 View along the $[10-1]$ direction on the ZB structure and the corresponding direction in a hexagonal WZ structure. 15

2.5 Stacking-sequence of the atomic close packed structure, corresponding to a view along the [111] direction as ABC and AB 15

3.1 Lattice in two dimensional space. d_{10} and d_{11} are representing the distance in between the planes (10) and (11) respectively. 22
3.2 Incident x-ray beam diffracted from a crystalline sample. **a.** shows the geometry for the Bragg condition. Condition for the constructive interference will be fulfilled only along the vector **q**. **b.** shows a lattice plane with Miller index, h, k, l in **Q** space. 25
3.3 **a.** Symmetric and **b.** asymmetric diffraction geometry. In symmetric diffraction geometry incident beam illuminate the lattice planes parallel to the surface of the crystal. While in asymmetric case, Bragg's law is fulfilled at lattice planes inclined by an angle with respect to the surface. 26
3.4 **a.** A rocking θ-scan around the 111 Bragg angle of GaAs. **b.** The lines in detector plane represent the reciprocal space at angles less, equal and larger than the Bragg angle. . . . 28
3.5 Two plane waves with slightly different wavelengths propagate in the same direction. Image obtained from Ref.[4] 29
3.6 Two plane waves with the same wavelength radiated by the source of the size w propagate at some offset angle. Image obtained from Ref.[4] 30

4.1 Schematic representation of ion beam column dual FIB-SEM inside of a vacuum system. In-set shows the apparatus setup for Ga-LIMS[5] 34
4.2 Schematic representation of dual beam system. FIB column has a 52^0 tilt with respect tot vertical SEM column at single "coincident" point on sample. Inset shows the real time monitoring of milling on sample by FIB cross-section with *in-situ* SEM imaging. . 35
4.3 Basic experimental layout of the FEI™ Helios NanoLab™ 600 dual FIB-SEM inside of a vacuum system. 35
4.4 **a.** SEM image of the Akiyama probe consisting of a quartz tuning fork and a Si cantilever tip. **b.** Magnified image of Si cantilever tip. Image is adopted from[6] 35
4.5 Basic layout of the Scanning Force Microscope for in situ Nanofocused X-ray diffraction (SFINX) **a.** two long-range piezo linear translation stages, **b.** xy-piezo scanner, **c.** sample stage ,**d.** z scanner, **e.** AFM cantilever and **f.** optical microscope 36
4.6 Experimental hutch room and scheme of the beamline in P23 beamline,PETRAIII (adapted from Refs.[7]). 37

5.1 Mode shapes of first three vibrational eigenmodes of the NW. 40
5.2 Experimental arrangement for electromechanical vibrations in as-grown NWs. An AC pulse was applied to NW. 45
5.3 **a.** NW before exciation (static state). **b.** Electromechanically induced first eigenmode of vibration in as-grown GaAs NW. 45
5.4 SEM image presenting the schematic view of the nanowires in two lines for easy accessibility and alignment. 46
5.5 Estimated error between excitation frequencies and their theoretical values plotted as function of Length. 47

6.1 **a.** GaAs NW under loading for 20min. The insets show the relaxation after unloading after (1) 5 sec, (2) 60 sec and (3) 9min. **b.** Curvature of the GaAs NW after release as a function of relaxation time measured by SEM 53

6.2 Deflection profile is extracted by scanning and recording the position of maximum intensity of each x-pixel along the y-axis. **a.** Line profile taken at $x = 100$. **b.** The corresponding intensity profile with maximum at $y = 93$. **c.** Misleading maximum intensity estimation influenced by the neighboring artifacts and particles for the deflection profile of the NW 54
6.3 **a.** The deflection profile of the NW is obtained by removing the outliers and fitted with a second order polynomial around the maximum. **b.** Stacked deflection profiles extracted from the SEM images by using the DIC algorithm. 54
6.4 Curvature of the NW **a.** per pixel **b.** per meter during the relaxation, after holding and release. 55
6.5 Residual of polynomial fit presented in Fig. 6.4 - **a.** 56
6.6 NW2 and NW3 before nanomanipulation i.e., pristine form. This geometry was taken as unstrained reference for the relaxation mechanism. 56
6.7 NW2 and NW3 bent and hold in semi-circle form for 17 minutes and 20 minutes respectively. NW3 has an offset angle between NW plane and image plane. 57
6.8 **a.** Offset angle and the diameter of semi circle arc, distance between point **A** and **B**, was estimated at 0° tilt of the sample stage. **b.** Bent NW imaged at 52° tilt. **c.** Skewed SEM image after the offset tilt correction fitted with a perfect circle. 58
6.9 Relaxation of the NW2 and NW3 as a function of time. Scale bar represents 1μm. Relaxation time for NW2 and NW3 is 13 minutes and 17 minutes respectively. 58
6.10 **a.** A straight NW with uniformly distributed point defects. **b.** In a Bent NW point defects migrates in stress gradient. Interstitial diffuse towards the tensile part and vacancies in opposite direction. c. Arrangement of vacancies in the hexagonal cross-section, during the bending. 59
6.11 Graphical illustration of a NW under the bending load. 60
6.12 Time dependent curvature profile of NW2. The holding time was 17 minutes with 2.87% initial bending strain. Black line indicates the elastic curvature κ_e while blue and black circles are total curvature κ and calculated curvature $\kappa_{experimental}$, respectively. Green and red lines are the contribution of point defects towards the total curvature. . 62
6.13 Time dependent anelastic strain as function of relaxation time compared with FEM result. Here FEM simulations are based on only one kind of point defects. 63
6.14 Strain profile originating from the migration of point defects a as function of time during the loading unloading of the NW2 64
6.15 **a.** Uniformly distributed vacancies across the cross-section. **b.-c.** During the loading process, vacancies are drifted towards the higher compression in the NW. **d.** The NW is released by removing the initial bending strain.**e.** Redistribution of vacancies to the original composition profile, after relaxation. **f.** Vertical line profiles measured at the center of the cross section as function of time. 65
6.16 **a.** Anelastic strain as a function of recovery time for different initial bending strain **b.** radius **c.** initial concentration **d.** holding time, **e.** partial molar volume and **f.** diffusion coefficients.The holding time was 900 s in every case study except **d** where the holding time was varied ($\pm 50\%$). 66
6.17 After releasing the initial bending strain, the time dependent curvature of the NW compared with FEM result. 67
6.18 Time dependent anelastic strain recovery of Be doped GaAs NWs. 68

6.19 **a.** Anelastic strain relaxation plotted on semi-log scale to extract an average time for the complete relaxation by the extrapolation of the curve. **b.** The average diffusion coefficients are compared with the FEM simulation. 68

7.1 **a.** Scanning electron micrograph of Be-doped GaAs NW laying across the Si micro trenches after dispersion of mixture by drop casting. Green arrow represents the direction of beam. The displacement of SFINX tip was along Q_x during the bending of the NW. **c.** Self suspended NWs are glued at their two supports by depositing platinum in the FIB/SEM system. **b.** Scanning Electron Microscopy image of the $2\bar{2}0$ side facets of GaAsNW sitting parallel to the surface of Silicon substrate. **d.** Illustrates the affixing of the $2\bar{2}0$ side facets to the surface of substrate schematically. 73
7.2 **a.** SEM image of a self suspended NWs1 laying across two micro trenches and glued by depositing in FIB/SEM system.SEM image captured after the nanomechanical testing at **b.** 0° and **c.** 52° tilt. **d.** During loading, the NW1 Fractured close to the Platinum clamping where the maximum stresses are present. 75
7.3 Three dimensional iso-surface of diffracted intensity in reciprocal space before lateral three point bending test. 75
7.4 RSMs of the $2\bar{2}0$ Bragg reflection of the NW1 recorded by rocking scan. 76
7.5 **1.-6.** 2θ vs torsion plot. NW was contacted by the SFINX tip at (3) where the Bragg peak splitting is observed. **7.-12.** corresponds to the integrated intensity plot of the torsion. 77
7.6 **a.** SEM image of self suspended NW2 before nanomechanical testing. **b.-c.** SEM image taken after nXRD and nanomechanical testing **b.** 0° and (c) 52° tilt. Analogous to NW1, round shaped blobs were observed for NW2 which was further investigated by Energy-dispersive X-ray spectroscopy (EDX). **d.** Elemental composition of round blobs determined by EDX. 78
7.7 $2\,\theta$ vs θ plot. Relative movement of the Bragg peak in θ with respect to zero corresponds to the rotation or the torsion of the NW. **a.-c.** Scans during the SFINX alignment in the vicinity of the NW **d.** NW comes in contact with the SFINX tip. **e.-i.** SFINX tip moved and bend the NW along Q_x at the speed of 2[nm/s]. **j.-l.** SFINX tip was retracted at the speed of 2[nm/s]. 78
7.8 Torsion induced in NW2 is plotted as function of time. The NW was bent during 645[s] to 990[s] with SFINX tip for total displacement of 10[nm] with the steps of 2[nm]. Red dotted line is the reference for zero torsion. 79
7.9 **A.** Two dimensional cuts from the three dimensional RSMs taken before (1) and after (2-4) the *in-situ* lateral three point bending test. **B.** 2D cuts from (**A.**) were integrated along Q_x and Q_y and fitted with Gaussian to extract the Bragg peak position. 79
7.10 **a.** SEM image of self suspended pristine NWs, NWs2, before *in-situ* three-point bending test. **b.** SEM image taken after nXRD and nanomechanical testing 0° tilt. Analogous to NW1 and NW2, round shaped blobs were observed for NW3 which was further investigated by Energy-dispersive X-ray spectroscopy (EDX). **c.** SEM image containing the section of NW and contamination for the site-specific EDX spectroscopy **d.** Elemental composition of round blobs determined by EDX in a overlaying map with subplot **c.** 81

7.11 2 θ vs θ plot. Relative movement of the Bragg peak in θ with respect to zero corresponds to the rotation or the torsion of the NW. **a.** Scans during the alignment SFINX and the NW alignment **b.** NW comes in contact with the SFINX tip when moving it along Q_x at the speed of 10[nm/s]. **c.** SFINX tip was interrupted and the NW kept under the stress from **e.** The SFINX tip was retracted and the NW was released. **f.-j.** The torsion in the NW relaxes as function of time. **k.-l.** Full retraction of the SFINX tip. 82
7.12 Torsion induced in NW3 is plotted as function of time. The NW was contacted at 745[s] and kept under the applied force until 1085[s] with SFINX tip for total displacement of 30 [nm]. Blue dotted line is the reference for zero torsion for the main peak, which shows the time dependent torsion relaxation. 83
7.13 **A.** Two dimensional cuts from the three dimensional RSMs taken before (1) and after (2-4) the *in-situ* lateral three point bending test. **B.** 2D cuts from **A.** were integrated along Q_x and Q_y and fitted with Gaussian to extract the Bragg peak position. Drifting of Bragg peak in Q_{xy} represents the time bending and torsion relaxation of the NW after the *in-situ* lateral three point bending test. 83

List of Tables

5.1 Structural parameters of as-grown GaAs NWs along with their corresponding eigenfrequencies and excitation time. 46

6.1 Summary of the samples used for anelastic relaxation experiment. 53
6.2 Summary of the parameters used in fitting model. 70

To my mother

Acknowledgments

Apparently, I am having a hard time writing this section in the manuscript. During my Ph.D., I have met and been inspired by many people, and it is not possible to thank each of them individually. Nevertheless, I'll start with my three supervisors: Ulli, Olivier, and Thomas.

Ulli, I am most grateful to you for presenting me with a wonderful opportunity to work on a joint Ph.D. project. Thank you very much for your invaluable remarks on my work, stimulating discussions, and sharing your extensive knowledge of nanowires and crystallography. Despite your busy schedule, you always find an answer to my problem and provide constant support throughout my Ph.D.

Olivier, I am constantly amazed by your tremendous understanding of mechanics and x-ray crystallography at the nanoscale. I owe you a great debt of gratitude for introducing me to the amazing field of nanomechanics. Thank you very much for your detailed comments on the manuscript and insightful discussion during Skype sessions or weekly meetings. They helped me to stay on track when I needed it the most. Also, Thank you very much for making me feel at home during my stay in Marseille.

Thomas, This joint Ph.D. project was not possible without your assistance. Thank you for taking care of everything, from administrative work to securing the funding. You are the one who explained to me the basics of SFINX. Having direct access to your room at Marseille was not less than an asset. Any question I have had regarding nanomechanics or x-ray diffraction techniques, I knew Thomas had a reference for it. Thanks for your constant and unconditional support during my stay in France. I am grateful to you and Olivier for traveling to Hamburg and Paris with SFINX during the peak of COVID-19.

I want to express my gratitude to **Prof. Christian Gutt** and **Dr. Anthony Ayari** for reviewing and examining the manuscript. I am also grateful to other defense committee members (**Prof. Dr. Thorsten Feldmann** and **Dr. Lisa Michez**) for joining the defense.

A big thanks to all my colleagues and fellow Ph.D. students at Siegen University and AMU. Specially; **Dr. Arman Davtyan** and **Dr. Danial Bahrami**, for supporting and offering help whenever needed.

Dr. Ali AlHassan, For joining my beamtime and providing the MATLAB codes. Thank you for sharing your expertise and knowledge throughout my Ph.D.

Mr. Mahmoud Alhumaidi, For sharing an office and rebooting the workstation every Monday morning.

Dr. Etienne Navarro, For insightful discussions and providing DIC algorithm.

I want to express my gratitude to my father, **Muhammad Siddique Khan Qamar**, for being there for me emotionally and for your eternal love. I still have a lot to learn from you about life and family. Moreover, a big thanks to my brothers **Zaheer** and **Ismail**. A heartful thanks to **Zaheer** and his wife **Guriya**, for their persistent motivation, support, and love. I enjoy every minute of **Arsal**'s videos. Thanks for taking care of everyone in my absence. **Sidra** and **Attiya**! I am just so blessed to have you this close in my life. A simple Thanks is not enough for your love.

Finally, I would like to express my deep gratitude to my wife **Attiqa** and my son **Abdullah** for their unconditional love and support during this journey.

Abdullah! Your morning smile is priceless. You are the pride and joy of my life.

Attiqa! You have been extremely supportive of me throughout this process and have made countless sacrifices while encouraging me to get to this point. Thank you for your unconditional and selfless support. You both are nearest to my heart, and I can't express how much I appreciate having both of you. Thank you!

1 Introduction

1.1 Mechanical properties at nanoscale

Nanomechanics or mechanics on nanometer scale is a relatively new research area that concerns the mechanical properties and behavior of nanomaterials. The criterion for a material to be considered "nano" is having a characteristic dimension smaller than 100[nm]. This reduction in the characteristic dimensions at nanoscale regime causes dramatic changes in the mechanical properties of the nano-object. Along with miniaturization and scalable integration of the desired functional properties there is a constant need to investigate and characterize the mechanical behavior and deformation mechanisms of low-dimensional materials.

At nanoscale, the limited size induces a unique behavior. Reports have shown that micro- and nanostructures exhibit increased elastic limit as compared with their bulk counterpart[8,9]. Hence nanoobjects can sustain elastic strains of few percent whereas larger size materials relax the stored elastic energy via brittle failure or plasticity. This opens the door to strain engineering where elastic deformation is used to modify physical properties. Even a minute strain to a semiconductor or other crystalline material can distort the atomic position sufficiently to introduce significant changes in its properties, such as the electrical and thermal transport properties. One percent elastic strain, which is a huge elastic strain, can in some cases improve the speed of the device by 50%[10], by allowing electrons to move through the material faster. Diamond, the strongest and hardest material found in nature, can be elastically stretched by as much as 9 percent without failure[11] when it is in the form of nanometer-sized needles while wires of

silicon can be stretched purely elastically by more than 16% [12].

There are other methods that can be used to tailor the properties of a nanomaterial such as chemical doping, which produce a permanent, static change. On the contrary, elastic strain engineering allows to modify the properties and behavior in a controlled fashion. In an effort to fabricate materials tuned precisely for electronic, optoelectronic, and photonic devices that could find uses for communications, information processing, and energy applications, the understanding of the mechanical behavior at the nanoscale is of paramount interest. The cross-disciplinary nature of nanomechanics has provided extraordinary and revolutionary advances in science and engineering and it is widely agreed to be an essential core component for the development of novel materials and technologies in the foreseeable future.

To study the mechanical properties of nanostructures, the present thesis concentrates on fundamental mechanics of nanostructures under different external mechanical influences.

To introduce this thesis, in the first section, some general information and state-of-the-art of *in-situ* nanomechanical tests combined with X-ray diffraction techniques is provided. Finally, the aim of this project is briefly described and the structure of the thesis is introduced.

1.2 State of the art nanomechanics

A range of new techniques and methods have been deployed to investigate the peculiar mechanical nature of nanomaterials. The elastic and plastic deformation, fatigue, fracture and creep behavior of nanomaterials have been studied by various direct (uniaxial tensile and compression tests [13,14,15,16], nanoindentation [17,18] and bending test) and indirect (vibration test [19]) characterization methods. These nanomanipulation techniques have relied heavily on different microscopy techniques like Atomic Force Microscopy (AFM), Focused Ion Beam/Scanning Electron Microscopy(FIB/SEM) and Transmission Electron Microscopy (TEM). More specifically integration of FIB with SEM has allowed to design on site sub-micron pillars out of bulk materials for mechanical testing [8]. Compression and tensile tests on such micropillars demonstrated finite size effects [13,14]. Scanning Electron Microscopy allows the direct visualization and tracking of the deformation of the structure. Due to its surface sensitivity SEM does not give any information regarding dislocations and defects inside the nanostructure during the testing and only provide access to the defects which exist at the surface [20,13]. On the other hand, TEM allows monitoring of nucleation and propagation of dislocations during the testing but calls for additional sample preparation in order to provide electron-transparent foils [21,22,23].

In this thesis, we investigated the mechanical properties of single semiconductor *GaAs* Nanowires NWs using synchrotron based diffraction techniques in their as-grown geometry as well as in three point bending configuration. Thus discussion in the following is limited to the *in-situ* micro- and nano-mechanical testing in combination with synchrotron X-ray diffraction techniques.

1.2.1 *In-situ* micro- and nano-mechanical tests in combination with synchrotron X-ray diffraction techniques

Due to the non-invasive nature of X-ray diffraction and high sensitivity towards the elastic strain and defects, *in-situ* mechanical tests combined with synchrotron X-ray diffraction techniques may yield detailed strain and defects information in the volume of the tested nanomaterial. With the remarkable progress of the X-ray sources (e.g. 3rd generation synchrotron) and the focusing optics several mechanical testing instruments have been developed for *in-situ* indentation and uniaxial testing. At the Paul-Scherrer Institute (PSI) in Switzerland an indenter for *in-situ* micro-compression tests on metal micropillars in combination with Laue microdiffraction was developed[15,16]. Another similar instrument for *in-situ* compression and bending tests also in combination with Laue microdiffraction was developed at the Montan university in Leoben (Austria) and employed at the BM32 beamline at the European Synchrotron in Grenoble[24]. Recently, at beamline P03 beamline at the PETRA III an *in-situ* indenter was designed and coupled with X-ray diffraction in transmission geometry using hard X-ray beams that are focused down to a size of the order of 200[nm][25,26]. Although these instruments are aligned to the submicron sample by optical microscopy, additional care is needed to attain a precise alignment which further complicates the study. To overcome this issue, Ren et al.[27] developed a scanning force microscope for *in-situ* nanofocused X-ray diffraction studies (Scanning Force Microscope for in situ Nanofocused X-ray diffraction (SFINX)) which was combined with Bragg coherent X-ray diffraction imaging and Laue microdiffaction for *in-situ* nano-indentation on crystals and for *in-situ* three-point bending tests on NWs, respectively[28,27]. The imaging capabilities of SFINX facilitate the alignment of the SFINX-tip on a selected nanostructure and the incident X-ray beam.

In this thesis, we have used SFINX combined with Nano X-rays Diffraction (nXRD). The basic principles of Nano X-rays Diffraction (nXRD) and SFINX are provided in the Chapter 3 and Chapter 4 respectively. Here, the *in-situ* mechanical tests employing the Nano X-rays Diffraction (nXRD) and Bragg Coherent X-rays Diffraction Imaging (BCDI) are briefly reviewed.

1.2.2 *In-situ* micro-mechanical testing and Nano X-rays Diffraction

In-situ nXRD was demonstrated by Stefenelli et al.[29] on a lamella of an indented CrN-Cr multilayer thin film in a transmission geometry providing access to the local stress fields around the indenter imprint. Later on it was incorporated with the *in-situ* indenter at the P03 beamline at PETRA III to investigate the strain field and the microstructural variations in Zr-based bulk metallic glasses[25] and in several micrometer thick TiN films[26]. The authors were able to quantify the strain and strain gradients from the peak positions and widths by following the tilting of TiN crystallites, which was related to a crack propagation in the film.

An analogous setup, the X-AFM was developed at the European Synchrotron ESRF in Grenoble (France) with the possibility of recording the deformation mechanism of the microstructure that was not feasible

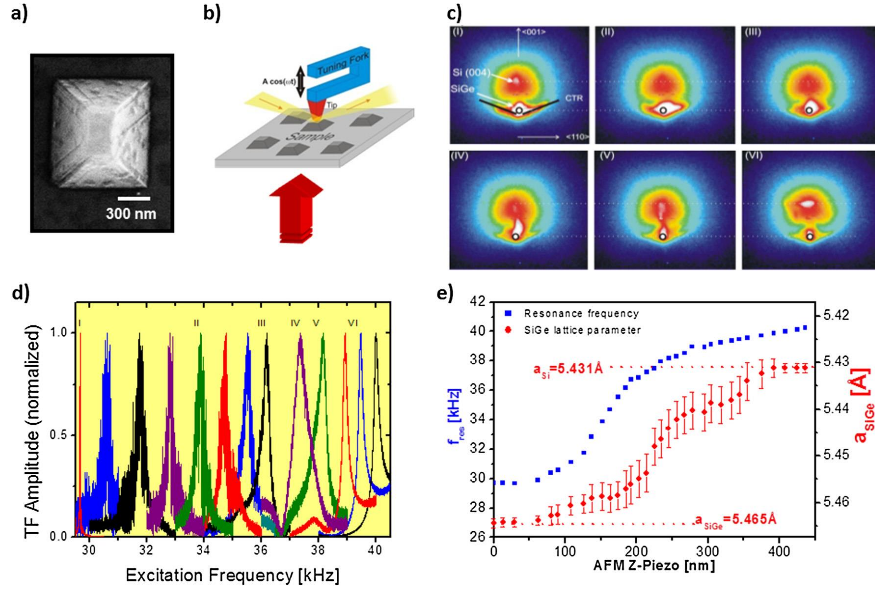

Figure 1.1: a. Scanning electron micrograph of a SiGe island. **b.** Schematic illustration of the mechanical loading of a SiGe island using the AFM-tip and simultaneous X-ray diffraction. **c.** X-ray diffraction patterns for 6 consecutive pressures applied on an individual SiGe island. The Si (004) and SiGe Bragg reflections are marked by arrows while the CTRs originating from the island side facets are highlighted by black lines, and the substrate CTR is encircled. **d.** Normalized resonance frequencies of the AFM tuning fork. The resonance curves corresponding to the diffraction maps from panel **c.** are indicated by Roman numerals I to VI. **e.** Variation of the SiGe island lattice parameter (red) and the tuning fork resonance frequency as a function of the sample displacement Δz. Taken from Refs. [1]

at P03 [1,30]. Employing X-AFM furnished the *in-situ* compression of a single microstructure and monitoring the deformation by monochromatic X-ray diffraction on a single SiGe island. The authors were able to record a 2D X-ray diffraction pattern around Si (004) Bragg peak. The evolution of the Bragg peak was followed with the increasing mechanical load applied on the SiGe island Fig. 1.1 - (c) while simultaneously recording the resonance frequency of the tuning fork. Initially, as mechanical load increases the Crystal Truncation Rods (CTRs) of the SiGe island side facets collapse (II and III) and the Bragg signal of the SiGe island shifts to larger Qz values (IV and V) until it is superimposed with the Bragg reflection of the Si substrate (VI).Simultaneously the resonance frequency of the tuning fork was increased from 29[kHz] for the free tuning fork to 40[kHz] see Fig. 1.1 - (d). The results show a direct correlation between the tuning fork resonance frequency and the lattice parameter Fig. 1.1 - (e) of the SiGe island and revealed a Young's modulus of (108 ± 12)[GPa], which is very close to the literature value for a SiGe island of 105[GPa].

Thanks to the recent developments in focusing optics, 50[nm] hard X-ray beams are readily available at numerous beamlines. Combined with *in-situ* nanoindentation and tensile testing techniques allow for an in-depth assessment of local strain and defects. While the above mentioned experiments concentrated on 2D X-ray diffraction patterns providing limited access to the deformation of a structure, the three-dimensional intensity distribution in the vicinity of a given Bragg reflection is necessary to obtain more information on the deformation and defects. Such 3D reciprocal space maps are typically recorded by

rocking curves which may induce vibrations that are detrimental to the nano-mechanical setup. Thus, a new method was developed where the energy of the incident X-ray beam is scanned thus avoiding the movement of any diffractometer motor [3].

1.2.3 *In-situ* mechanical tests with coherent Bragg diffraction imaging

A fully coherent X-ray beam provides the three dimensional reciprocal space maps by recording the 3D intensity distribution with the help of two dimensional CCD matrix detector. Although reciprocal space mapping is independent of beam coherence a coherent beam provides the apparition of detailed size and strain interference features in the X-rays Diffraction (XRD) patterns. These features are lost when the beam is incoherent. During coherent diffraction, the Bragg's condition is satisfied by coherently illuminating the specimen by x-ray beam. While Bragg Coherent X-rays Diffraction Imaging (BCDI) is only possible when the diffraction pattern obtained from coherent x-ray beam are inverted by Fast Fourier Transformation (FFT) into a real space image. A fully coherent X-ray beam provides a spatial resolution of (5-10[nm]) and resolution in displacement of 1[pm]. The measured far field intensity distribution is proportional to the square of Fourier transform of the complex electron density distribution of the crystal in real space. The loss of phase information through absolute square value is known in X-ray crystallography as the phase problem. It can be resolved by employing phase retrieval algorithms that provide access to the local displacement projected along the diffraction vector. Phase retrieval is more general tool and applies also to non-crystallized matter when used in forward geometry. In Bragg geometry the displacement field is retrieved and used to estimate the strain and defects distribution within the crystal. As compared to other diffraction techniques, BCDI is a relatively new diffraction technique and it gives access to the structural variations during the nanomechanical testing. For various as-grown nanostructures BCDI has shown sensitivity towards small strain variations in the order of 10^4 [31,32]. Mechanical test relying on thermal treatment i.e., mechanical loading via thermal cycling combined with BCDI have also been reported in the past [33,34]. Recently, after the development of Scanning Force Microscope for in situ Nanofocused X-ray diffraction (SFINX), various *in-situ* nano-mechanical tests combined with BCDI have been reported [3,2].

Dupraz et al. [2,35] demonstrated the potential of BCDI by imaging a prismatic dislocation loop that was induced by nano-indentation using SFINX and trapped inside the nanocrystal. A scanning electron micrograph of a typical Au crystal is shown in Fig. 1.2 - (a). Reconstructed electron density of the Au nanocrystal presented in Fig. 1.2 - (c) demonstrating a perfect agreement between the SEM image and the reconstructed shape of the pristine crystal. The crystal exhibits a Winterbottom equilibrium shape where all the [100] and [111] facets connected with rounded edges are clearly identified from the reconstructed electron density. The reconstructed electron density after the indentation of the Au crystal reveals a loop-shaped feature, nearly 100[nm] above the particle-substrate interface and with a diameter of 30[nm] at

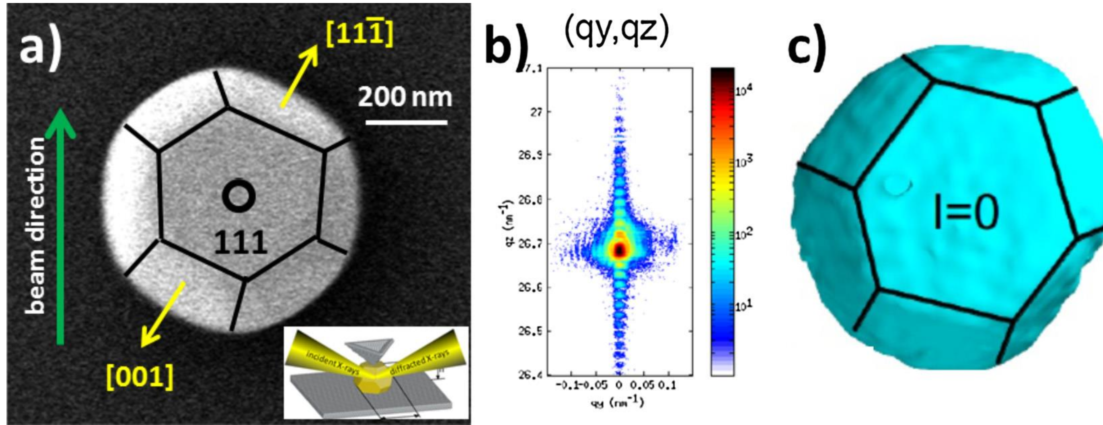

Figure 1.2: a. SEM image of Au nano-crystal prepared by dewetting of a 45[nm] Au thin film on a sapphire substrate. The inset illustrates the *in-situ* indentation and the green arrow represents the direction of the incident X-ray beam. The facets are highlighted by black solid lines. **b.** Cut through a 3D coherent X-ray diffraction pattern and **c.** reconstructed electron density of the Au nanocrystal shown in panel (a). Taken from Refs.[2]

the center of the Au particle. It exhibits a characteristic intensity drops which is expected in the vicinity of dislocations. This drom is still open for debate as one group tend to believe that it is a numerical artefact related to Fourier transformation while another group think it is related to the incomplete collection of photons by the detector because of tilted lattice planes in the vicinity of the defect. The (110), the (112), and the (111) planes displayed in Fig. 1.2 - (b–d) intercept the loop in two locations where a pair of phase vortices with opposite directions is observed. The profile of the u_{111} displacement field around the defect is very similar to the u_{111} displacement field around a simulated prismatic dislocation loops[36]. Between the two phase vortices, the rapid phase variations along the loop axis are localized to a region which does not exceed the loop diameter. In the plane that intercepts the loop perpendicularly to its axis, the phase shift between the regions inside and outside the loop is roughly equal to π coinciding with simulations.

Recently, Davydok et al.[3] investigated the deformation of a gold NW loaded *in-situ* in a three-point bending configuration using SFINX in combination with BCDI using sub-micrometer focused hard X-ray beams. The diffraction patterns before and after the deformation provided detailed structural information on a single Au NW. Deformation at different loading stages was monitored and measured by scanning the energy of the incident X-ray beam. Higher resolution 3D reciprocal space maps revealed plastic deformation in NW with a bending of 0.7° as depicted in Fig 1.4. Besides bending also torsion was evidenced as soon as SFINX -tip contacts NW and torsion remains rather constant during the loading process. Furthermore, the torsion is about one order of magnitude smaller than the bending at the highest load. After unloading the NW stays twisted by about 0.05° . The residual bending and the torsion are evidences that NW was plastically deformed.

Despite all advances in imaging and *in-situ* experimentation techniques, it remains difficult to phase retrieve highly defective or highly strained crystals[37,38]. This is a consequence of the very high sensitivity of BCD to any deviation from the perfect crystalline order. As a result, BCD or BCDI remain limited to

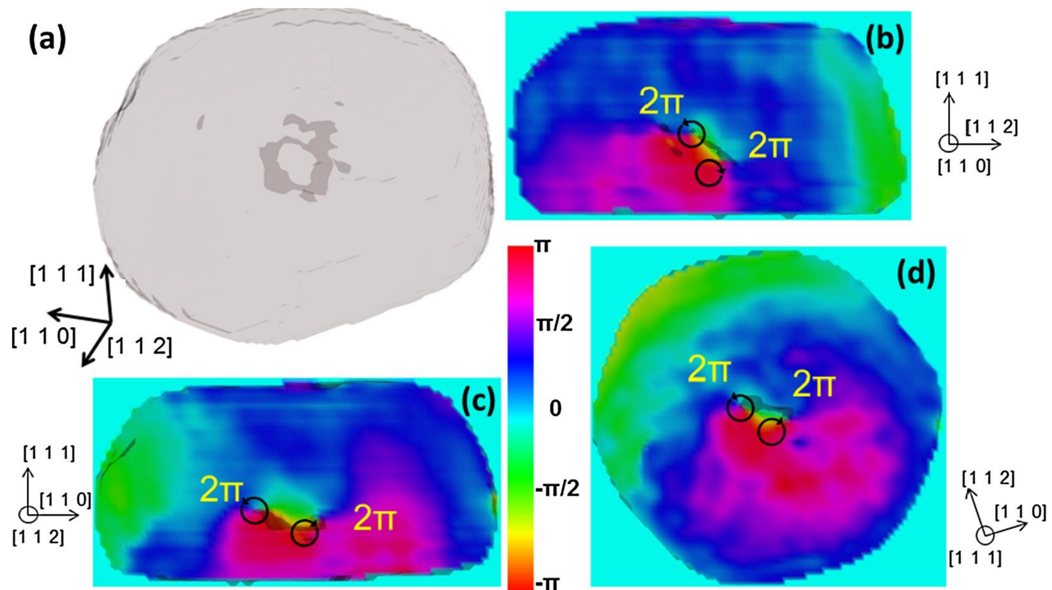

Figure 1.3: a. Reconstructed electron density drawn at 15% of the maximum value. The drop in the electron density indicates the position of the dislocation loop. Reconstructed u_{111} displacement field in **b.** the (110), **c.** the (112), and **d.** the (111) planes which intercept the loop in two locations. Taken from Refs.[2]

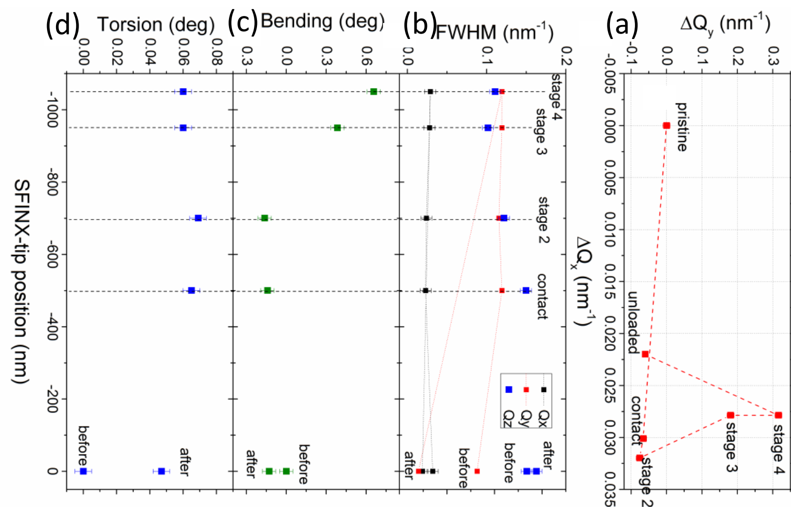

Figure 1.4: a. Displacement and **b.** full width of half maximum (FWHM) of the Au 111 Bragg peak in reciprocal space during the *in-situ* three-point bending test. **c.** Bending and **d.** torsion of the NW during the nano-mechanical test inferred from the displacement of the Au 111 Bragg peak is shown in part **a.** Taken from Refs[3]

very small deformation or amount of defects. This is why *in-situ* mechanical tests with coherent diffraction remain limited.

1.3 Thesis Structure

In this manuscript, we investigate the mechanical properties of single semiconductor GaAs NWs using synchrotron based focused X-rays Diffraction (XRD) in the as-grown geometry and as well as during three-point bending test. At the same time, obstacles, technical limitations, and general background to understand the original research results will be discussed in detail. The manuscript is organized in seven chapters and the outline is as following:

Chapter 2 - Semiconductor nanowires
In the second chapter, the basic concepts concerning crystal phase structure and general aspects of the epitaxial growth of free-standing semiconductor NWs are discussed briefly.

Chapter 3 - Kinematic x-ray diffraction
In this chapter, the key principles of X-ray diffraction and coherent X-ray diffraction are presented. The description includes the scanning modes used experimentally, i.e., Scanning x-ray diffraction microscopy (SXDM) for nXRD and BCDI at the synchrotron beamlines.

Chapter 4 - Experimental methods
This chapter aims at introducing the design and working principles of the main experimental techniques used in this work for the preparation and characterization of semiconductor NWs. Later on, we introduce the operational setup and functionality of custom built Scanning Force Microscope for in situ Nanofocused X-ray diffraction (SFINX).

Chapter 5 - Electromechanical resonance in nanowires
This chapter is related to the impact of systematic dynamic mechanical loading on the different structural phases of the NW by using the resonance test. The descriptions include some theoretical background followed by various factors impacting the quality factor of the resonating NWs followed by the *in-situ* electromechanical vibrational loading of NWs in FIB/SEM.

Chapter 6 - Anelasticity in semiconductor nanowires
This chapter presents the original experiments evidencing anelastic relaxation in initially bent Be-doped GaAs NWs. A model based on diffusion in a stress field (Gorsky effect) is developed to interpret the experimental data.

Chapter 7 - Three point bending test on Be doped GaAs nanowires
This chapter relates to the *in-situ* X-rays Diffraction study of the mechanical properties of Be-doped

GaAs NWs in three-point bending test by using Scanning Force Microscope for in situ Nanofocused X-ray diffraction (SFINX). The elastic, plastic and anelastic deformation in the Be-doped GaAs NWs were visualized and discussed.

Chapter 8 - Conclusion

In the last chapter, we discuss and summarize the main results obtained in this thesis.

2
Semiconductor Nanowires

Semiconductor Nanowires (NWs) are regarded as potential candidates for future optoelectronics and sensor-based Nano-electromechincal systems (NEMS)[39,40,41,42] systems. Indeed, they were shown to exhibit superior properties compared to their bulk counterparts thanks to finite-size and quantum size effects caused by their large aspect ratio and quasi-one-dimensional nature. In the recent years III-V semiconductor NWs gained momentum as their fabrication can be done directly on silicon substrates. Silicon is the most used semiconductor in the microelectronics industry. GaAs, however, has higher electron mobility and exhibits a direct band gap but due to its higher cost, it is used for very specific applications only where its unique capabilities justify a higher cost[43].

In this chapter, we describe the basic principles of the epitaxial growth of free-standing semiconductor GaAs, NWs. At first, epitaxial growth by using Molecular Beam Epitaxy (MBE) will be covered, then the crystal structures of GaAs and two crystalline structures, zinc-blende crystal structure (ZB) and wurtzite crystal structure (WZ) are summarized. At the end of the chapter, p-type Be-doped GaAs nanowires are discussed in detail.

2.1 Epitaxy and crystal growth techniques

Growth on a template in a controlled, ordered, and systematic fashion is called "epitaxy", from the Greek words "epi" ("above") and "taxis" ("in an ordered manner"). Epitaxial growth is a bottom-up method where the layers of crystals are grown atom by atom on a substrate. The fabrication process is controlled

by manipulating the gas flux, droplet size, and the temperature for the various mechanisms involved. For the growth of the NWs several techniques can be employed but metal-organic vapor phase epitaxy (MOVPE) or MBE via so-called vapor-liquid-solid mechanism (VLS) are the most common growth methods for homoeptitaxial III-V semiconductors. Before going into the details of the crystal structure of GaAs and its different phases, a brief introduction of MBE is presented in the following subsection.

2.1.1 Molecular Beam Epitaxy

Molecular Beam Epitaxy is one of the most widely used growth methods for the fabrication of III-V semiconductor NWs based on the vapour-liquid-solid (VLS) process, which is actually a catalytic assisted growth process. In many cases, Au particles are used as catalytic seeds. Gold, however, may interdiffuse into the material and affects the electronic properties of the nanostructures. Thus, self-catalytic growth is preferred[44]. In this method, crystalline thin films are grown on a heated substrate by the interaction of one to several molecular or atomic beams under ultra high vacuum (UHV) conditions with the substrate[45,46]. With multiple interdependent steps, the crystal growth is a complex process with gas phase reactions and unstable precursors being involved. Nevertheless, it offers much needed growth characteristics such as smoother surface growth with the precise and *in-situ* control of crystal growth on the atomic level with a growth rate of 1 monolayer (lattice plane) per second and low growth temperature. Throughout this work, we focus solely on GaAs NWs grown on silicon substrates using MBE and provided by the Paul-Drude institute in Berlin. For free-standing GaAs NWs, this can be done in two different ways:

1. by the use of a seed particle made of a foreign material, typically Gold (Au)[47]

2. by introducing a droplet of one of the constituent element, called self-seeded[48]

The conventional growth mechanism is the same in these methods and both are presented in the next subsections.

2.1.2 Gold-assisted nanowire growth

As the name suggests, the GaAs NWs are grown by using Au seed particles as catalyst. Use of a metallic seed particle was the first realization of growing NW on a semiconductor substrate under the vapor-liquid-solid mechanism[44] where a crystal is formed through adsorption of atoms from the gas phase on to liquid and then to a solid layer. Starting with gold, the liquid particles as seeds with a diameter usually of tens of nanometers, are deposited on the substrate surface[49,50]. A typical method to achieve this is by direct deposition of a thin Au layer assisted by annealing above the melting temperature of the Au film. This results in to a subsequent dewetting of the Au film and the formation of droplets. Alternatively, Au colloidal nanoparticles can be deposited directly to silicon, providing extra control over the size of the gold particles[51]. Once the substrate temperature is raised to the growth temperature (∼600[°C]),

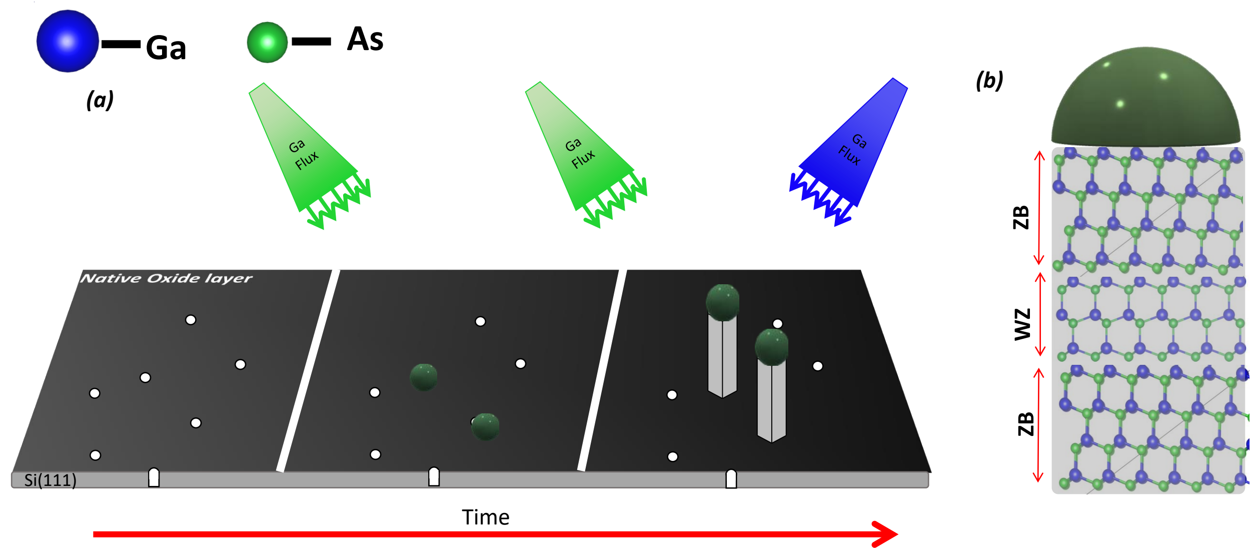

Figure 2.1: Vapor-liquid-solid mechanism growth. The position of the catalyst particle is defining the position of the NW growth. **a.** shows the non selective area growth of the NW. Image **b.** illustrate different structural phases that may appear during the growth process: polytypism.

Ga and As fluxes are supplied in the vapor phase. The crystal growth relies on a phase transition from the vapor phase to the solid phase. The melting point of Au is decreased as soon Ga incorporates with it and results in a Au-Ga alloy [52]. Solubility of As is very low. The vapor Ga and As atoms are solved in the liquid Au droplet until the concentration in the droplet exceeds a critical value (supersaturation). The chemical potential difference between the solved atoms in the droplet and the substrate surface below the droplet leads to the formation of a solid monolayer at the droplet to substrate interface which causes lifting the droplet upwards by the resulting GaAs NW. In order to grow a crystal in the shape of NWs it is necessary to promote the growth along one crystallographic direction. It can be achieved by optimizing the growth conditions and by using a mask with only small openings in it , onto the substrate. This method is also known as selective area growth (SA).

2.1.3 Gallium-assisted nanowire growth

In this process, Gallium droplet is used as a substitute for Au catalyst in order to have Au free growth of GaAs NWs. For the first time it was realized by Fontcuberta et al. [53,54] on GaAs substrate which was covered by an oxide layer. In this thesis, we investigated GaAs NWs that were grown on silicon substrate. The substrate was covered with the oxide layer of native SiO_2. During the first step, Ga particles in the vapor phase form liquid droplets after absorption at the surface of the native oxide SiO_2. Ga droplets stick to the defects on the native oxide layer and start to etch the native oxide. In this way, it makes a direct contact to Si substrate. Next, As shutter opens at the growth temperature. As atoms are dissolved in the Ga droplet, thus forming crystallization, supersaturation, and subsequent epitaxial GaAs growth at the

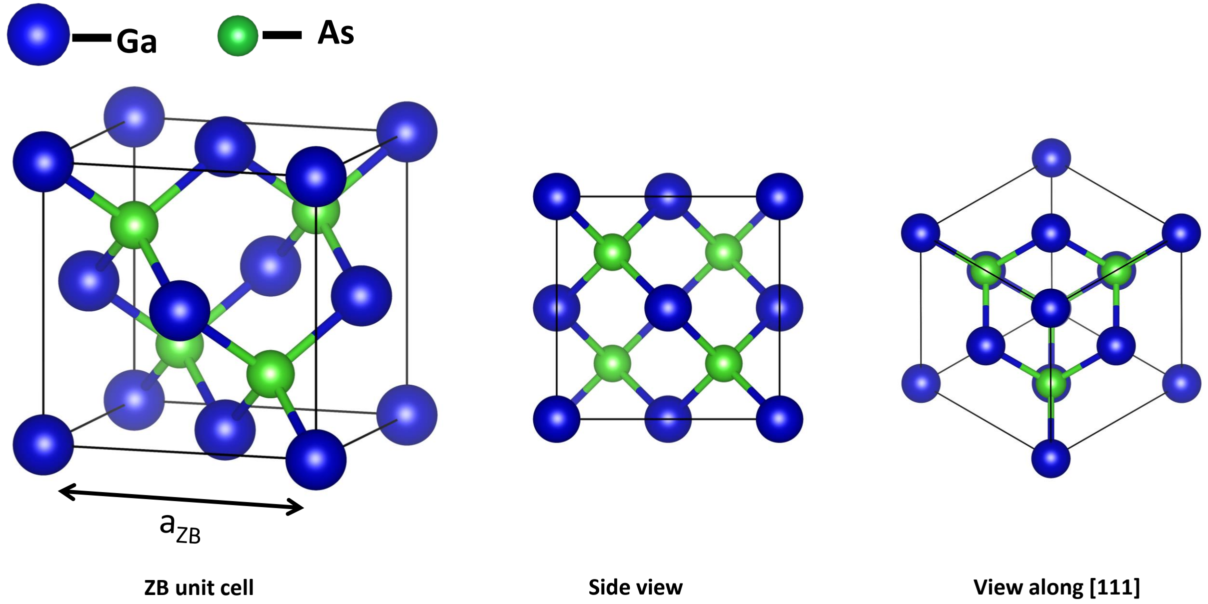

Figure 2.2: ZB unit cells in three dimension. The diagonal axis [111] is the growth axis.

bottom of the droplet due to chemical potential differences. The possibility of the fusion of impurity atoms into the NWs grown by self-assisted process is negligible, as no other atoms are present during growth. In addition, such NWs are found to grow in the cubic ZB structure , however the WZ structure and mixtures of both are observed as well[55,56,57,58]. The complete process of Ga-assisted growth of GaAs NWs is depicted in Fig. 2.1

2.1.4 Crystal structure of GaAs nanowires

At ambient conditions, the cubic ZB structure is the stable crystalline phase of bulk GaAs crystals. For GaAs NWs grown by MBE, the two most common crystal structures are the cubic ZB and hexagonal WZ. The possibility of the pure ZB and/or WZ phase and the coexistence of different crystal phases, known as polytypism, in the same NW is very common. More complicated crystal structures, such as the 4H phase, is also possible to grow.
In MBE ,GaAs NWs are grown in [111] direction along the same principle direction as the silicon substrate. In ZB structure the conventional unit cell consist of a cube with Ga atoms in the corners and at the center of each face. The corresponding lattice is Face-Centred Cubic (FCC).Both the Ga and As atoms are arranged in FCC structure and translated $\frac{1}{4}$ of a unit cell with respect to each other. There are four atoms of As inside the unit cell positioned in such a way that each As atoms binds to four Ga atoms in a symmetric tetrahedral coordination as shown in Fig. 2.2. Crystal lattice is assembled by the continuous repetition of the unit cell. The cubic lattice parameters are $a_{cubic} = b_{cubic} = c_{cubic}$ =5.65[Å], with $\alpha = \beta = \gamma = 90°$.

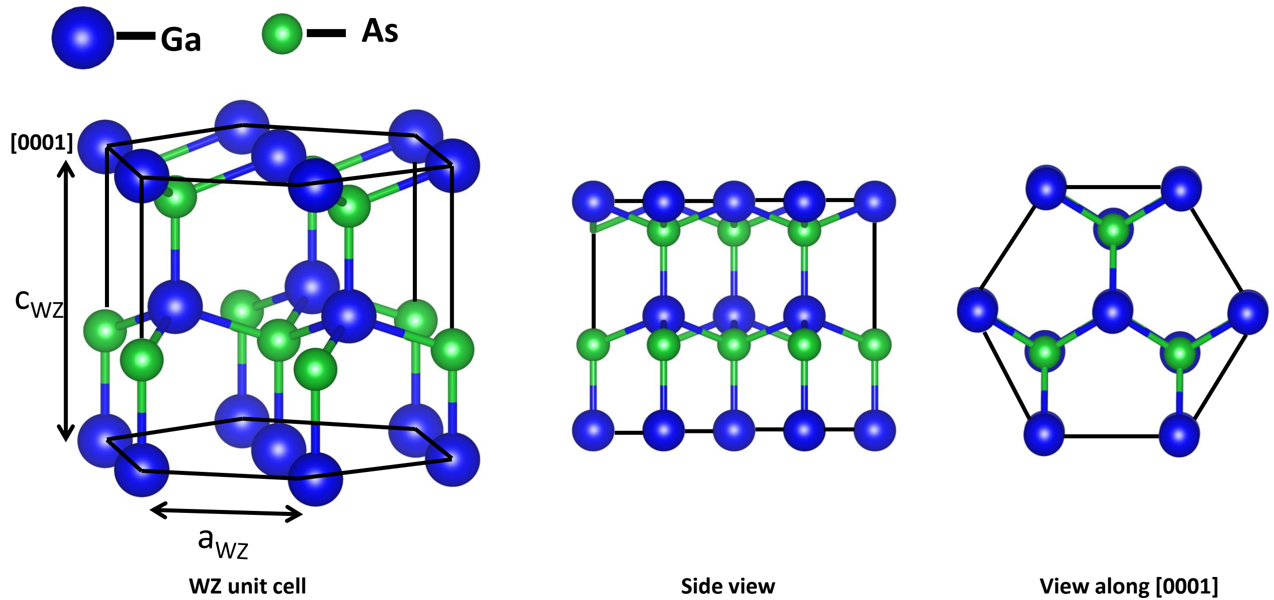

Figure 2.3: WZ unit cells in three dimension. Here the growth axis is along $[0001]$

Similar to ZB, WZ, Ga atoms are positioned in the corner of the unit cell while making a tetrahedral coordination with the four As atoms. Here the unit cell is hexagonal with a rhombus as a base, which means having an angle of 60 ° and 120° at the corners. Two lattice constants are needed to determine the size of the WZ unit cell with one lattice constant a. Two lattice constants can be used to describe a hexagonal structure $a_{wz} = 3.99[\text{Å}]$ describing the size of the base of the rhombus and $c_{wz} = 9.79[\text{Å}]$ is used to define the height of the unit cell. In Fig. 2.3 different viewing angles are presented graphically for WZ unit cell.

Both ZB and WZ are close-packed structures with the difference in the stacking sequence of the next nearest atom within the Ga or As sublattice placed at side by side lattice positions along the growth axis. Growth axis is along the diagonal in ZB and along the c axis in WZ. The stacking patterns are shown in Fig. 2.4. Every third bi-layer is repeated in ZB $\ldots ABCABCABC \ldots$ while for WZ every second bi-layer is repeated $\ldots ABABAB \ldots$ where the A, B and C planes (Fig. 2.5) are constituted by bi-layers of Ga and As atoms.
To further understand the stacking of atoms in GaAs, consider the stacked atoms in Fig. 2.5. To stack them as close as possible in a single layer, they should be arranged in a hexagonal pattern. While adding another hexagonal layer of atoms on top of the first, it will be placed between the voids of the first layer. The third layer of the atoms may either be placed directly above the atoms or above the voids between the first layer. If the third layer is placed exactly above the atoms of the first layer, the $\ldots ABABAB \ldots$ stacking sequence of the ZB structure. If the third layer is above the voids, the $\ldots ABCABCABC \ldots$ of ZB is achieved.

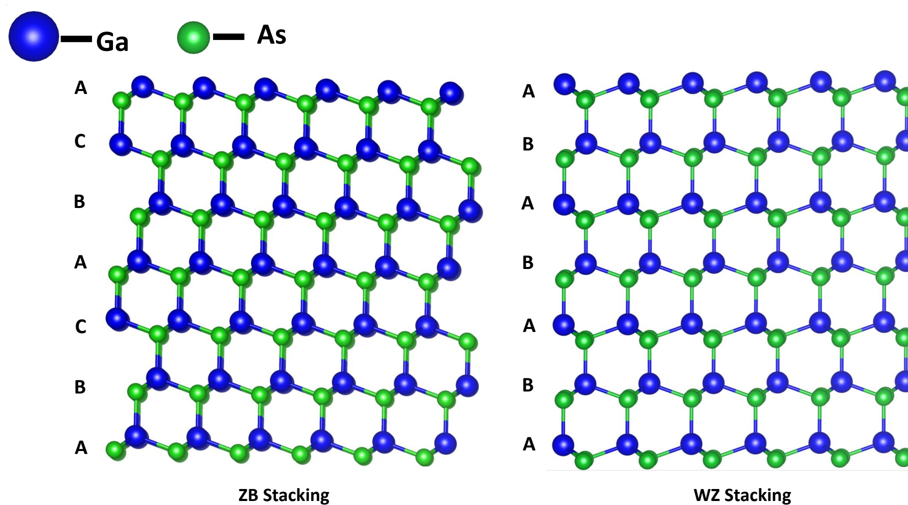

Figure 2.4: View along the $[10-1]$ direction on the ZB structure and the corresponding direction in a hexagonal WZ structure.

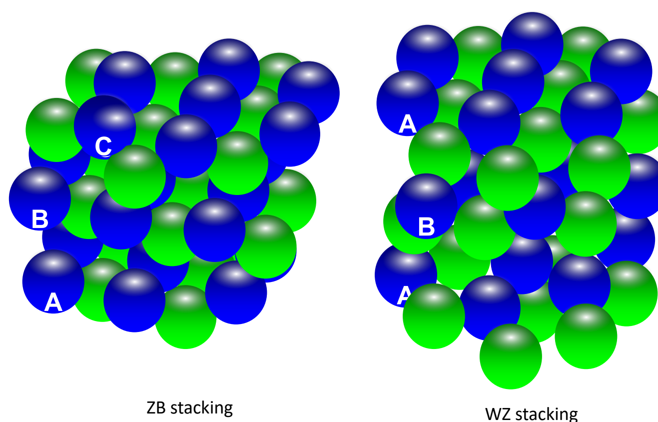

Figure 2.5: Stacking-sequence of the atomic close packed structure, corresponding to a view along the $[111]$ direction as ABC and AB

Stacking faults (SF) and rotational twins may form during the growth. A rotational twin corresponds to a 180° rotation of the ZB structure around the growth axis, is an inverted ZB sequence at a twin boundary along the growth direction, known as twinned zinc-blende (TZB). This stacking fault in the epitaxial layer sequence or the twin-boundary initiates a $\ldots ABABAB \ldots$ hexagonal close packed atomic sub-layers stacked sequence along the [111]-direction. These sub-layers are perpendicular to the [111]-direction and contain either only Ga or only As atoms and hence with repeated twin boundaries constitute a WZ segment of the GaAs Nanowire.
Cubic zinc-blende crystal structure (ZB) is mostly found in stable bulk III/V materials and in case of GaAs it is energetically favorable due to the difference in the cohesive binding energies between wurtzite and zinc-blende which is $\partial E = E_{wz} - E_{zb} = 24$ [meV/pair][59]. However, many studies have reported wurtzite phase for [111] oriented nanowires with hexagonal cross-section[60,61]. The presence of WZ phase is attributed to the lower surface energies of the side wall facets caused by the lower number of dangling bonds of WZ NW. Akiyama et al.[62] predicted a critical radius ranging from 1-22[nm] for which WZ phase is energetically favored and an intermediate regime ranging from 12-32[nm] for the coexistence of both polytypisms in the same structure.

Consequently, solely thermodynamic considerations might be insufficient for a description of the wurtzite-zincblende polytypism. Therefore, we now consider polytypism by kinetic aspects of nanowire growth.

In the case of Au-assisted GaAs nanowires, wurtzite segments are frequently observed at the very bottom of the NW closer to the substrate and at the top just below the droplet[63]. As a result, these segments were formed at the beginning and at the end of development. As reported for self-assisted GaAs nanowires by Rieger et al.[64], wurtzite developed in a controlled manner during the consumption of liquid Ga-droplet. Various growth parameters, such as the temperature of the substrate, flux ratio, supersaturation, and the shape of the catalyst are important parameters for describing and understanding polytypism. Subsequently, a kinetic approach to polytypism involves important parameters such as supersaturation[65], the shape of the droplet[66] and the geometry of the nucleation site[67] (and thus the surface energy of the involved facets[68]) which determine the energy barrier E for the creation of the critical nucleus. The nucleation energy barrier is related to the layer-nucleation rate J by[69].

$$J = J_0 exp^{-\frac{E}{k_b T}} \tag{2.1}$$

The number of layers per time[70,71] is controlled by the substrate temperature T and the absolute value of the energy .In the case of wurtzite zinc-blende polytypism, a minimum of four nucleation barriers should be considered :

1. $E_{WZ|ZB}$ and $E_{ZB|WZ}$ Energy required to grow a wurtzite layer on top of a zinc-blende layer or vice versa

2. $E_{WZ|WZ}$ and $E_{ZB|ZB}$ Without interruption of the stacking sequence add a new layer of the current polytype

The differences between these energy barriers make it possible to approximate and control the polytype behavior of the growing NW. The existence of WZ or ZB crystal structures is currently interpreted by the amount of contact angle between the droplet and the NW side planes.

2.2 Be-doped GaAs nanowires

Semiconductor NWs are integrated into many electronic devices by exploiting and tailoring their electrical properties by doping. In conventional MBE, *in-situ* n-type and p-type doping is possible by introducing different dopant precursors during the growth process, but the incorporation of impurities is rather challenging. The process may follow different routes, some of which are still under serious criticism. Common belief is that dopant atoms can alloy with metallic nanoparticles and mitigate within the semiconductor crystal via a "comet-trail" effect. p-type Si doping in Au-induced GaAs NWs was first reported by Piccin et al.[72]. Later it was realized in self-assisted NWs[73]. Author suggested incorporation pathways for the impurities: one from the Ga droplet and one from lateral overgrowth.

Doping with Be was consistently found to yield p-type behaviour for Au-induced GaAs NWs[74,72]. In this work, we have used Be-doped GaAs NWs, with different doping concentrations to gain a comprehensive understanding of Gorsky effect at the nanoscale. More details are provided in Chapter. 6. These NWs were grown at PDI Berlin and they also reported the Be incorporation in self-induced GaAs NWs by means of Raman scattering[75]. The dominant incorporation of Be atoms was observed at Ga sites by using Raman spectroscopy in self-induced GaAs NWs. Similarly as the planar growth of GaAs, Be dopant atoms are incorporated as acceptors on Ga lattice sites Be_{Ga}leading to p-type conductivity[76]. At high doping levels, indications of Be at interstitial sites were also found . Higher Be doping concentrations cause a morphological modifications in NWs, with pronounced kinking and tapering[75].

Casadei et al.[77] reported that the incorporation of the Be atoms during the doping starts from the side facets while the incorporation through the Ga droplet is negligible. Doping profile of the NW depends also on the diffusion rate of the Be atoms during the growth of the NW[78]. There is a concentration of Be adatoms on the side facets that will diffuse into NW during the axial growth[53,73]. Due to the constant Be flux, the concentration of the adatoms on the surface is also kept constant to achieve a homogeneously concentration during the growth, p_0 and thus the diffusion is driven by the gradient of Be concentration[79].

$$p(x,t) = p_0 \times erfc\left(\frac{x}{2\times(Dt)^{\frac{1}{2}}}\right) \tag{2.2}$$

Here p_0 is the doping concentration at the surface, x is the distance from the surface is the diffusion time, and D is the diffusion coefficient.

$$D = D_0 \times e^{-\frac{E_0}{kT}} \tag{2.3}$$

where for Be diffusion in bulk GaAs, $D_0 = 0.655[cm^2/s]$, activation energy $E_0 = 2.43$ [eV][79]. Considering a growth temperature $T = 790[C°]$ a diffusion coefficient of $1.9816 \times 10^{-12}[cm^2/s]$ for Be atoms in GaAs is expected. This yields 1 minute for a diffusion distance of 107[nm] which means that core doping should be expected in the grown NWs. Since Be is the lightest p-type dopant for GaAs, core incorporation of the dopant atoms can be accomplished with relatively less lattice damage. Two types of principal intrinsic point defects exist in GaAs lattice, i.e., vacancy and interstitial, with six possible configurations: vacancies on both sublattices (V_{Ga} and V_{As}), Ga and As interstitials (Ga_{in} and As_{in}) and antisites (As_{Ga} and Ga_{As})[80]. Both interstitial and substitution doping contribute to a distortion of the atomic volume in the proximity of Be atoms and change the volume V of GaAs NW. This change is estimated by considering the bond length and subsequently the lattice parameter variation of host lattice[81]. Core Ga atom substituted by one Be atom yields a bond length of Be–As is smaller than Ga–As bond due to the much smaller size of Be atom as compared Ga. This leads to a decrease of lattice parameter which is related to the partial molar volume V_M of point defects in the GaAs NW by[81]

$$\frac{a_{Be} - a_{GaAs}}{a_{GaAs}} = c\frac{V_M}{N_A V_{mean}} \tag{2.4}$$

Here, a_{Be} is lattice parameter of Be, a_{GaAs} is lattice parameter of GaAs, c is an atomic fraction of Be atoms, V_{mean} is mean atomic volume and N_A is Avogadro's number. Be substitutional doping causes the lattice constant declining by 0.79% and the volume declining by 2%[82], which accounts to partial molar volume equal to $4.0575 \times 10^{-24}[cm^3]$. Precise doping concentration in Be doped GaAs NWs or even the equilibrium concentration of point defects in GaAs is a complicated function which depends on temperature, Fermi-level position and activation energy. Goktas et al.[83] reported inconsistent carrier concentration with respect to nominal concentration in Be doped GaAs NWs. These NWs were grown by VLS and the carrier concentration was measured by diverse experimental techniques. In this thesis, we have used Be doped GaAs NWs with two different nominal doping concentration i.e. $1 \times 10^{18}[1/cm^3]$ and $1 \times 10^{19}[1/cm^3]$. However, exact doping gradient is unknown and concentration profile is varied one order for the optimization.

2.3 Elastic properties of GaAs

Elasticity is the property of a material that forces it to return to its original shape as soon as the external stress causing the deformation has been removed. Elasticity in materials originates from a slight shift (< 1-3 percent usually) in the interatomic distance under the external stress, which induces a small interatomic force that tends to be restored. As long as the atomic structure is not altered, the atoms will adapt back to their original unstrained position after the external force (load) has been removed. For bulk materials, the linear elastic theory of solids works perfectly and it works well down to a few nm in the framework of micro-nanomaterials with reduced dimensionality. Below 10[nm], the interatomic

distance is comparable to the dimension of the the nanoobject and thus the assumption of continuum of classical elastic theory does not hold. Similarly, surface effects such as surface tension force are not negligible at low dimension but rather play a dominating role compared to bulk materials where such effects are simply neglected. Given the fact that different phases of structure coexist in the NWs and due to structural transition the response of interatomic forces can change thus their elastic properties. In this manuscript, we used the Young's modulus of bulk zinc blende (ZB) GaAs NWs and wurtzite (WZ) GaAs NWs as derived from their stiffness tensors considering that the typical size of NWs is justified in the framework of continuum elasticity.

2.3.1 Elastic properties of Zinc-blende crystal structure in GaAs

Stiffness tensor $C_{ZB,ij}$ of ZB GaAs in the cubic crystal reference frame is given as:

$$\left[C_{ZB,ij}\right] = \begin{bmatrix} C_{11} & C_{12} & C_{12} & 0 & 0 & 0 \\ C_{12} & C_{11} & C_{12} & 0 & 0 & 0 \\ C_{12} & C_{12} & C_{11} & 0 & 0 & 0 \\ 0 & 0 & 0 & C_{44} & 0 & 0 \\ 0 & 0 & 0 & 0 & C_{44} & 0 \\ 0 & 0 & 0 & 0 & 0 & C_{44} \end{bmatrix} \tag{2.5}$$

where the elastic constants are $C_{11} = 124.2$ [GPa],$C_{12} = 51.4$ [GPa], $C_{44} = 63.4$ [GPa][23].

For a cubic system, directional Young's modulus in the direction of interest can be calculated by knowing the relevant directional cosines[84].

$$\frac{1}{E_{[111]}} = 2\left[(S_{11} - S_{12}) - \tfrac{1}{2}S_{44}\right](l_1^2 l_2^2 + l_2^2 l_3^2 + l_1^3 l_1^2) \tag{2.6}$$

$$S_{ij} = inv(C_{ij}) \tag{2.7}$$

Here $E_{[111]}$ is the elastic modulus along the growth direction of the ZB GaAs NW and defined by directional cosines as $(l_1, l_2, l_3) = (0.577, 0.577, 0.577)$ which results into 149 [GPa].

2.3.2 Elastic properties of Wurtzite crystal structure in GaAs

Stiffness tensor $C_{WZ,ij}$ for WZ hexagonal GaAs in the orthogonal reference frame related to the hexagonal reference frame is given as:

$$\left[C_{WZ,ij}\right] = \begin{bmatrix} C_{11} & C_{12} & C_{13} & 0 & 0 & 0 \\ C_{12} & C_{11} & C_{13} & 0 & 0 & 0 \\ C_{13} & C_{13} & C_{11} & 0 & 0 & 0 \\ 0 & 0 & 0 & C_{44} & 0 & 0 \\ 0 & 0 & 0 & 0 & C_{44} & 0 \\ 0 & 0 & 0 & 0 & 0 & \frac{C_{11}-C_{12}}{2} \end{bmatrix} \tag{2.8}$$

where the elastic constants are $C_{11} = 147.6$ [GPa], $C_{12} = 46$ [GPa], $C_{13} = 33.4$ [GPa], $C_{44} = 42.2$ [GPa][23]. The growth axis of WZ GaAs is along [001] direction and the Young's modulus along that direction is $\frac{1}{S_{33}}$. From the calculations, it is found that the Young's modulus of WZ GaAs along [001] is equal to the Young's modulus of ZB GaAs along [111] , i.e, 149 [GPa].This makes perfect sense considering the close relationship between the two structures, which differ only by the stacking sequence along [001] WZ or [111] ZB.

3

Kinematic X-ray Diffraction

X-rays were discovered by the German physicist Wilhelm Conrad Röntgen in 1895. X-rays are a form of electromagnetic radiation and have the capability of passing through solid materials. Röntgen's discovery was a ground breaking scientific bombshell and was received with extraordinary interest by both scientists and the general public. The discovery of X-rays set two new sciences, X-ray crystallography and X-ray spectroscopy, in motion after the revolutionary and sensational discovery of X-ray diffraction by crystals. The experiment was proposed by Max von Laue and its was performed by Walter Friedrich and Paul Knipping, in April 1912 in the Institute of Theoretical Physics at the University of Munich[85]. The discovery of X-ray diffraction by crystals was later confirmed in 1913 by a father-son duo, William Henry Bragg and William Lawrence Bragg, by developing an alternative method of interference when X-rays are interacting with the periodic lattice of a crystal. Max von Laue, for the discovery of X-ray diffraction, and the Braggs, for crystal structure analysis by X-rays, both were awarded Nobel prizes in 1914 and 1915, respectively[86].

In this chapter, we give an overview of the key principles of X-rays Diffraction (XRD) from crystals in the kinematic approximation, a short description of the reciprocal lattice of crystals, and the necessary methods for the crystal structure characterization.

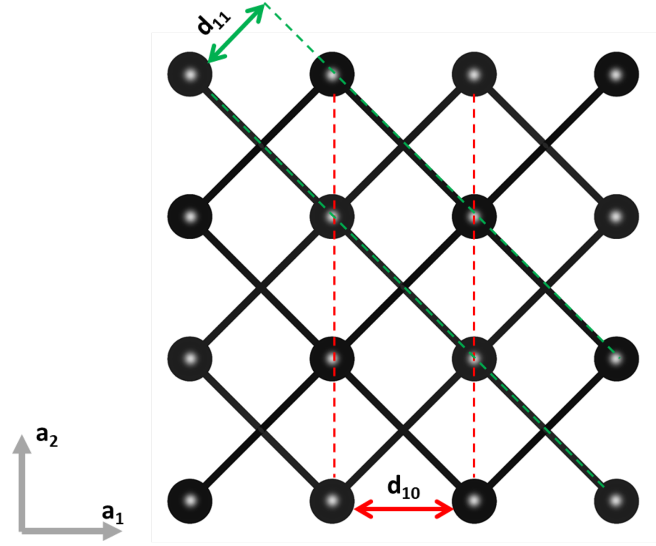

Figure 3.1: Lattice in two dimensional space. d_{10} and d_{11} are representing the distance in between the planes (10) and (11) respectively.

3.1 Crystal planes and reciprocal lattice

A lattice is a mathematical construction that represents a set of regularly arranged imaginary points in three-dimensional space. The position of every point in the lattice to the lattice point selected as the origin, $\boldsymbol{O}$, of the lattice, is uniquely defined by the vector[87]

$$\boldsymbol{R}_{u,v,w} = u\boldsymbol{a}_1 + v\boldsymbol{a}_2 + w\boldsymbol{a}_3 \tag{3.1}$$

Here u,v, and w are positive or negative integers. The vectors $\boldsymbol{a}_1$, $\boldsymbol{a}_2$ and $\boldsymbol{a}_3$are the basis vectors that define cell which is called the unit cell. Three lattice points in space define a crystallographic plane. Planes that are identical and equally spaced to each other construct a family of crystallographic planes. Family of planes is represented by a sequence of three integer numbers called Miller indices **(h,k,l)**. Knowing the lattice constant and the type of Bravais lattice[87], inter-planer distance d of the same family can be estimated with the help of Miller indices. For cubic and hexagonal lattices, the distance between two subsequent planes is given by

$$\begin{gathered} d^c_{hkl} = \frac{a}{\sqrt{h^2 + k^2 + l^2}} \\ d^h_{hkl} = \frac{a}{\sqrt{\frac{4}{3}(h^2 + hk + k^2) + (\frac{a_h}{c_h})^2 l^2}} \end{gathered} \tag{3.2}$$

The angle between two adjacent planes,(h_1, k_1, l_1) and (h_2, k_2, l_2) for cubic and hexagonal crystals[88,89]

$$\cos\Phi^c = \frac{h_1h_2 + k_1k_2 + l_1l_2}{\sqrt{h_1^2 + k_1^2 + l_1^2}\sqrt{h_2^2 + k_2^2 + l_2^2}}$$

$$\cos\Phi^h = \frac{h_1h_2 + k_1k_2 + \frac{1}{2}(h_1k_2 + k_1h_2) + \frac{3a_h^2}{4c_h^2}l_1l_2}{\sqrt{(h_1^2 + k_1^2 + h_1k_1 + \frac{3a_h^2}{4c_h^2}l_1^2)(h_2^2 + k_2^2 + h_2k_2 + \frac{3a_h^2}{4c_h^2}l_2^2)}} \tag{3.3}$$

Any lattice can be visualized with the set of vectors given in Eq. (3.1) in three-dimensional real space. To preconceive the diffraction condition in X-rays Diffraction, it is important to mention the reciprocal lattice of a crystal[90], first introduced by P. Ewald in 1921[90]. Fourier transformation of real space lattice points gives the reciprocal lattice points in the reciprocal space or Fourier space. Analogous to any vector $\boldsymbol{R}$ in real space, a vector $\boldsymbol{G}$ in reciprocal space can be defined as a linear combination of the reciprocal space vectors and Miller indices and fulfills the following condition

$$e^{iG_{hkl}\cdot R} = 1 \tag{3.4}$$

where

$$G_{hkl} = h\boldsymbol{b}_1 + k\boldsymbol{b}_2 + l\boldsymbol{b}_3 \tag{3.5}$$

It is clear from Eq. (3.4) that the scalar product $\boldsymbol{G}.\boldsymbol{R}$ needs to be an integer multiple of 2π. The reciprocal lattice vector $\boldsymbol{G}_{hkl}$ is perpendicular to the planes (hkl) and its magnitude is inversely related to the inter-planer lattice distance in real space

$$\boldsymbol{G}_{hkl} = \frac{2\pi}{d_{hkl}} \tag{3.6}$$

The reciprocal lattice basis vectors are related to the real space lattice basis vectors as

$$\boldsymbol{b}_1 = 2\pi\frac{\boldsymbol{a}_2 \times \boldsymbol{a}_3}{\boldsymbol{a}_1 \cdot (\boldsymbol{a}_2 \times \boldsymbol{a}_3)}$$

$$\boldsymbol{b}_2 = 2\pi\frac{\boldsymbol{a}_3 \times \boldsymbol{a}_1}{\boldsymbol{a}_1 \cdot (\boldsymbol{a}_2 \times \boldsymbol{a}_3)} \tag{3.7}$$

$$\boldsymbol{b}_3 = 2\pi\frac{\boldsymbol{a}_1 \times \boldsymbol{a}_2}{\boldsymbol{a}_1 \cdot (\boldsymbol{a}_2 \times \boldsymbol{a}_3)}$$

3.2 X-ray diffraction

Thomson scattering describes the scattering of X-rays from a single free electron. The amplitude of the scattered wave at distance R is given by[91]

$$A_{rad}(r, R) = r_0 P A_0 e^{i\mathbf{k}_i \cdot \mathbf{r}} \frac{e^{ikR}}{R} \tag{3.8}$$

where P is a polarisation factor which depends on the scattering geometry. r_0 is classical electron radius or Thomson scattering length, k is the wave number equal to $|\mathbf{k}_i| = k = \frac{2\pi}{\lambda}$ for elastic scattering and A_0 is the incident amplitude. We used kinematic approximation where multiple scattering is neglected and the total scattered radiation field is a superposition by a coherent summation[92], specified by the electron density $\rho(\mathbf{r})$

$$A_{rad}(R) = r_0 P A_0 \int \rho(\mathbf{r}) e^{i\mathbf{k}_i \cdot \mathbf{r}} \frac{e^{ik|r-R|}}{|r-R|} d\mathbf{r}. \tag{3.9}$$

The Fraunhofer approximation can be applied to Eq. (3.8) as the distance R between the sample and detector is much larger compared to the size of the illuminated crystal. In this case, both primary and scattered waves are considered, plane wave and Eq. (3.8) becomes

$$A(\mathbf{q}) = r_0 P A_0 \frac{e^{ikR}}{R} \int \rho(\mathbf{r}) e^{i\mathbf{q} \cdot \mathbf{r}} d\mathbf{r}. \tag{3.10}$$

Here $\mathbf{q}$ is the scattering vector defined as[93]

$$\mathbf{q} = \mathbf{k}_f - \mathbf{k}_i \tag{3.11}$$

Hence, the Fourier transformation of the electron density is proportional to the scattered amplitude. Eq. (3.9) produce sharp Bragg peaks in the reciprocal space for an infinite and perfect periodic crystal as long as scattering vector is equal to reciprocal lattice vector $\mathbf{q} = G_{hkl}$, known as diffraction (or Laue) condition. The description of the diffraction condition is equivalent to *Bragg's law* which is the condition for the constructive interference of X-rays, with a wavelength comparable to atomic spacing, which has an incident angle θ to a set of lattice planes a distance d_{hkl} apart

$$\lambda = 2 d_{hkl} \sin \theta_B \tag{3.12}$$

Here θ_B is the Bragg angle[93]. At Bragg condition, each set of planes serve as a Bragg peak or Bragg reflection in the reciprocal space. By employing the translational symmetry for a crystal of finite size the integral can be replaced by a summation over all electrons.

$$r = r_{cell} + r_n + r_n' \tag{3.13}$$

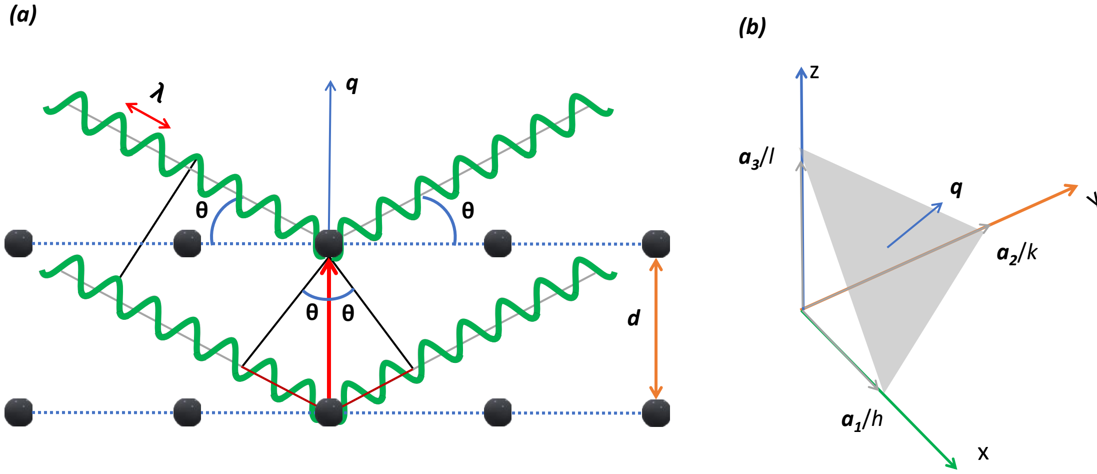

Figure 3.2: Incident x-ray beam diffracted from a crystalline sample. **a.** shows the geometry for the Bragg condition. Condition for the constructive interference will be fulfilled only along the vector **q**. **b.** shows a lattice plane with Miller index, h, k, l in **Q** space.

where r_{cell} is the position of the different unit cells in the crystal, r_n is the position of atom n in the unit-cell and r'_n describes the electron distribution around atom n. This replaces the integral by a summation of all atoms in the unit cell and a sum over all unit cells[94].

$$A(\mathbf{q}) \propto \sum_n \underbrace{\left(\int \rho(\mathbf{r}'_n) e^{i\mathbf{q}\cdot\mathbf{r}'_n} d\mathbf{r}'_n \right)}_{\text{Atomic form factor } f_n(q)} e^{i\mathbf{q}\cdot\mathbf{r}_n} \sum_{cells} e^{i\mathbf{q}\cdot\mathbf{r}_{cell}}$$

$$= \underbrace{\sum_n f_n(q) e^{i\mathbf{q}\cdot\mathbf{r}_n}}_{\text{Structure factor } F(q)} \underbrace{\sum_{cells} e^{i\mathbf{q}\cdot\mathbf{r}_{cell}}}_{\text{lattice sum}} \tag{3.14}$$

Here, the first term is the unit cell structure factor which determines the intensity of the Bragg peak. The second term is a sum over the lattice cells which identify the possible locations of reflection in the reciprocal space. Scattering amplitude is non-vanishing if and only if $\mathbf{q} = G_{hkl}$. This is also called *Laue condition* for the observation of the diffraction pattern from a crystalline lattice which regarded as completely equivalent to *Braggs Law*. The diffracted intensity I is given by[95,92]

$$I = A(\mathbf{q}) \cdot A^*(\mathbf{q}) \tag{3.15}$$

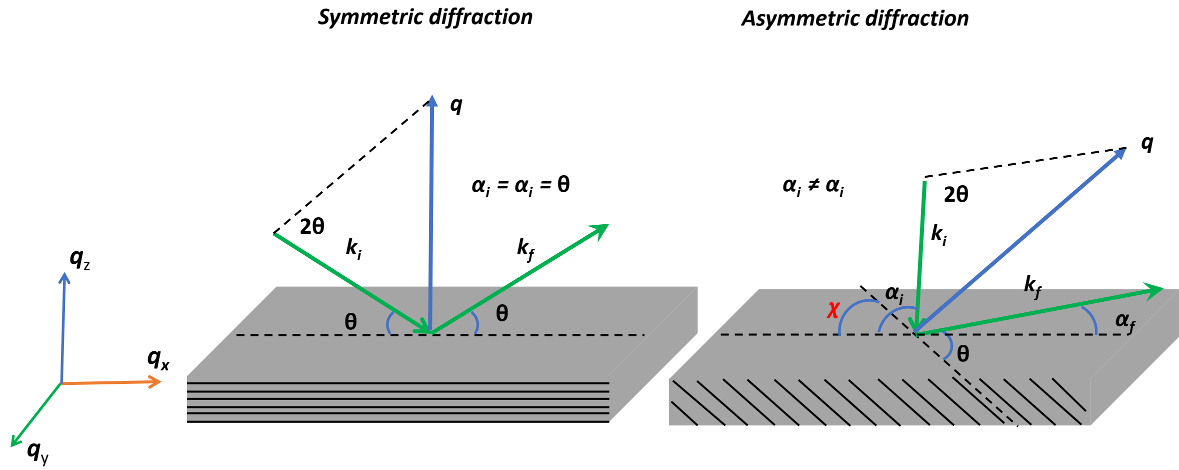

Figure 3.3: a. Symmetric and **b.** asymmetric diffraction geometry. In symmetric diffraction geometry incident beam illuminate the lattice planes parallel to the surface of the crystal. While in asymmetric case, Bragg's law is fulfilled at lattice planes inclined by an angle with respect to the surface.

3.2.1 Diffraction geometries

For a typical XRD experiment, one generally aims at recording the diffracted intensity in a particular region of the reciprocal space. This implies tuning the incident angle ω, and the detector position such that the momentum transfer $\mathbf{q} = k_f - k_i$ maps a specific region in the reciprocal space around the reciprocal lattice vector G_{hkl}. Depending on the nature of experiment different diffraction geometries can be employed, such as the coplanar symmetric and asymmetric reflection geometries. In this work, experiments have been carried out in a quasi coplanar diffraction geometry where the illuminated set of planes are ideally parallel to the sample surface and the scattering angle is determined by 2θ.

In diffraction geometry, the scattered wave (k_f) remains in the plane specified by the incoming X-ray beam (k_i) and the surface normal to the sample. Two possible diffraction geometries are shown in Fig 3.3. In the symmetric diffraction geometry, the selected lattice planes are parallel to the sample surface, while in the asymmetric diffraction geometry they are inclined to the sample surface by an offset angle Φ. Asymmetric reflections can be obtained if $\Phi > 2\theta$ and the Bragg condition can be satisfied in grazing incidence geometry $(2\theta - \Phi)$ and grazing exit geometry $(2\theta + \Phi)$. To diffract at the Bragg angle, generally a set of planes are rotated around the surface normal for the alignment. The component of the scattering vector can be decomposed by using the incident and exit angle of the x-ray beam on the sample surface and the scattering angle ν in the detector plane perpendicular to exit angle 2θ[96].

$$q_x = \frac{2\pi}{\lambda}\left(\cos(2\theta - \omega) \cdot \cos \nu - \cos \omega\right)$$

$$q_y = \frac{2\pi}{\lambda} \sin \nu \tag{3.16}$$

$$q_z = \frac{2\pi}{\lambda}\left(\sin(2\theta - \omega) \cdot \cos \nu - \sin \omega\right)$$

$q_z$is out of parallel to the surface normal of the sample while q_x is parallel to the projection of the incoming X-ray beam on the surface. q_y is the in plane component of scattering vector , perpendicular to q_x

3.2.2 Reciprocal space mapping

Reciprocal space mapping (RSM) or the measurement of the scattered intensity in the reciprocal space around the Bragg reflection are usually recorded employing two-dimensional X-ray detectors (see Fig 2.6(a)). Such detectors allow to simultaneously measure the intensity distribution for a small range of 2θ and ν. Each pixel on the detector corresponds to a direction of the scattered wave and represents to a point in the reciprocal space. A plane constructed in the reciprocal space by using Eq. 3.16 is corresponding to a single image taken at a fixed incident angle. To reconstruct three-dimensional RSM consecutive images are taken at different incident angles, below or above the Bragg peak while keeping the detector stationary[97,98]. This method is known as Theta scan or Rocking curve method and depicted in Fig. 3.4.

Another method to record the 3D intensity distribution[98], called theta-two theta scan, scans the angle of incidence and detector angle with respect to the primary beam simultaneously. In this case the plane cut by the detector will cut the planes from 3D RSM and follow a different trajectory compared to the theta scan.

It is also possible to reconstruct the 3D RSM by continuously changing the wavelength of the X-ray beam[98], usually known as energy scans. In this method, the incident beam and diffracted beam change symmetrically with respect to the scattering vector along which the detected frames are stacked for the 3DRSMs recording.

3.3 Bragg Coherent Diffraction Imaging

In a typical XRD experiment, the scattered intensity is recorded on a two-dimensional matrix detector. The three-dimensional intensity distribution in the vicinity of a given Bragg peak is recorded by vary-

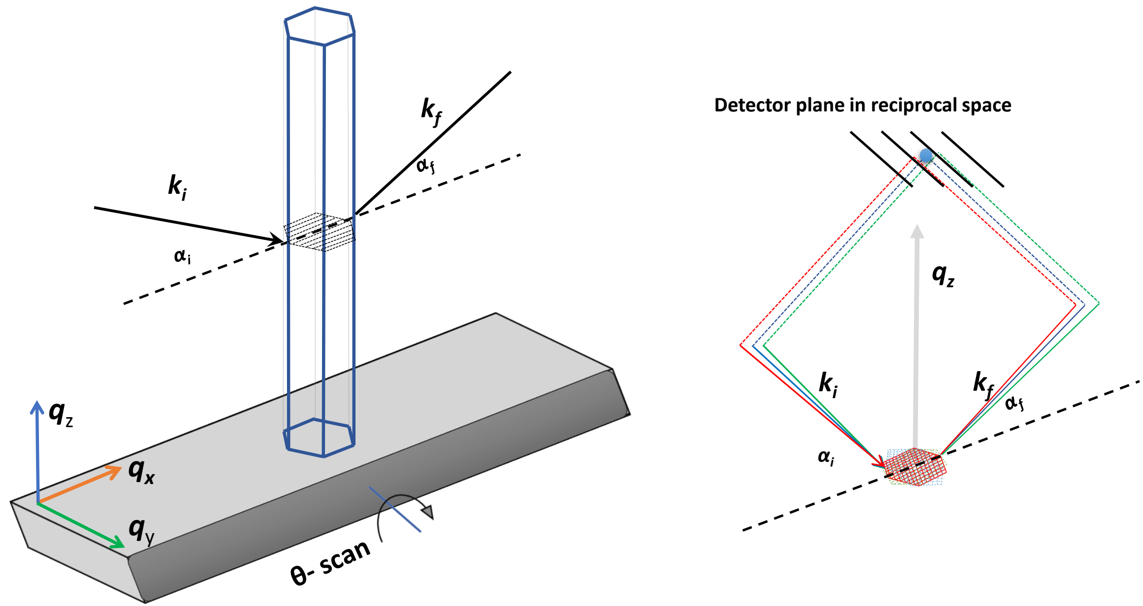

Figure 3.4: **a.** A rocking θ-scan around the 111 Bragg angle of GaAs. **b.** The lines in detector plane represent the reciprocal space at angles less, equal and larger than the Bragg angle.

ing either the incident angle or the energy of the incident X-ray beam. To obtain coherent 3D-RSMs, fully coherent X-ray beams are needed as they are provided by state-of-the-art synchrotron sources. The coherence length has to be larger than the object size and the beam size is smaller than that coherence length.

3.3.1 Coherence

X-ray beam originating from identical sources will be a coherent beam when

- It is monochromatic
- It has identical phase
- It has identical amplitude

The phase difference between the different points within the illuminated volume will be constant with respect to time as the incident X-ray beam is always assumed to be a plane wave with constant phase, i.e. a fully coherent beam. In other words, the fringes in the diffraction pattern are observed with a high contrast for the phase retrieval. However, in reality, X-ray beam is not exclusively monochromatic and it does not propagate ideally. These fluctuations in time and space lead to such a X-ray beam where different segments are more correlated than others. Coherence of a beam is specified by the magnitude

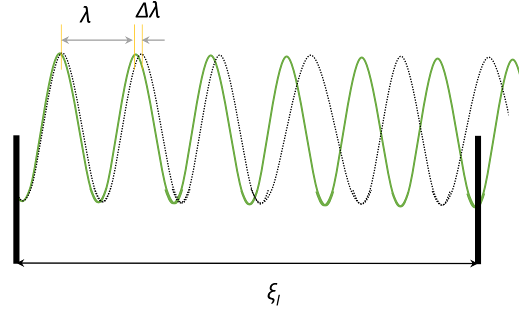

Figure 3.5: Two plane waves with slightly different wavelengths propagate in the same direction. Image obtained from Ref.[4]

of this correlation. The degree of coherence can be expressed by *Visibility* and defined as the difference between minima (Imin) and maxima (Imax) in the diffraction pattern.

$$Visibility = \frac{I_{max} - I_{min}}{I_{max} + I_{min}} \tag{3.17}$$

Generally, the amount of correlation varies along the longitudinal and transverse direction with respect to the propagation direction and thus the coherence of X-ray beam can be described via two different coherence lengths – longitudinal and transverse. They depend on the monochromaticity of the X-ray beam and on the source size seen from the scattering object.

To visualize the impact of longitudinal coherence, consider two wavefronts with two wavelengths $\lambda, \lambda + \Delta\lambda$ in a double slit diffraction experiment. The observed fringes at the detector will have a reduced contrast as depicted in Fig. 3.6. To obtain a reasonable contrast, longitudinal coherence is defined as a distance in space where the phase difference of the two waves is less than π. It infers that for the same distance, the second wave is oscillating $N - 0.5$ times if first wave is oscillating N times[4].

$$\xi_l = \frac{\lambda^2}{2\Delta\lambda} \tag{3.18}$$

For spatial coherence, imagine the finite size and a point shape X-ray source. Monochromatic beam will produce discrete interference fringes, i.e., the intensity will be zero in between the fringes (Visibility=1)[99]. In general, X-ray source is not point-like and laterally elongated sources will reduce the contrast because different parts of the source will produce patterns that are shifted with respect to each other. Transverse coherence length is[4]

$$\xi_t = \frac{\lambda R}{2w} \tag{3.19}$$

Where R is the source to slits distance and w is the height of the source. For a reasonable contrast, the phase difference has to be less than π which yields a factor $1/2$ for the transverse coherence length. In BCDI coherently scattered radiation intensity, the absolute square modulus of the diffraction amplitude can be exploited to extract the complex density function of the measured crystal with the help of Inverse

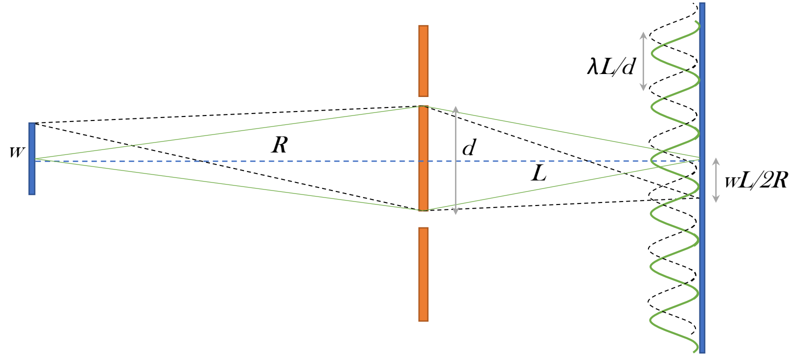

Figure 3.6: Two plane waves with the same wavelength radiated by the source of the size w propagate at some offset angle. Image obtained from Ref.[4]

Fourier Transformation (IFT) and phase retrieval algorithms rendering possible the 3D visualization of the shape of the crystal, as well as the strain and defect distribution of the nanostructure. Thus, BCDI greatly relies on the computational methods to recover phase information and compared to other conventional imaging techniques that require an objective lens between the object and the detector[100,101], BCDI is a lens-less technique and consequently, providing the best spatial resolution of $8-10$[nm][102,32] depending upon the size of the RSM measured around the Bragg peak.

In the recent past, numerous methods have been proposed to retrieve the full information of the sample's amplitude and phase from a measured intensity pattern numerically. The reconstruction of the phase information is based on the measured scattered wave amplitude of diffraction and certain constraints which results in a complex electron density function[103,104,105,106,107]. Information regarding the shape of the crystal, strain and defect distribution can be successfully determined by using the reconstruction of the three-dimensional amplitude, if the illuminating X-ray beam is coherent and the scattered photons make an interference pattern that has high visibility.

3.4 Scanning X-ray diffraction microscopy

Scanning x-ray diffraction microscopy (SXDM) combines X-ray diffraction with focused X-ray beams for continuous and fast two-dimensional real space mapping of the sample. Knowing the material structure of the sample, SXDM can be used to localize nanostructures of interest and to examine the structural composition. Real space maps are extracted by translating the sample across the focused X-ray beam, from where it is diffracted into the detector. At every point of translation along and perpendicular to the x-ray beam, the sample is rocked and the scattering intensities are recorded as a function of the real space position in the fashion of a scanning probe microscope. With a nanometer focused x-ray beam fast SXDM allows for a detailed evaluation of of local strain with a strain resolution of 10^{-5} and spatial resolution of 50[nm][108]. We have used SXDM to identify the regions of interests as well as the NWs which have to be studied by X-ray diffraction. As discussed earlier in 2.1.3, GaAs NWs grown by MBE

have both cubic ZB and hexagonal WZ phase along the growth direction, due to small difference in lattice parameters makes the angular separation between the Bragg angles of ZB and WZ is also small in Q-space. Thus,SXDM, which is non-invasive in nature and sensitive to the lattice parameter and crystal phase structures along the probed volume, can be applied to find the NWs which mostly consists of ZB or WZ segment by identifying the respective segment offset Δq_z.

4
Experimental methods

In this chapter, the experimental techniques and instrumental setups are briefly described. The first section is dedicated to the combination of scanning electron microscopy and focused ion beam microscopy in a single instrument, dual beam Focused Ion Beam /Scanning Electron Microscopy (FIB/SEM). This instrument is used for the primary characterization of the samples and as well as for their preparation for further studies. The experiments were carried out by employing a Helios NanoLab™ 600 dual FIB-SEM system at the Micro-and Nanoanalytics Facility (MNaF) of the University of Siegen. The second section introduces the operational setup and functionality of the custom-built *in-situ* atomic force microscope "Scanning Force Microscope for in situ Nanofocused X-ray diffraction (SFINX)" which was developed for *in-situ* nano-mechanical studies in combination with nanofocused X-ray diffraction techniques at 3rd generation synchrotron sources. Static three point bending tests and anleasticity test were performed with this tool at "Mechanics of Nano-objects" (MNO) research group at IM2NP at Aix-Marseille University.

4.1 Dual Beam Focused Ion Beam / Scanning Electron Microscopy (FIB/SEM) system

A dual beam microscope integrating both a Focused Ion Beam (FIB) and a Scanning Electron Microscopy (SEM) in a single instrument, which is schematically illustrated in Fig. 4.2.

It consists of one column for the acceleration and focusing of electrons and a second column that is inclined by 52° with respect to the first one for the acceleration and focusing of ions. Electrons are

emitted either thermionically from a cathode such as a tungsten filament or LaB6 cathode, or by field emission. For a field emission source, a fine, sharp, single-crystal tungsten tip is employed giving a more coherent beam and higher brightness than the tungsten filament. There are also so-called cold emission sources where the heating of the filament is not required as it operates at room temperature. However, this type of filament is prone to contamination and requires more stringent vacuum conditions as well as regular and rapid heating ('flashing') to remove contamination. Other field emission sources, known as thermal and Schottky sources, operate with lower field strengths. The Schottky source is also heated and dispenses zirconium dioxide onto the tungsten tip to further lower its work function. The electrons are then accelerated by a voltage applied between the cathode and an anode which is a metal plate with a hole in its center. Typical energies for SEM range from 0.2 to 30[keV]. Thereafter, the electrons pass through a magnetic lens system that directs the path of the electrons and focuses the electron beam. The last part of the electron column consists of deflector coils that allow for scanning the electron beam. The electron beam is focused down to a spot about 0.4[nm] to 5[nm] in diameter by using condenser lenses. The typical scanning range is in the order of ten micrometers. SEM imaging is done by detecting the scattered or emitted electrons. Each pixel corresponds to the number of collected electrons by using Secondary Electrons (SE) detector and/or Back Scattered Electrons (BSE) detector. Secondary Electrons are the results from the inelastic interaction, while Back Scattered Electrons from elastic interactions and the images formed with them will have different contrast. The spatial resolution in the SEM is below 1[nm] with an ideal sample, beam size, the electron penetration depth, and the acceleration voltage inside the microscope. For semiconductor NWs, the spatial resolution can be improved by using higher acceleration voltage, which increases the penetration depth and decreases the signal to noise ratio for SE detector.

The FIB setup uses a focused beam of Ga^+ ions instead of a beam of electrons to image the sample in the chamber. Since its invention [109], Focused Ion Beam served as a multifunctional tool for wide range of site-specific applications in multidisciplinary fields, from improving dental implants to the nanotechnology [110,111]. Inside a typical FIB system, the source or ion column is based on Liquid Metal Ion Source (LMIS), Fig. 4.1 - (in-set). Gallium is currently the most common material used for LMIS because of a number of reasons: Gallium is metallic and has low melting point, low volatility, low vapor pressure, and excellent mechanical, electrical, and vacuum properties. In Liquid Metal Ion Source (LMIS), a metal is heated into the liquid state and then it is transferred to the end of a tungsten needle. Here, the opposing forces of surface tension and electric field convert the gallium into a capillary shaped tip, known as Taylor cone. The tip radius of this cone is extremely small, $2nm$. Ga^+ ions escape by field evaporation from the Taylor cone when the electric field exceeds the threshold and enter into the extractor electrodes. Afterwards, inside the ion beam column, ions pass through the two lenses and an array of apertures in between them. The first set of condenser lens is used for the probe-forming and the second objective lens is used to focus the ion beam at the sample. Beam size and ion beam current, in the order of a few pA to as high as 30nA, are defined by the apertures in between the objective and condenser lenses as in Fig. 4.3. Sample stage can move along five-axis (X, Y, Z, tilt and rotation) and its motion can be automatized for

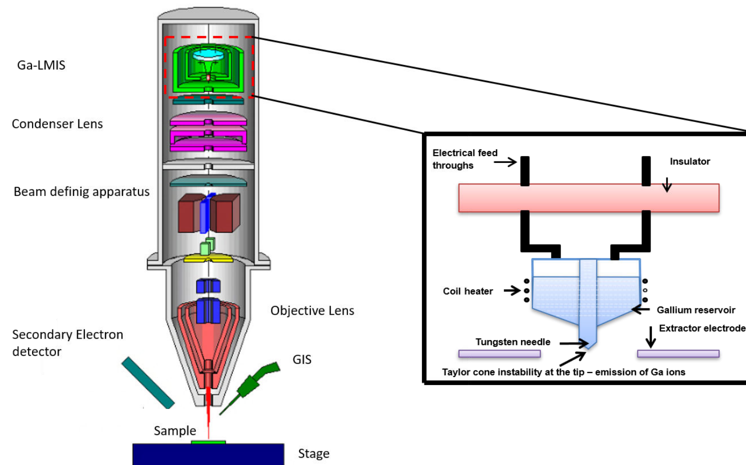

Figure 4.1: Schematic representation of ion beam column dual FIB-SEM inside of a vacuum system. In-set shows the apparatus setup for Ga-LIMS [5]

positioning. The FIB/SEM system is equipped with a gas injection channel that can be used for *in-situ* material deposition on the sample. It provides site-specific deposition of metals like *C* (insulator) or *Pt* (conductor) by chemical vapor deposition for sample preparation, e.g., TEM lamella and soldering of nanoobjects to the collection probe [112]. The working principle involves the insertion of a precursor gas of the deposition material into the microscope via a guided system, shaped like a hollow needle. The precursor adheres to the sample surface through Van der Waals forces [113]. The precursor shell can be decomposed by ion beam for *in-situ* chemical vapor deposition [114]. The metal deposited is amorphous. Either a multichannel plate or an electron multiplier detector is used to collect secondary electrons for imaging in the FIB chamber.

The combination of SEM and FIB gives the flexibility of on-site tomography, Transmission Electron Microscopy (TEM) lamella preparation, surface and cross-sectional imaging and creating fully functional nanoscale prototype devices [115]. As required, FIB and SEM may be employed either simultaneously or separately.The layout of the dual beam (FIB/SEM) chamber is illustrated in Fig. 4.3. Most of the theoretical explanations are taken from [5].

4.2 Scanning force microscopy of *in-situ* nano-focused X-ray diffraction

As mentioned earlier, the "Mechanics of Nano-objects" (MNO) research group at IM2NP at Aix-Marseille University developed a worldwide unique **atomic force microscope (AFM), called** Scanning Force Microscope for in situ Nanofocused X-ray diffraction (SFINX), that is compatible with the 3rd generation synchrotron end-stations [27]. Fig. 4.5 presents the basic layout of the SFINX. The AFM consists in total of five long-range piezoelectric stages (12[mm] stroke) and three short range piezoelectric scanner motors with a range of x = y = 40[µm] and z = 24[µm]. This large number of motors facilitates the alignment

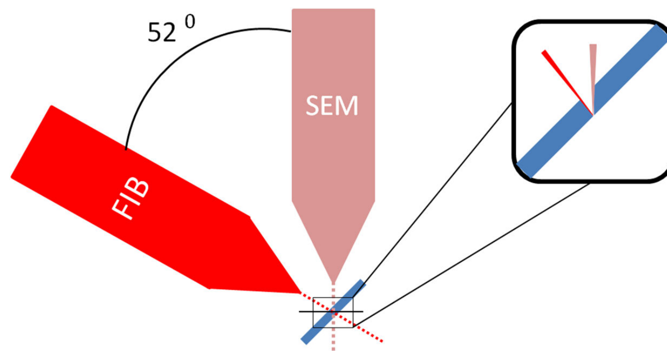

Figure 4.2: Schematic representation of dual beam system. FIB column has a 52^0 tilt with respect tot vertical SEM column at single "coincident" point on sample. Inset shows the real time monitoring of milling on sample by FIB cross-section with *in-situ* SEM imaging.

Figure 4.3: Basic experimental layout of the FEI™ Helios NanoLab™ 600 dual FIB-SEM inside of a vacuum system.

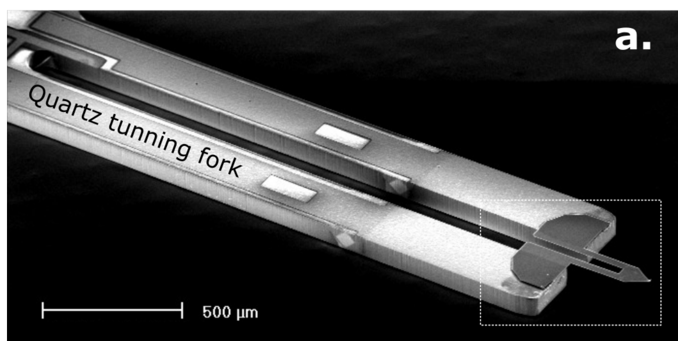

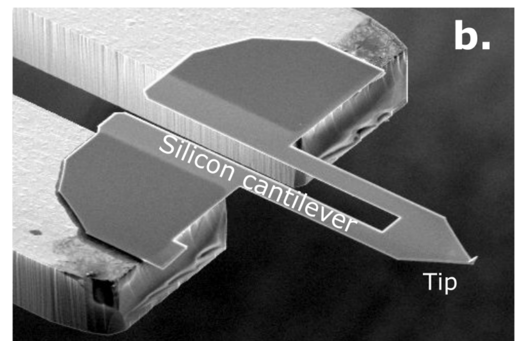

Figure 4.4: a. SEM image of the Akiyama probe consisting of a quartz tuning fork and a Si cantilever tip. **b.** Magnified image of Si cantilever tip. Image is adopted from [6]

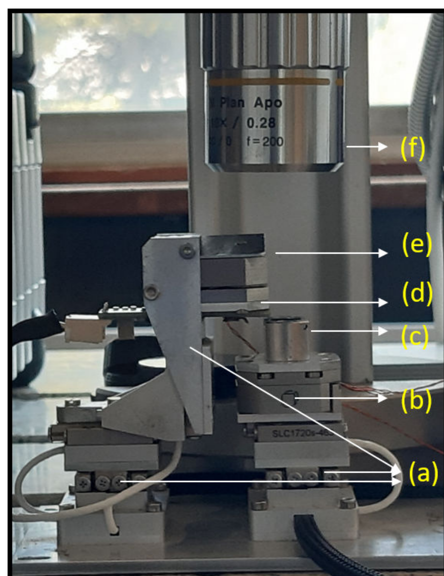

Figure 4.5: Basic layout of the Scanning Force Microscope for in situ Nanofocused X-ray diffraction (SFINX) **a.** two long-range piezo linear translation stages, **b.** xy-piezo scanner, **c.** sample stage ,**d.** z scanner, **e.** AFM cantilever and **f.** optical microscope

of the AFM-tip with respect to the nanostructures as well as the alignment of both the tip and the sample with respect to a nanofocused X-ray beam at synchrotron beamlines. Two long-range piezoelectric stages are mounted below the sample stage, while the other three stages support the AFM-head which consists of a vertical z-scanner unit for AFM topography imaging and the AFM cantilever. The lateral piezoelectric scanner motors are installed on the sample stage. The separation between the lateral and vertical scanner motors improves the stability of the system. As AFM cantilever, a self-actuating and self-sensing Akiyama probe was chosen, which combines a quartz tuning fork and a Si cantilever [116,117], see Fig. 4.4 . This AFM probe makes the laser feedback system used in most commercial systems unnecessary and, thus makes the whole system more compact. The trade-off of this compactness is the lacking of deflection sensitivity of the cantilever and, thus, of a direct force measurement. SFINX is operated in frequency modulated mode and AFM images are recorded in tapping mode.

The cantilever is mounted on three long range piezo linear translation stages (a) in Fig. 4.5. To reduce the noise while measuring, z stage (e) in Fig. 4.5 is mounted independently. An additional xy stage (b) in Fig. 4.5 is installed under the sample stage (c) in Fig. 4.5 . This arrangement facilitate independent functionality of the AFM cantilever (d) in Fig. 4.5 and the sample stage and provides the flexibility to align the focused x-ray beam with the AFM tip and the NW. A rough alignment of the AFM cantilever and the NW, with a precision of 10[μm], can be done by optical microscopy (f) in Fig. 4.5 installed above the SFINX. SFINX is operated in tapping mode with frequency modulation in ambient conditions. On electrodes, connected to the tuning fork, the electrical input signal is applied. This driving signal forces the two prongs to vibrate in plane and have opposite phases, meaning that they approach and withdraw from each other. This out of phase vibration induces small vibrations at the adjective Si cantilever which results in a vertical vibration of the tip. Tip and sample interaction at resonance can be monitored by

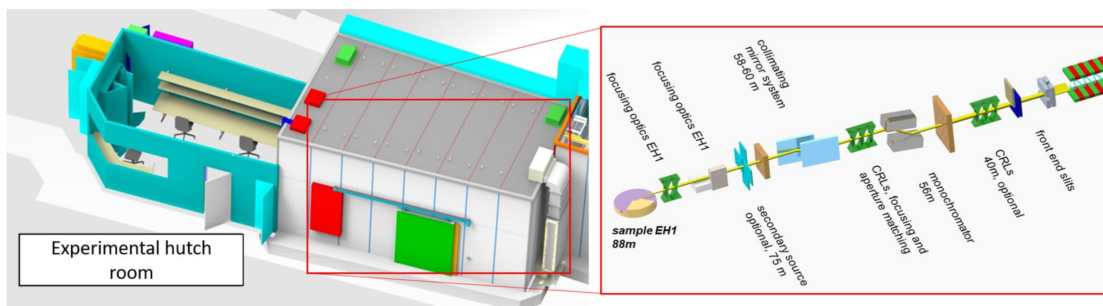

Figure 4.6: Experimental hutch room and scheme of the beamline in P23 beamline,PETRAIII (adapted from Refs.[7]).

measuring the electrical impedance of the tuning fork. Thus only the electrical driving signal is used instead of piezoelectric actuator and no further detection system is needed for imaging.

4.3 P23 beamline at PETRAIII

The beamline P23 in DESY, Hamburg, gives access to a wide range of x-ray diffraction techniques, such as reciprocal space mapping, x-ray reflectivity, x-ray resonant scattering, grazing incidence diffraction. Other forms of scattering and spectroscopy, e.g., powder diffraction, small-angle x-ray scattering, GISAXS, XANES, coherent X-ray diffraction, are still possible with some technical constraints. The beamline source is a spectroscopy sort of undulator providing up to 10^{13} photons per second in the energy range 5[keV] to 35[keV]. In principle, higher energy up to 50[keV] is also accessible but has restricted focusing capability. Focusing optics hutch includes a double crystal monochromator, harmonic rejection mirrors, beam collimation, and two sets of focusing lenses. Beam focusing, beam collimation, and aperture matching are accomplished by Beryllium focusing lenses in the optics hutch that works with the second lens changer in the experimental hutch. The position of the lens changer can be modified with respect to the sample and therefore offering a wide variety of feasible beam spot sizes with demagnification ratios down to 200:1. Beamline facilitates a heavy load $5+2$ circle Huber diffractometer in the experimental hutch with sample cells load capacity up to 150[kg] in horizontal scattering mode and up to 15[kg]on an Eulerian cradle the vertical mode. The available detectors include a state of the art 2D LAMBDA pixel detector with GaAs sensor and a time resolution up to 2[kHz]. Lambda detector consist of an array of 512×1528 pixels with a pixel size of 55×55 [μm^2]. The minimum beam size on the sample can be set on 3(H) × 0.8(V) [μm^2] and 1800(H) × 1200(V) [μm^2] for the maximum beam size[7]. Fig. 4.6 presents a schematic overview of the experimental hutch room at P23 beamline in PETRAIII Hamburg.

5

Electromechanical Resonance In Nanowires

When a NW is perturbed, it will experience vibrations, which emerge at a characteristic natural frequency, the resonance frequency, determined by the geometrical, structural, and mechanical parameters. In our experiments, resonance is attained by applying an AC voltage with a tuneable frequency on one of the side walls of a NW using a nanomanipulator inside a FIB/SEM.
Resonance has been extensively studied in MEMS for mechanical characterization. The first use of Resonance test was to measure the elastic modulus of a nanostructure in the TEM by Treacy et al.[118]. The technique was later integrated by electrostatic excitation[119,120] and it has been extensively used to study electromechanical properties of Nano-electromechincal systems and sensors[120,121,122].

A large number of works[123,124,125] on the mechanical properties of GaAs NWs can be found in the literature, but they mainly focus on uniaxial compression or tensile tests, while studies on the dynamic behavior are scarce. Fewer studies have reported the correlation of NW morphology and its mechanical behavior by employing electromechanical resonance[126,127]. To date, there is no literature available regarding the impact of the dynamic mechanical loading on the different structural phases of NWs. The focus of this chapter is to study the vibration induced mechanical loading on GaAs NWs and to examine the crystalline real structure by using *ex-situ* Bragg Coherent X-rays Diffraction Imaging (BCDI) after a large number of vibration cycles to understand the deformation and mechanical behavior at a fundamental level. Systematic and progressive dynamic loading is thoughtfully performed on single NWs in their as-grown geometry, either by increasing the amplitude of resonance or the dwell time, to investigate the possible correlation between structural properties and the impact of mechanical loading.

5.1 Fundamental theory of Resonance

We study the electromechanical resonances in GaAs NWs in their as-grown geometry. Transverse displacement or vibration in NW is measured with respect to their neutral axis of equilibrium. It is a function of both position along the NW length and time. It is assumed that the NW is homogeneous with length L and a hexagonal cross-section area A. The following Partial Differential Equations (PDE) provides the equation of motion governing the vibrations of the NW[128,129]. It is based on the Euler-Bernoulli beam model, for which the limit of small amplitude of a free vibration rod is governed by the fourth-order wave equation

$$\rho A \frac{\partial^2 X(x,t)}{\partial t^2} = -EI \frac{\partial^4 X(x,t)}{\partial x^4} \tag{5.1}$$

Here ρ is the density, I is the quadratic moment which is $\frac{5\sqrt{3}a^4}{16}$ for hexagonal cross-section of radius a, and E is the Young's modulus. $X(x,t)$ is the transverse deflection of the beam as a function of time and position along its length. To find the eigenvalues (resonance frequencies) and the eigenfunctions (modal shapes), variable separation methods can be used.

$$\begin{gathered} X(x,t) = X(x)F(t) \\ \text{where} \\ F(t) = cos(\omega t + \alpha) \end{gathered} \tag{5.2}$$

using Eq. 5.1

$$\begin{gathered} \frac{\partial^4 X(x)}{\partial X^4} - \frac{\rho A X(x)}{EI} = 0 \\ \frac{\partial^4 X(x)}{\partial X^4} = k^4 X(x) \\ \text{where} \\ k^4 = \frac{\rho A \omega^2}{EI} \end{gathered} \tag{5.3}$$

Eq. 5.3 is a fourth order differential equation and its general solution is

$$X(x) = a_1 \cos kx + a_2 \sin kx + a_3 \cosh kx + a_4 \sinh kx \tag{5.4}$$

a_i are found from the Boundary Conditions (BC). NW has fixed-free BCs.

$$\begin{gathered} X(0) = X^{'}(0) = 0 \\ X^{'}(L) = X^{'''}(L) = 0 \end{gathered} \tag{5.5}$$

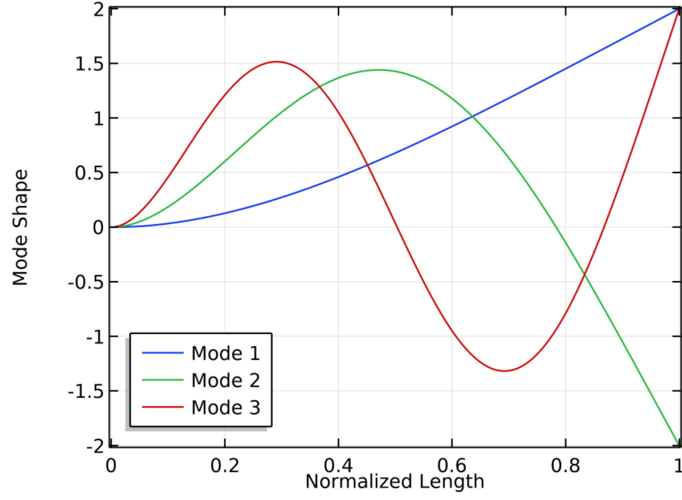

Figure 5.1: Mode shapes of first three vibrational eigenmodes of the NW.

By applying the boundary condition in Eq. 5.4 we have a unique equation that satisfy a discrete set of values for k.

$$\cos kL \cosh kL = 1 \tag{5.6}$$

The roots of the equation correspond to the fundamental eigenmode and $kL = 1.875$. First, three vibrational mode shapes of a NW are shown in Fig. 5.1 Thus, the eigenvalue of a stress-free NW is given by

$$\omega_n = \frac{(k_n L)^2}{L^2}\sqrt{\frac{EI}{\rho A}} = \frac{\beta_n^2}{L^2}\sqrt{\frac{EI}{\rho A}} \tag{5.7}$$

Here$(k_n L) = \beta_n$ and it depends on $n = 1, 2, 3, \ldots .\infty$. For $n = 1$ i.e., β_1, the non-trivial solution $\beta_1 = 1.875$ for first eigenmode and 4.69 for the first harmonic. Electromechanical excitation is achieved in NW by applying a sinusoidal electric signal with a frequency matching to the resonance frequency of the NW. The underlying physics in this dynamic excitation is the electrostatic force originating from the capacitive forces i.e., from the charge interaction between NW and nanomanipulator.

$$F_e = \frac{1}{2}v^2\left[\frac{dC}{dx}\hat{\mathbf{X}} + \frac{dC}{dy}\hat{\mathbf{Y}} + \frac{dC}{dz}\hat{\mathbf{Z}}\right] \tag{5.8}$$

Non-linearity in squared voltage v^2 in electrostatic force can be exploited by coupling a DC voltage, V_{DC}(as off-set voltage) with the AC voltage, where V_{AC} make the fine control of the frequency force

function during the frequency sweep.[119]

$$F_e = \alpha\beta\left(V_{DC} + 2V_{DC}V_{AC}\cos\omega t + \frac{1}{2}V_{AC}^2\cos 2\omega t + \frac{1}{2}V_{AC}^2\right) \quad (5.9)$$

Here ω is the frequency of the AC voltage, t is time, α is a geometrical constant, while β is a proportionality constant. Eq. 5.9 contains both driving frequency ω and double driving frequency 2ω. $V_{AC} \gg V_{DC}$ implies that ω term $\gg$ 2ω term in Eq. 5.9. Thus the term, 2ω, may be neglected if ω is equal to the resonance frequency of the NW. The force function, F_e induces resonance at frequency set to $\frac{1}{2}\omega$, if V_{DC} is zero. For typical diameters ranging from 100 to 200[nm] and lengths of ranging from 4[μm] to 6[μm] are used for the resonance test and the eigenfrequencies are ranging from 3 to 7[MHz] by using the Eq.5.7.

5.2 Damping and its impact on quality factor

Deformation at the nanoscale can be induced by applying a constant or oscillating external mechanical stress. In reality, the amplitude of vibration becomes progressively smaller and smaller in all resonant systems as energy is lost due to friction, also called damping, and it follows an exponential decay pattern. The rate at which the vibration energy is dissipated in the material due to the relaxation processes is called internal friction. It is also commonly known as damping factor. The Quality Factor (QF), Q, predicts the damping factor of the resonator, which is defined as the ratio of the energy stored and the energy loss during one cycle of oscillation in a volume unit of the resonator material. For our measurements, we define Q as the center frequency divided by the Full Width at Half Maximum (FWHM) of the resonance curve[130]. Numerically, it may be estimated as follows

$$Q = \frac{\omega_n}{\Delta\omega_{FWHM}} \quad (5.10)$$

Here ω_n is the experimentally determined resonance frequency.

Next, we will consider various intrinsic and extrinsic damping mechanisms that lead to mechanical energy dissipation in resonance experiments. The total energy dissipation contributes the QF inversely and is the sum of losses from all channels.

$$\frac{1}{Q_{total}} = \sum \frac{1}{Q_i} \quad (5.11)$$

In this section, we discuss the damping due to mechanical energy dissipation, enforced on the resonator by different surrounding channels. The main mechanisms are considered which produce anelastic damping and anelastic relaxation (details in Chapter 6) which are considered as the main source of internal friction. Depending upon their contribution, they may have a sound impact on the QF of the resonator and it becomes essentially important to characterize them explicitly for quasi-static and dy-

namic experiments.[131]

5.2.1 Snoek Effect (Snoek relaxation)

The Snoek effect, first described by Snoek (1941) to explain the damping due to carbon in α-Fe, is an anelastic relaxation caused by the stress-induced drifting of interstitials in the body-Centred Cubic (BCC) metal. On the other hand, isolated interstitial atoms in Face-Centred Cubic (FCC) metals occupy tetrahedral symmetry equivalent interstitial sites, the same as their host lattice and thus the overall symmetry is unaltered. For this reason, the isolated interstitial atoms in Face-Centred Cubic (FCC) metals do not contribute to anelastic relaxation if a stress is applied. Point defect diffusion at low frequencies facilitates internal friction via stress induced reorientation of interstitial atoms. The diffusion may assist the anelastic relaxation and result in mechanical peak loss, i.e., Snoek peak. It can be estimated as a function of the stressing frequency via Debye function:

$$Q^{-1} = \Delta \frac{\omega\tau}{1 + (\omega\tau)^2} \tag{5.12}$$

Here Δ is called the relaxation strength and has a relationship with the internal fraction peak maximum $\Delta = 2 \times Q^{-1}_{maximum}$. Given the fact that the Snoek relaxation time is much smaller due to short range diffusion of interstitials. At any typical excitation frequency in our experiment, a relaxation time of few seconds will yield a QF of order 10^8. Thus it does not contribute to the dynamical damping of the NW.

5.2.2 Thermo-elastic damping

High QF is essential for the higher sensitivity in NEMS and an ultra high QF can be achieved at low temperatures[132,133]. Whenever a NW is bent while vibrating at its resonance frequency, its opposite sides are under tension and under compression, causing a slight expansion and reduction of the crystal lattice accordingly. It induces a nonzero thermal expansion coefficient creating a temperature gradients coupled to the strain gradient. The thermoelastic relaxation is achieved through the irreversible heat flow driven by local temperature gradients that couple to the inhomogeneous strain field. This mechanism of energy dissipation is called Thermo-elastic damping (TED). The thermal expansion coefficient acts as a coupling constant and its non-zero value contributes to the QF. Thermo-elastic damping as source of the dominant damping mechanism was first realized by Zener[134] in 1930. Zener's standard model treats the problem in the framework of anelastic relaxation in solids and predicts that the TED can be

approximated by the characteristic relaxation time and is related to the QF

$$\begin{aligned} Q_{TED} &= \frac{C_p}{E\alpha^2 T_0} \frac{1+(\omega\tau)^2}{\omega\tau} \\ \tau &= \left(\frac{b}{\pi}\right)^2 \frac{C_p}{\chi} \end{aligned} \tag{5.13}$$

In these equations, b is the diameter of the NW with Young's modulus E. C_p is the heat capacity per unit volume at constant pressure, α is the thermal expansion coefficient, χ is the thermal diffusivity, and ω is the resonance frequency of the NW. T_0 is the temperature and τ represents the relaxation time. For $GaAs$ at $T_0 = 300[\text{K}]$, $\alpha = 6.4 \times 10^{-6}[K^{-1}]$, $C_p = 1.78 \times 10^6[Jm^{-3}K^{-1}]$ and $\chi = 2.45 \times 10^{-5}[m^2/s^6]$. The thermo-elastic damping factor for GaAs thus amounts to $Q_{TED} = 2.024 \times 10^4$, which is much larger then the experimental quality factor and hence it is negligible.

5.2.3 Anchor damping

The mechanical connection of the NW to the substrate gives rise to strain while vibrating and thus leads to the dissipation of energy [131]. Such loss of energy is the driving mechanism of nanoscale resonators in flexural modes as the strain is maximum at the mechanical support [135]. The process of energy dissipation at the support through the resonator is called anchor damping and it is temperature independent. Depending upon the mode shape, different vibrational modes have different strain fields and it makes the mediation of elastic wave into the support strongly depend on vibrational mode shape [136,137]. The contribution of anchor damping on the QF of a cantilever beam with rectangular cross-section is approximated by [138]

$$Q_{anchor} \approx 0.31 \frac{w}{l} \left(\frac{h}{l}\right)^4 \tag{5.14}$$

5.2.4 Gorsky relaxation

The Gorsky relaxation is related to the long range diffusion of point defects under a stress gradient, caused by the bending of the material, which induces a gradient in the chemical potential. The point defects migrate under the chemical potential and make a composite profile by accumulating at the maximum compression and tensile regions of the material. The relaxation time for the Gorsky relaxation is given by [139]

$$\tau_G = \frac{d^2}{\pi^2 D} \tag{5.15}$$

Here d is the confined diffusion distance and D is the diffusion coefficient of the point defects. The

Gorsky relaxation time is much larger than the other type of point defect reorientation relaxation (Snoek relaxation), due to the long range of defect diffusion. For this reason, the Gorsky effect must be investigated by the quasi-static anelastic relaxation test. Our results showed that the Gorsky relaxation time for Be-Doped GaAs NWs is in the order of a few minutes. In this case, relaxation time of 300[s] yields a QF equal to 8×10^9 with the excitation frequency of 44[MHz]. In our case, the experimental QF yields a relaxation time of about 40[μs]. Thus, Gorsky is not the origin of observed dynamical damping.

Barois et al.[140], attributed the damping of SiC NWs to the Ohmic losses induced by the electromechanical coupling between charge and mechanical displacement. The influence on the damping rate was studied by varying of the capacitive environment and the applied voltage. Their QF and resonance frequency for Sic NWs have the same order as we observed in our experiment. Thus the damping we observed may be attributed to Ohmic losses.

5.3 Electromechanical resonance in FIB/SEM

Although GaAs NWs have unique geometry and high surface to volume ratio, the stacking of different structural phases along the [111] growth direction differs from one NW to another grown on the same substrate[88], thus affecting the physical properties such as the electrical resistance[141] and size dependent mechanical properties[125]. In this section, we investigate the correlation between NW phase composition and the mechanical properties comparing the changes in real structure of a single NW after the impact of dynamic mechanical loading by vibration tests. Single as-grown pristine GaAs NWs grown by MBE on a Si (111) substrate are electrostatically excited using a micromanipulator in a dual beam FIB/SEM chamber. In the electrostatic excitation technique, an AC voltage with a tunable frequency is directly applied to the NW via a nanomanipulator that serves as a conducting electrode which is connected to a function generator. As schematically depicted in Fig. 5.2, the AC electric field applies an oscillatory force on the side wall of the NW, causing NW to vibrate, when the driving frequency is equal to the resonance frequency of NW.

5.3.1 Imaging and detection in FIB/SEM

Detection and imaging of the vibrational eigenmode is carried out by direct observation inside the dual beam FIB/SEM system. For the imaging the resonance of the NW, the scanning frequency of the detector must be higher than the resonance frequency of NW. To excite the vibrational eigenmode, the nanomanipulator was brought into the proximity of the NW, as shown in Fig. 5.3 - (a). An AC voltage with tunable frequency was applied to the nanomanipulator, resulting in a cyclic force developed between the nanomanipulator and NW. Such electrostatic actuation technique offers a fine control of the frequency force function, which is essential for the determination of the dynamic properties. To observe the resonant frequency, the frequency of AC voltage was manually adjusted. Resonance was directly ob-

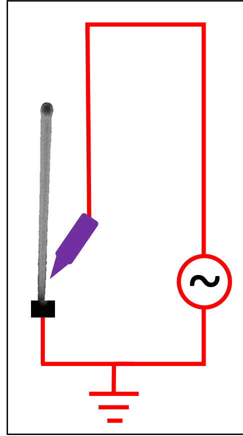

Figure 5.2: Experimental arrangement for electromechanical vibrations in as-grown NWs. An AC pulse was applied to NW.

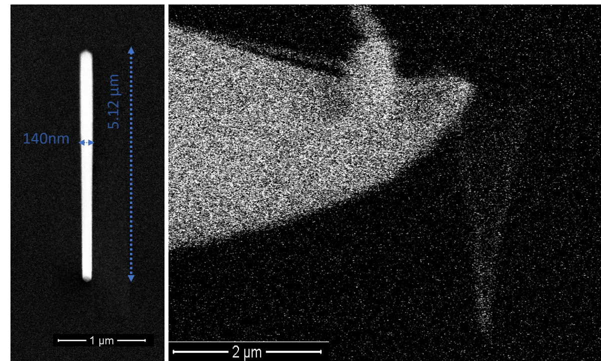

Figure 5.3: **a.** NW before exciation (static state). **b.** Electromechanically induced first eigenmode of vibration in as-grown GaAs NW.

served using SEM via first mode resonant excitation. In Fig. 5.3 - (b) SEM image shows a NW vibrating at the resonance frequency.

We aim at studying the impact of dynamic mechanical loading by vibration tests on the structural phase composition of GaAs NWs. After systematic vibration tests on NWs, structural characterization is carried out by an ex-situ nXRD experiment. More details will come in the next section.

As depicted in Fig. 5.4, two sets of NWs are prepared by varying different parameters during the vibration tests, for the dynamic mechanical characterization. All three NWs set one (NW1L, NW2L and NW3L) are excited for a constant period of time while varying the amplitude of the vibration. For set two (NW1R, NW2R, and NW3R), both time period and amplitude of vibration were varied systematically. NW NW1B was excited for 30 minutes at the maximum observable amplitude of the vibration. In addition to these sets, there is a set of pristine NWs for the direct structural comparison. More details are summarized in the Table.5.1

The eigenfrequencies observed during the SEM measurements are sometimes significantly different

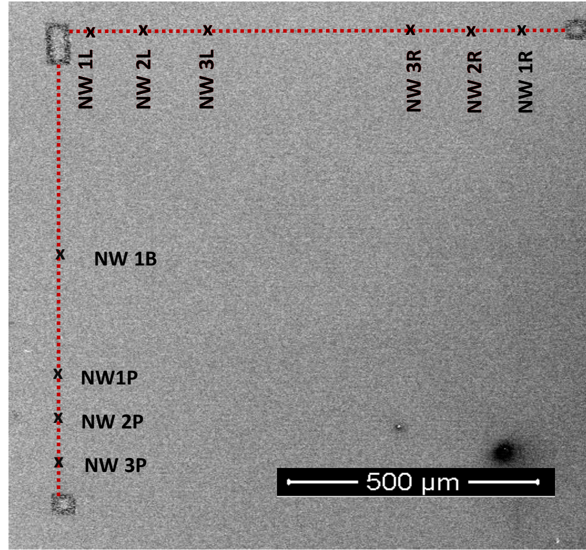

Figure 5.4: SEM image presenting the schematic view of the nanowires in two lines for easy accessibility and alignment.

	NW	Length (\mu m)	Diameter (nm)	Excitation time (min)	ω_{th} (KHz)	Res_{mes} (KHz)
	NW1L	3.9	123.1	15	5470.9	4952.2
SET 1	NW2L	5.14	130.8	15	3346.7	3601
	NW3L	4.14	116.7	15	4602.6	4402
	NW1R	5.52	200	10	4436.9	3490
SET 2	NW2R	5.6	170	15	3664.4	4402
	NW3R	5.12	140	30	3610.1	3786.3
	NW1B	4.49	123.1	30	4127.6	3456.7

Table 5.1: Structural parameters of as-grown GaAs NWs along with their corresponding eigenfrequencies and excitation time.

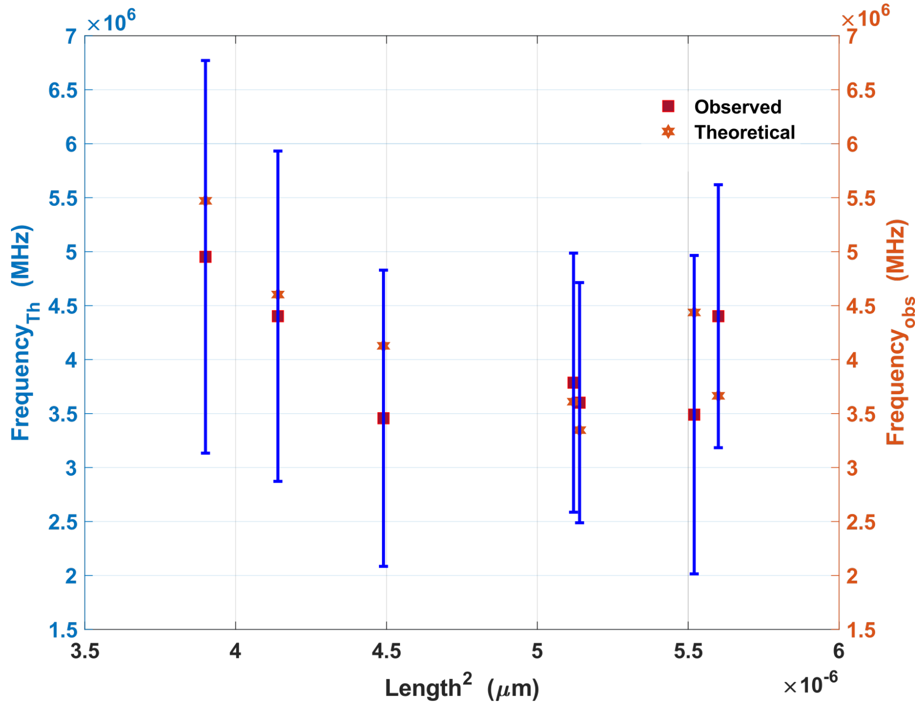

Figure 5.5: Estimated error between excitation frequencies and their theoretical values plotted as function of Length.

from their theoretical estimation. The variation in the excited frequency may arise from the transmission cord connected to the nanomanipulator. A delay in transmission frequency and vibration of NW was frequently observed which may occur due to indirect dynamical mechanical loading. In this case, the electric charge will take longer to accumulate at the surface of the nanomanipulator and to initiate capacitive-force driven dynamical mechanical loading. While in direct loading, the mechanical vibrations are induced by direct implementation of the eigenfrequency such as vibrations induced via lasers. At the nanoscale, the dimensions of an object play a deterministic role in the estimation of eigenfrequency. In Fig. 5.5 we have investigated the difference between excitation frequency and observed frequency via error estimation. The results presented in Fig. 5.5 are obtained by considering the deviation of NW's diameter and length i.e., 65% and 5% , from their measured values. The estimated frequency shows a strong sensitivity towards the length and diameter of the NW due to the nonlinear dependence. Thus, a wrong estimation of any of these parameters from SEM imaging will exceptionally impact the determination of the eigenfrequency .

We demonstrated systematic electromechanically induced vibrations in single pristine GaAs NWs, either by increasing or decreasing the amplitude of resonance and the dwell time. The crystalline structure and phases of dynamically loaded NWs were meant to be examined by using *ex-situ* Bragg Coherent X-rays Diffraction Imaging (BCDI) at beamline CRISTAL, SOLEIL in order to understand the impact of the deformation and mechanical behavior. Unfortunately, the *ex-situ* experiment that was planned for March 2020was canceled and shifted twice due to COVID-19 pandemic spread. Thus, at present,

no structural analysis of the vibrated NWs has been performed, at variance with the original plans.

6

Anelasticity In Semiconductor Nanowires

In the recent past, a time-dependent elastic relaxation upon mechanical deformation was identified in ZnO semiconductor nanowires. This anelastic behavior [142,143] is a process where the material after unloading exhibits a complete reversible but non-instantaneous recovery of its initial state. It was first conceived by Zener in 1948 and published in his monograph, "Elasticity and anelasticity of metals [144]". While the non-instantaneous recovery looks like plasticity at first sight, it implies a time-dependent response during the relaxation, in addition to an instantaneous elastic response. As will be shown in the following, anelastic relaxation is a kinetically controlled phenomenon which relates to the coupling between stress and strain by means of certain internal variables. Based on the driving mechanism of molecular relaxation, these internal variables can shift to an entirely new equilibrium state which occurs only via kinetic processes such as diffusion [145]. Multiple physical driving mechanisms contributing to anelastic relaxation have been identified, as discussed in the next section. Most of them are related to the reversible migration of point defects in the crystal structure. Within this manuscript, the anelastic effect is attributed to the diffusion of point defects under an inhomogeneous stress field and and its recovery.

In this chapter, the theoretical background of the strain gradient induced diffusion of point defects will be introduced, followed by a short review of the state-of-the-art studies of anelasticity in nanomaterials, and finally bending experiments on Be-doped GaAs nanowires.

6.1 Anelasticity in semiconductor nanowires

In the following, the state-of-the-art on anelasticity in NWs is briefly reviewed. As mentioned earlier, micro- and nanostructures exhibit enhanced mechanical properties as compared with their bulk counterpart[8,9], which may be attributed to the anelastic behavior.Sheng et al.[146] observed high strength in twinned CuO NWs in comparison to the bulk which is stimulated by the anelastic strain induced by blocking the motion of dislocations at twin boundaries. Although bulk materials display the anelastic behavior as well, it is much more significant in the nanostructures due to small dimensions and its influence on various parameters like temperature and diffusion which is more prominent. While anelasticity is rather well studied for bulk materials[147], alloys[148] and polymers[149], it is a comparatively new domain for NWs. The time dependent stress-strain response of a material can be described by the Zener model[144] i.e., each level of applied stress is associated with a unique equilibrium strain value. For ideal elastic behavior, this unique equilibrium strain is instantaneous and linear. While for anelastic behavior, the equilibrium rate is characterized by one or multiple internal variables (either a short-range or long-range order parameter) after the change of state. For example, Ikuma et al.[147] studied the high-temperature (1160 to 1450[°C]) deformation by stress relaxation and dead-load creep in dense polycrystalline (10 to 90[μm]) Al_20_3 and MgO doped with Fe. The results revealed discrepancies in both the magnitude of the strain rates and the dependence between the strain rate and stress that were attributed to the existence of anelastic effects originating from deformation caused by the elevated temperature. Anelastic strain was observed by David et al[149], for uniaxial and biaxial compression tests on glassy polymers and was attributed to the point defects migration and redistribution.

Depending upon the nanostructure, the anelasticity of NWs may be associated to different mechanisms. One study demonstrated the anelastic relation of the motion of atoms adjacent to twin boundaries in twinned CuO NWs[146]. Atoms near the edge of twin boundaries were dragged away from their original sites to facilitate the local lattice distortions under an external bending stress and during the unloading these atoms returned to their original site. Stress relaxation, in this case, is not spontaneous and causes anelastic deformation at low temperature. Furthermore, the motion of the dislocations may be blocked by the twin boundaries, preventing the NWs from fracture and facilitating anelasticity[150] but normally blocking the dislocations favors fracture.

Anelasticity was further reported for single-crystalline GaAs NWs where it was attributed to the existence of an amorphous oxide surface layer formed during sample preparation[22]. *In-situ* bending tests were conducted inside the TEM to study the anelasticity. Once the external load was released, the amorphous layer around the NW resisted the recovery of the crystal core and thus induced an increment in the recovery time. The thicker the surface amorphous layer, the longer the recovery time or anelasticity. Hence, this kind of anelasticity depends on the NW diameter.

In a recent paper, the anelastic behavior of amorphous Si NWs was studied as a function of their structure, depending on whether they were straight or curved in as-grown geometry. For the curved

NWs a non-instantaneous relaxation was observed when the NWs are bent along their original curvature. On the contrary, no initial anelasticity was found for straight nanowires. STEM-EELS analysis suggests that the underlying mechanism for this anelastic behavior is a bond-switching assisted redistribution of the nonuniform density (structure) in the curved NWs under the inhomogeneous stress field while the straight NWs deforms elastically. No bond switching occurs when the curved NW is bent against its curvature and does not display any anelasticity. However, an anelastic behavior can be introduced into originally straight NW by Focused Ion Beam (FIB) that modifies its morphology and causes a non-uniform structure distribution. Thus, anelasticity in amorphous Si NWs is a tunable property and can be manipulated by modifying the morphology, by controlling the loading direction or by FIB irradiation.

Anelasticity of NWs has recently attracted much attention and probably the most significant work was reported by Cheng et al.[151]. For single-crystalline ZnO NWs and p-doped Si NWs, the authors observed a large anelasticity that is, up to four orders larger than in bulk ZnO, with a relaxation time in the order of minutes. The oxide layer model[22] and the twin boundary motion mechanism[146] do not justify the large anelasticity of ZnO NWs. Thus, a theoretical model was developed considering a nonlinear relation between the anelastic strain and the initial strain. This model suggests that the anelasticity is based on the diffusion of point defects in the NW′s crystal lattice. During the bending, the stress gradient across the sample creates a gradient of the chemical potential which forces the point defects to migrate; oxygen vacancies from the tensile to the compressive end and zinc interstitials towards the opposite direction. Thus, the Gorsky effect, which arises from the motion of point defects in an inhomogeneous stress field[152,153], is the driving mechanism. The diffusion constants for vacancies and interstitials were found to be much greater than their respective bulk values. The results showed that the small diffusion distance (small NW diameter), large diffusivity values and stress gradient are the combined factors that contributes to the relaxation time of the order of minutes.

6.2 Anelasticity tests in FIB/SEM system

As discussed earlier Semiconductor Nanowires (NWs), which are regarded as potential candidates for future optoelectronics and sensor-based nano-electromechanical systems, were shown to exhibit superior properties compared to their bulk counterparts thanks to finite-size effects and possible quantum size effects caused by their large aspect ratio and quasi-one-dimensional nature. While numerous studies of uniaxial tension and compression tests exist in the literature, bending experiments are scarce although the flexure behaviour is of major importance for applications such as flexible electronics.

While performing the cantilever bending test on Be-doped GaAs NWs, time independent elastic deformation is expected as the elastic strain completely recovered after unloading. In some cases, it was observed that the NW does not completely bounce back to its initial state instantly, but it takes a finite time to recover from the strain completely. This time-dependent relaxation is analogous to the anelastic recovery. This was the compelling reason to investigate the anelasticity in semiconductor NWs. Initial

anelasticity tests were performed at the University of Siegen employing the dual beam FIB/SEM system where a nanomanipulator equipped with a tungsten probe was used. It offers the precise and instantaneous control of the displacement of the NW during bending with a fine step size of the order of nm. To release the NW , the nanomanipulator is retracted quickly within a few steps with the step size of the order of μm, to avoid any collisions and to record the essential early stages of relaxation. The tests were performed at room temperature at three Be-doped GaAs NWs, NW1, NW2 and NW3. The nominal doping concentration in NW1 was $1 \times 10^{19} [1/cm^3]$ while it amounts to $1 \times 10^{18} [1/cm^3]$ for NW2 and NW3. Different methods were adopted to estimate the curvature during the holding period and to deduce the curvature as a function of relaxation time after the external stress is removed from the NW. During the holding and keeping NW1 under a constant external stress, the curvature is deduce by fitting a circle at the base of the NW, i.e. the maximum initial bending strain position as presented in Fig. 6.1 - (a). The measured nominal diameter D of the circle is related to the curvature κ as

$$\kappa = \frac{1}{R} = \frac{2}{D} \tag{6.1}$$

Here R represents the radius of curvature. NW2 and NW3 are considered to be bent in semi-circular shape, and thus it is assumed that the measured curvature and the corresponding initial bending strain distribution are uniform across the length of the NW.
Curvature after the release of external stress is measured as a function of the relaxation time from the SEM images by using a Digital image correlation (DIC) algorithm. The functionality of the algorithm is comprehensively discussed in the next subsection. The time-dependent anelastic relaxation of the curvature is extracted by second degree polynomial on the entire length of the NW. Thus the curvature obtained (nonlinear coefficient of fit) is the average over NW. This agrees with our assumption made in mathematical modelling where the NW is subjected to pure bending and inducing a constant quadratic shape curvature.

Fig. 6.1 - (a) presents SEM images of NW1 being bent by means of the nanomanipulator. After a holding time of 20 min, the NW was released and the relaxation process was monitored (insets 1 to 3 in part (a)) in real time by taking SEM images. Fig. 6.1 - (b) shows the curvature of the Be-doped GaAs NW after release as a function of relaxation time measured by SEM. Structural parameters and other investigated experimental conditions of NW1, NW2 and NW3 are summarized in Table. 6.1. When the bending force is removed, a large portion of the bending strain is recovered instantaneously while a small part of the curvature remains, which slowly decreases over a period of a few minutes.

6.2.1 Anelastic strain calculations

The NW relaxation was recorded in real time by video graphs while simultaneously taking SEM images at a frame rate of 5 seconds/image. The set of Scanning Electron Microscopy images was analysed by using a Digital image correlation (DIC) algorithm [154] to extract the time resolved anelastic strain relaxation of

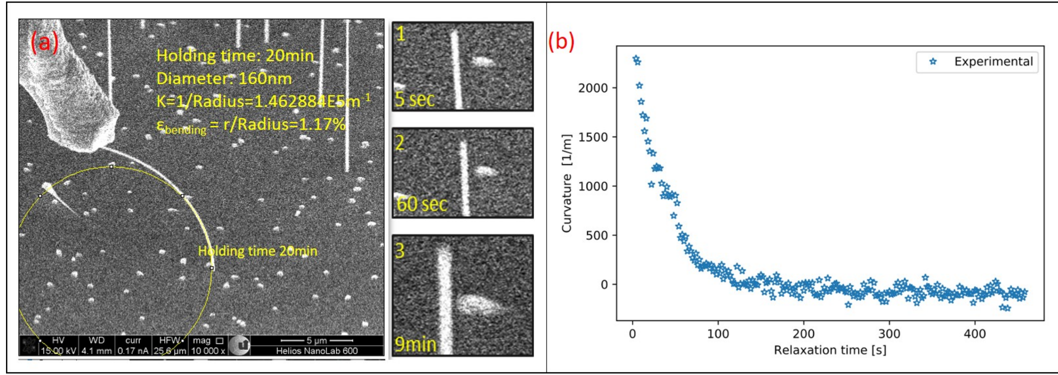

Figure 6.1: a. GaAs NW under loading for 20min. The insets show the relaxation after unloading after (1) 5 sec, (2) 60 sec and (3) 9min. **b.** Curvature of the GaAs NW after release as a function of relaxation time measured by SEM

	Length L (μm)	Diameter d (nm)	Nominal concentration c_n (1/cm^3)	Curvature κ (1/m)	Initial strain $= \frac{d\times\kappa}{2}$ (%)
NW1	20	138	1×10^{19}	1.462×10^5	1.17
NW2	21.4	240	1×10^{18}	2.395×10^5	2.87
NW3	22	139	1×10^{18}	2.336×10^5	1.61

Table 6.1: Summary of the samples used for anelastic relaxation experiment.

the NW by identifying the NW profile and deflection. Considering that a SEM image shows only a 2D projection, the following assumptions were applied for the 3D displacement $\vec{u}(h)$ of a point on the wire at height h:

1. NW is almost aligned with image axis (horizontal or vertical)

2. NW movements are only in the image plane

3. NW deflection remains small

the NW shape description could be simplified to $u_y(x)$ where x is the horizontal position on images and u_y is the NW position along y axis. The NW position is obtained by scanning the position of maximum intensity for each profile along y-axis of the image. Fig. 6.2 - (a-b) shows an image example and the corresponding profile for $x = 100$. The NW position at $x = 100$ is estimated as the position of maximum intensity.

Wrong estimations occur when another particle is located either in the vicinity of the NW or after the end of the NW as shown in Fig. 6.2 - (c). These outliers are removed from the estimated NW profile using a constant threshold filtering. However, to calculate the deviation from the actual NW profile, a sufficiently good estimation of the NW profile is needed. The algorithm uses iterative weighted fit where the weights are defined as the inverse distance to the previously obtained NW profile. After a few

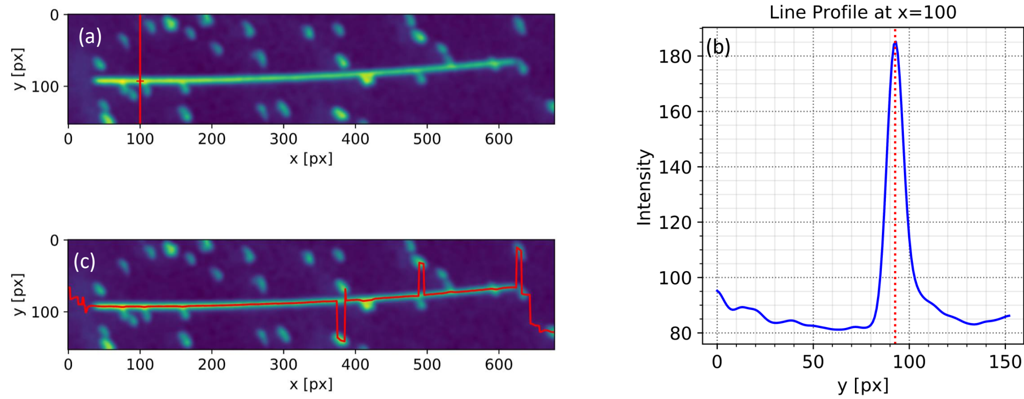

Figure 6.2: Deflection profile is extracted by scanning and recording the position of maximum intensity of each x-pixel along the y-axis. **a.** Line profile taken at $x = 100$. **b.** The corresponding intensity profile with maximum at $y = 93$. **c.** Misleading maximum intensity estimation influenced by the neighboring artifacts and particles for the deflection profile of the NW .

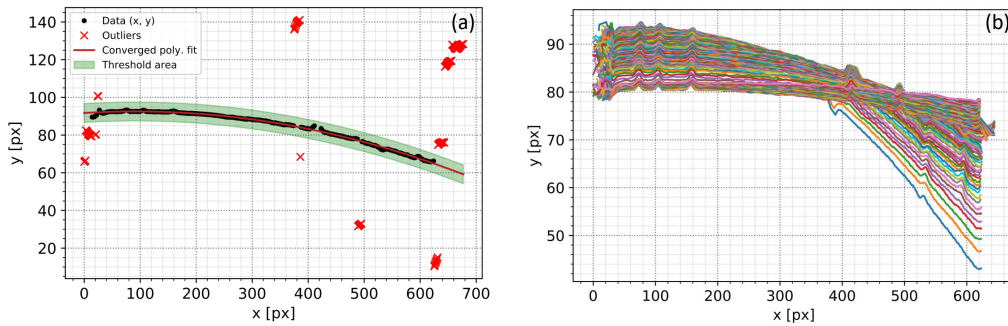

Figure 6.3: **a.** The deflection profile of the NW is obtained by removing the outliers and fitted with a second order polynomial around the maximum. **b.** Stacked deflection profiles extracted from the SEM images by using the DIC algorithm.

iterations the NW profile and weights converge to a solution as shown in Fig. 6.3 - (a). By means of the last fitted NW profile, the outlier points are removed applying a reasonable threshold.

To obtain the subpixel accuracy when searching for the maximum intensity position, a second order polynomial is fitted around the maximum. A second order polynomial has general form

$$f(x) = a + bx + cx^2 \tag{6.2}$$

Fig. 6.3 - (b) shows the stacked deflection profiles obtained from the SEM images with a visible drift in y direction. This drift originates from the SEM images and it does not require additional adjustments due to the fact that the nonlinear coefficient of the polynomial fit, i.e., the coefficient c in the quadratic cx^2 term corresponds to the curvature of the NW, see Fig. 6.4. By considering the entire deflection profile of the NW the homogeneous fitting leads to an average and constant curvature as a function of relaxation

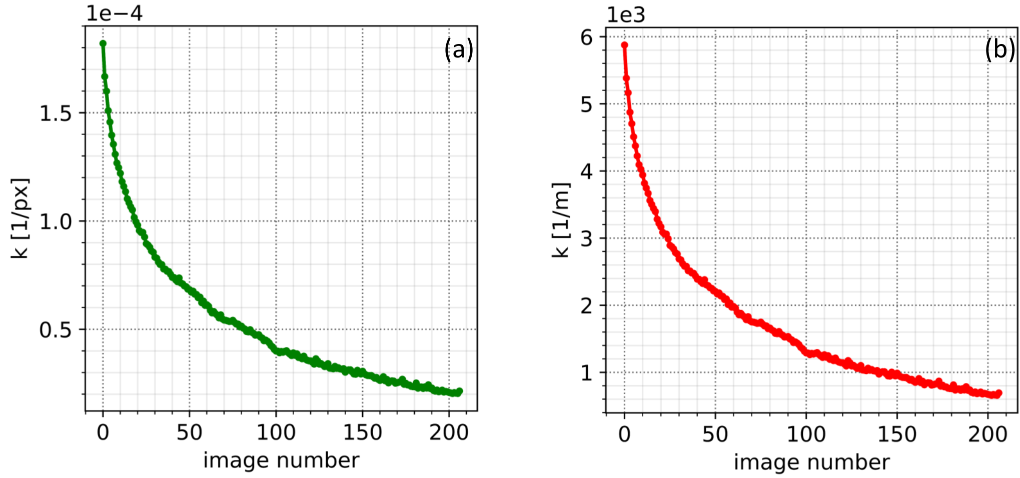

Figure 6.4: Curvature of the NW **a.** per pixel **b.** per meter during the relaxation, after holding and release.

time. The residual of the polynomial fit gives access to the information about how much the curvature varies along the NW. As depicted in Fig. 6.5, the residual of the fit does not change significantly along the length of the NW. The substantial fluctuations are caused by the adjacent noisy points and outliers, see Fig. 6.4 - (a), that is unavoidable and can not be removed by using the threshold. The units of the derived curvature are converted, from pixel to microns, by using appropriate scale to get the actual scale curvature of the NW. Once the NW is elastically relaxed after the holding and subsequent release, the anelastic relaxation is dominated by the anelastic strain which is estimated using the time resolved curvature of the NW. Time evolution is inferred from the SEM micrographs.

6.2.2 Anelasticity in Be doped GaAs nanowires bent in semi-circular form

In this section, the results from the heavily bent Be doped GaAs NWs are presented. Two NWs, NW2 and NW3, were bent in a semi-circular arc by using the same set-up as described above. The investigated NWs have a nominal Be doping concentration of the order of $1 \times 10^{18} [1/cm^3]$. Length and diameter of the NWs are listed in Table 6.1. Fig. 6.6 shows both NWs in pristine condition. Both NWs were bent by buckling and then by controlling the motion of the nanomanipulator to constraint the NWs until their free ends contact the Si substrate. The attachment of the free end to the substrate is also endorsed by a visible change in substrate color contrast at the point of contact as shown in Fig. 6.7. In our experiments, additional measures were adopted to keep the bending planar, i.e., the SEM image plane is parallel to the NW bending plane. However, the nanomanipulator navigates in the horizontal and vertical direction in an angular fashion. It may lead to an offset angle between SEM image plane and NW bending plane, see Fig. 6.7. Further steps were considered to correct the offset angle and to obtain SEM micrographs that allow for an error-free estimation of the curvature using DIC algorithms. In the postmortem analysis,

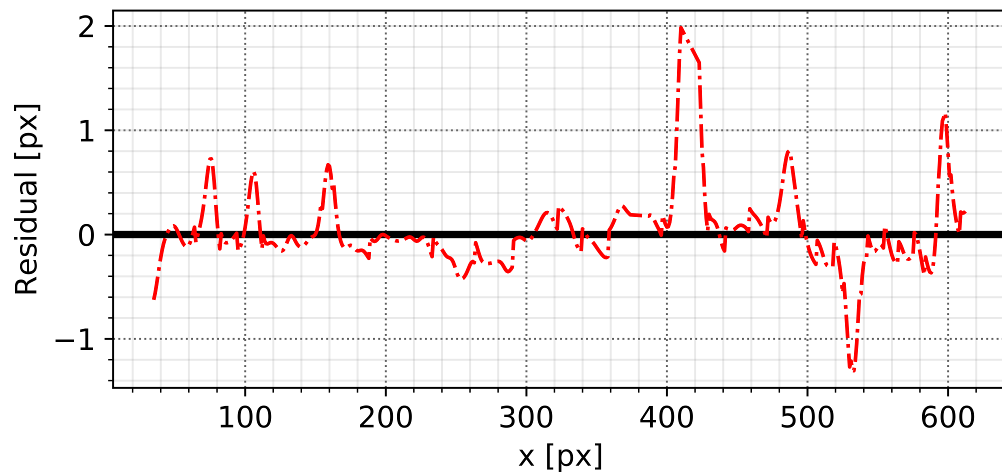

Figure 6.5: Residual of polynomial fit presented in Fig. 6.4 - **a.**

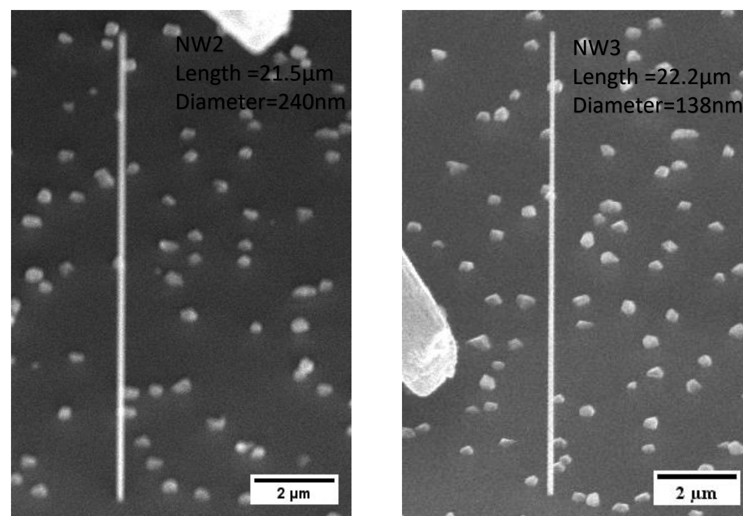

Figure 6.6: NW2 and NW3 before nanomanipulation i.e., pristine form. This geometry was taken as unstrained reference for the relaxation mechanism.

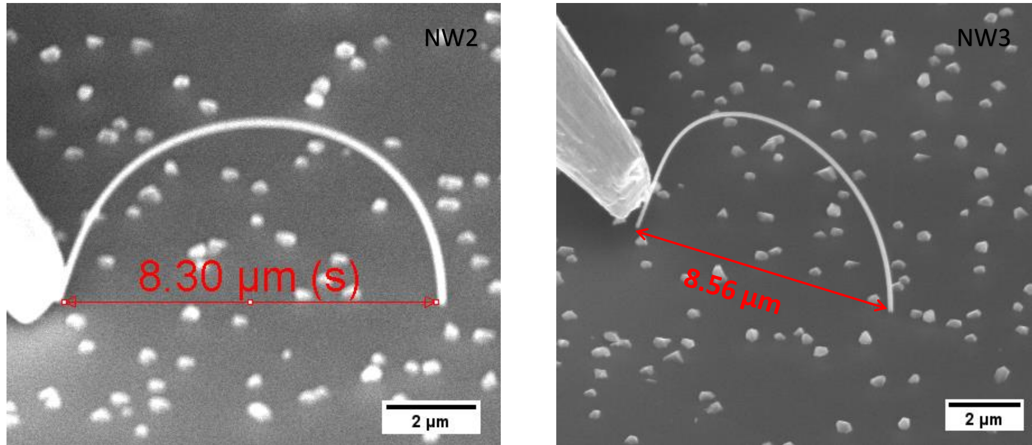

Figure 6.7: NW2 and NW3 bent and hold in semi-circle form for 17 minutes and 20 minutes respectively. NW3 has an offset angle between NW plane and image plane.

the distance between the position of the NW, **A**, and the contact point of the free end of the NW at the surface, **B**, was measured by translating the substrate perpendicular to the SEM column i.e.,0° tilt of sample stage. After translation, the offset angle was estimated to be 26.64°. To avoid time consuming and complicated mathematical transformation we skewed the SEM images at the offset angle and assume that the NW was bent in a semi-circular form. The skewed image in Fig. 6.8 fits to a perfect semi-circle with a radius equal to the half of the distance AB between points A and point B i.e., the radius of curvature of the bent NW. The holding time for NW2 and NW3 was 17 minutes and 20 minutes, while the relaxation lasted for 13 minutes and 17 minutes, respectively. The initial bending strain for NW2 is 1.61% and for NW3 is 2.87%. The initial bending strain is estimated by $\varepsilon_i = \kappa \times r$. Here r refer to the radius of the NW while κ is the initial bending curvature during bending and holding. It is assumed that the NW is bent in a perfect semi-circular shape and thus the inverse radius of the semi-circle results in a curvature κ. SEM images recorded after releasing the NWs are presented in Fig. 6.8 visualizing the relaxation process. After the initial elastic relaxation, both NWs show a first comparatively quick relaxation during the first 350 seconds, which slows down in the following as shown in Fig. 6.9. The relaxation is analysed in more detail in section 6.4 using FEM modelling.

6.3 Mathematical Modeling

One of the earliest contributions to the relaxation due to diffusion in a stress gradient was proposed and worked out in detail by Gorsky (1935). It concerns the long-range diffusion of impurities in an inhomogeneous stress field. Although the model was proposed already in 1935, its first experimental verification was carried out only in the late seventies of the last century by Schaumann et al.[152,153]. It was the first experiment proposing to use Gorsky relaxation as a tool to measure hydrogen diffusion in metals. Following this work, a number of studies were reported using this technique to measure hydrogen diffusion

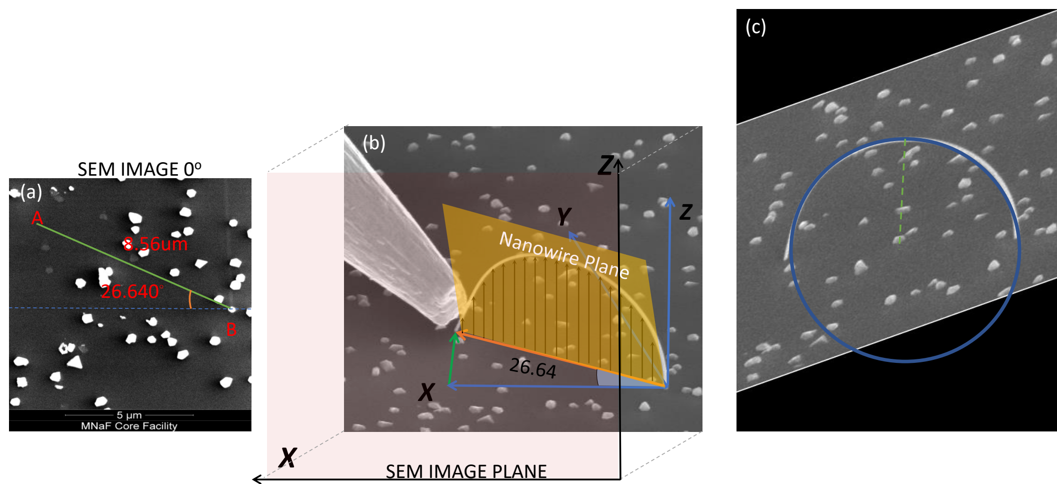

Figure 6.8: **a.** Offset angle and the diameter of semi circle arc, distance between point **A** and **B**, was estimated at $0°$ tilt of the sample stage. **b.** Bent NW imaged at $52°$ tilt. **c.** Skewed SEM image after the offset tilt correction fitted with a perfect circle.

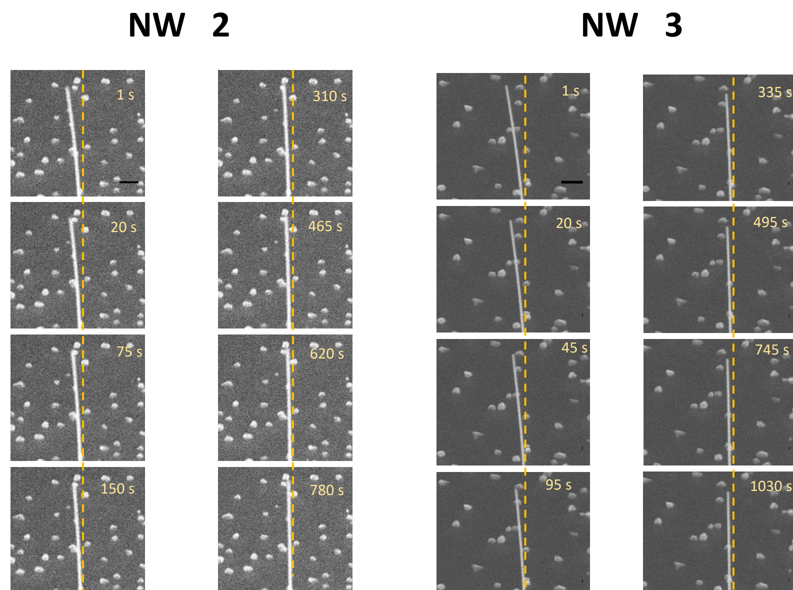

Figure 6.9: Relaxation of the NW2 and NW3 as a function of time. Scale bar represents 1μm. Relaxation time for NW2 and NW3 is 13 minutes and 17 minutes respectively.

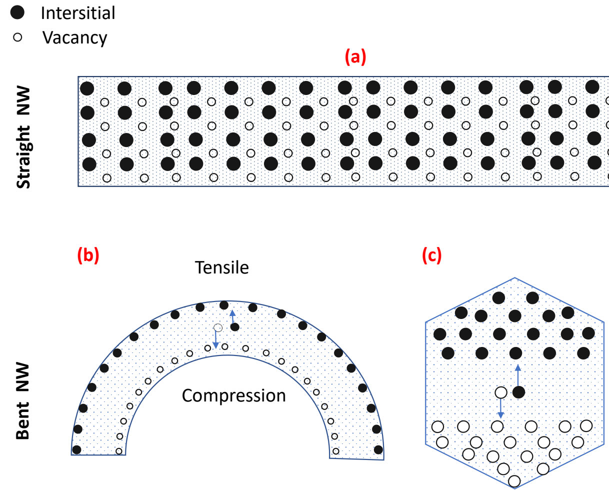

Figure 6.10: a. A straight NW with uniformly distributed point defects. **b.** In a Bent NW point defects migrates in stress gradient. Interstitial diffuse towards the tensile part and vacancies in opposite direction. c. Arrangement of vacancies in the hexagonal cross-section, during the bending.

in metals and alloys (even amorphous alloys).

Classical Gorsky relaxation is commonly measured as an elastic after effect. To realize the Gorsky effect in the simplest fashion, we assumed that the initial defect (vacancies and interstitials) distribution in the NW is uniform as shown in Fig. 6.10. When the NW is bent, the stress gradient within the NW cross-section generates a chemical potential gradient, along which point defects are diffusing, thus creating a composition profile across the NW, see Fig. 6.10. When the bending force is removed, the elastic strain recovers instantaneously. This elastic strain relaxation is followed by a much slower anelastic strain relaxation caused by the diffusion of the point defects to restore a homogeneous composition profile. The relaxation time τ is expected to be in the order of $\frac{a^2}{D}$, where a is the diameter of the NW and D is the diffusion coefficient.

To observe Gorsky relaxation and to get measurable strain, either small dimensions or large diffusion coefficients are required. On the other hand, point defects must be highly mobile like H in metals. H is a very fast diffuser, which make H diffusion very difficult to evidence during diffusional relaxation in a strain gradient, but it is perfectly suited for the Gorsky effect. Assuming that the anelastic strain relaxation of 20[min] found for the studied nanowires with a diameter of 240[nm] is caused by the Gorsky effect the diffusion coefficient has to be of the order of $10^{-18}[m^2/s]$.

Following the classical Gorsky effect, a mathematical model is introduced for the three-dimensional description of anelasticity in non-linear strain fields induced by the presence of point defects. A more detailed version is given in reference [151]. To begin with, the following constraints are considered:

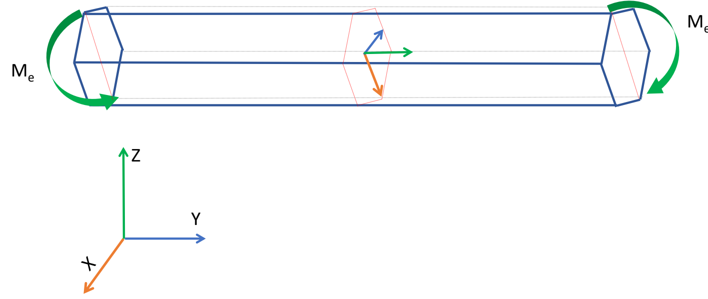

Figure 6.11: Graphical illustration of a NW under the bending load.

1. The NW has a uniform hexagonal cross-section, a specific length and diameter and it is subjected to a pure bending along the x-axis inducing a uniform curvature (quadratic shape).

2. Planar 2D defects diffusion is considered with the hexagonal cross-section. In planar geometry, the hydrostatic stress is $\sigma_h = \dfrac{\sigma_{zz}}{3}$ where σ_{zz} is the only non zero component of the stress tensor.

3. The diameter (2a) is much smaller than the length (l) (2a « l) and during bending, the planar cross-section remains planar i.e. the total strain change is linear. This does not hold during the initial bending and holding but it is valid during the anelastic relaxation.

$$\varepsilon_{zz} = \varepsilon_o + \kappa y \tag{6.3}$$

   Here, ε_o is the initial strain and κ is the curvature of the NW.

4. In the case of diffusing point defects such as vacancies, as it is the case for Be-doped GaAs NW, the total strain ε_{zz} is given by the sum of the strain caused by elastic loading ε^e_{zz} and the strain caused by the diffusing point defect ε^*_{zz}.

$$\varepsilon_{zz} = \varepsilon^e_{zz} + \varepsilon^*_{zz} \tag{6.4}$$

   ε^e_{zz} is related to the Young's modulus E by Hooke's law for elastic isotropic materials

$$\varepsilon^e_{zz} = \frac{\sigma^e_{zz}}{E} \tag{6.5}$$

   ε^*_{zz} is the strain caused by point defects

$$\varepsilon^*_{zz} = \frac{1}{3}\Omega c \tag{6.6}$$

where Ω is the partial molar volume of the point defects. It is an algebraic term and depending on the type of point defects it is assumed positive (interstitial) or negative (vacancies). c is the concentration of vacancies.

The applied stress and the concentration profile are coupled with the curvature κ across the NW cross-section and it can be further verified by using force and moment balance equations,

$$\begin{aligned} \iint_D \sigma_{zz} dxdy &= 0 \\ \iint_D \sigma_{zz} y dxdy &= M_e \end{aligned} \tag{6.7}$$

Eqs. 6.3-6.7 can be exploited to extract the relations for curvature κ and ε_o.

$$\begin{aligned} \varepsilon_o &= \frac{2}{3\sqrt{3}a^2} \iint_D \frac{1}{3} \Omega c dxdy \\ I &= \frac{5\sqrt{3}a^4}{16} \\ \kappa &= \kappa_e + \frac{1}{I} \iint_D \frac{1}{3} \Omega c dxdy \\ \kappa_e &= \frac{M_e}{EI} \end{aligned} \tag{6.8}$$

Here κ_e is the elastic curvature, I is the quadratic moment for a hexagonal cross-section and M_e is the applied bending moment.
Conventional continuity equation relates the flux and the defect concentration as

$$\frac{\partial c}{\partial t} = \bigtriangledown \cdot J \tag{6.9}$$

Here flux J is coupled with the chemical potential μ and any imbalanced homogeneity in μ will increase the concentration flux

$$J = M \bigtriangledown \cdot \mu \tag{6.10}$$

with M being the mobility of the vacancies.
After solving Eq.(6.9), the following equation for the time dependent evolution of the defect concentration is obtained

$$\frac{\partial c}{\partial t} = D \frac{\partial}{\partial x} \left[\frac{\partial c}{\partial x} + \frac{1}{3} \frac{E \Omega c}{RT} \frac{\Omega}{3} \frac{\partial c}{\partial x} \right] + D \frac{\partial}{\partial y} \left[\frac{\partial c}{\partial y} - \frac{1}{3} \frac{E \Omega c}{RT} \left[K - \frac{\Omega}{3} \frac{\partial c}{\partial x} \right] \right] \tag{6.11}$$

where $D = MRT$ is the diffusivity coefficient obtained from Einstein's relation.
Eq. 6.11 is a Partial Differential Equations (PDE) and given the initial boundary conditions, it yields the

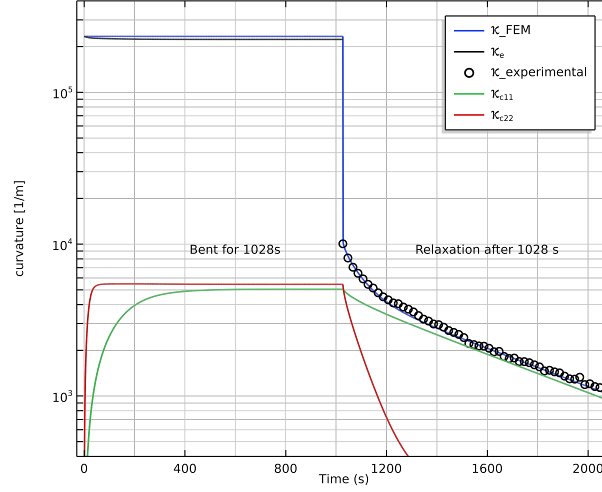

Figure 6.12: Time dependent curvature profile of NW2. The holding time was 17 minutes with 2.87% initial bending strain. Black line indicates the elastic curvature κ_e while blue and black circles are total curvature κ and calculated curvature $\kappa_{experimental}$, respectively. Green and red lines are the contribution of point defects towards the total curvature.

evolution of point defect concentration in the NW cross-section. It is assumed that the point defects, initially are uniformly distributed on the surface, i.e.

$$c = c_0 \text{ at } t = 0$$

The governing nonlinear partial differential equation is solved numerically in section6.4 dedicated to the simulation of the anelastic strain by the finite element method (FEM).

6.4 Finite element method modelling

As discussed in section 6.2, the vacancy diffusion under anelastic strain is solved numerically by employing Finite Element Method (FEM). The governing nonlinear Partial Differential Equations was simulated by using the General PDE Form module of *COMSOL Multiphsics*. Boundary Conditions (BC) and the constraints mentioned in section 6.3 are numerically implemented in this section.

To simulate the bending and relaxation processes under the same conditions as in the experiments, a NW with diameter of 138[nm] is considered. The NW was held at a fixed curvature with 1.17% initial bending strain for 20[min]. For t = 0[s] the total curvature is equal to the elastic curvature κ_e. With increasing holding time, the elastic curvature decreases due to the diffusion of point defects which increases the anelastic curvature keeping the total curvature κ constant as shown in Fig. 6.12. The Be atoms migrate towards the elongated and compressed edges of the NW during the holding period and it will bring the strain caused by these point defects to zero value i.e, Eq. 6.6. Initially, we perform the FEM simulations for anelastic strain by considering the diffusion of only one kind of point defects. In

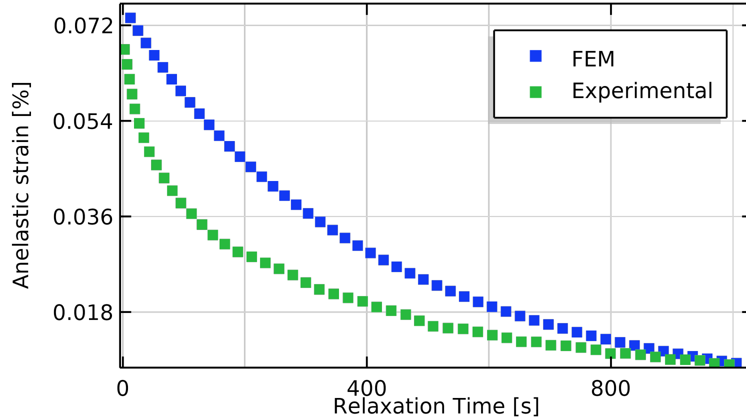

Figure 6.13: Time dependent anelastic strain as function of relaxation time compared with FEM result. Here FEM simulations are based on only one kind of point defects.

Fig. 6.13 we present the comparison of anelastic strain extracted from the experimental data and anelastic strain obtained from the FEM model where diffusion occurs due to the transfer and reversal of only one type of point defects. Despite the fact that both curves essentially have similar maximum anelastic strain and relaxation time, the qualitative agreement scares. FEM simulation shows a linear relaxation of anelastic strain as a function of time, which is a characteristic classical effect i.e., the diffusion occurs due to the migration of one type of point defects and the initial strain is small. While the experimental data shows a faster relaxation of anelastic strain at the beginning and then a slower and linear relaxation of anelastic strain afterwards. This qualitative agreement can be achieved by increasing the types of diffusing species, i.e., fast and slow moving point defects under the stress gradient. From this point forward, our FEM simulations are based on two types of point defects.

In our simulations, the nominal Be doping concentration of the NWs is considered as the initial concentration of the point defects. As mentioned in Chapter 2, Be dopant atoms are incorporated in GaAs as acceptors on Ga lattice sites and, in the case of high doping levels, an indication of Be at interstitial sites is also found. We thus consider two kinds of point defects here. Additionally, missing information regarding the exact doping gradient in Be doped GaAs NWs, the initial nominal doping concentration is varied for the optimization of anelastic strain. Initial concentration of two types of point defects for the visual agreement after the optimization is listed in Table 6.2. Initial concentration and the respective partial molar volume contribute to the quantitative anelastic strain profile of the NW during the relaxation. On contrary, qualitative agreement is achieved by tuning of diffusion constants.

The drop of point defect strain is rather quick and qualitatively it becomes zero as soon as the contribution of point defects to their respective curvatures, depicted by the red and green lines in Fig. 6.12, reaches its maximum value. Once the NW is released, the elastic curvature κ_e instantaneously drops to zero, which indicates that the applied moment is zero and the remaining curvature is of purely anelastic nature which varies as a function of time. In the absence of elastic strain, the leftover strain is attributed

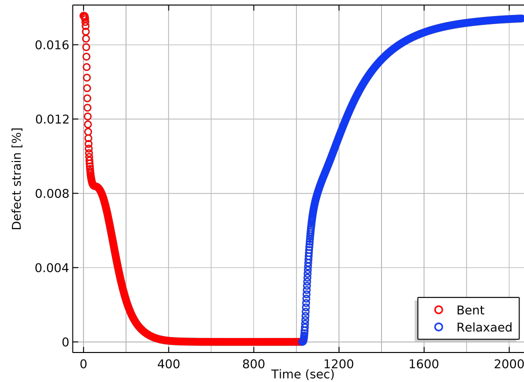

Figure 6.14: Strain profile originating from the migration of point defects a as function of time during the loading unloading of the NW2

to the anelastic strain or strain contribution from the anelastic curvature, i.e., the nonhomogeneous distribution of point defects induces a strain gradient that controls the curvature relaxation. During relaxation, when the point defects diffuse back to reestablish a homogeneous composition, the defect strain can also increase to take back its initial value, which is the strain caused by the initial concentration of the point defects.

Fig. 6.15 shows the concentration profiles in the cross section of the NW during the bending and relaxation process of NW1. The initial concentration of the point defects is considered homogeneous across NW's cross section, as shown in Fig. 6.15 - (a) . In Fig. 6.15 - (b-c) the nanowire is bent up to the initial strain and held there for 1200. Fig.6.15 - (d) . The NW is released at $t = 1200$[s]. When the bending force is removed, point defects diffuse back to restore a homogeneous composition profile as shown in Fig. 6.15 - (e) for t = 1600[s] (i.e., 400[s] after releasing the NW). This process controls the time-dependence of the NW curvature, which slowly returns to its original straight shape. In Fig. 6.15 - (f) the concentration profile in the cross section is presented during the bending, release, and relaxation. During the first $t = 400$[s] many point defects diffused and accumulate on the upper edge of the NW which is under compressive strain. After releasing the nanowire, the point defects diffuse back to the homogeneous phase, in the order of a few minutes.

Before going to further details of Finite Element Method simulations, we briefly discuss the impact of various parameters on the anelastic strain as function of relaxation time. Fig. 6.16 shows the simulated anelastic strain relaxation after the release of the NW. The holding period was 900[s] for all the cases except subgraph Fig. 6.16 (d) where the relaxation strain is compared for different holding times. A black dotted line is plotted as the reference curve of anelastic strain relaxation which is identical in every subgraph. All the parameters are varied ($\pm 20\%$) from the reference curve except (d) where the holding time was varied ($\pm 50\%$). Besides the varying parameter all other parameters were kept constant and depicted by the reference curve. The overall variation range we used for our parameters is relatively small, but the impact on subsequent anelastic strain is significant. Our simulation shows that the anelastic

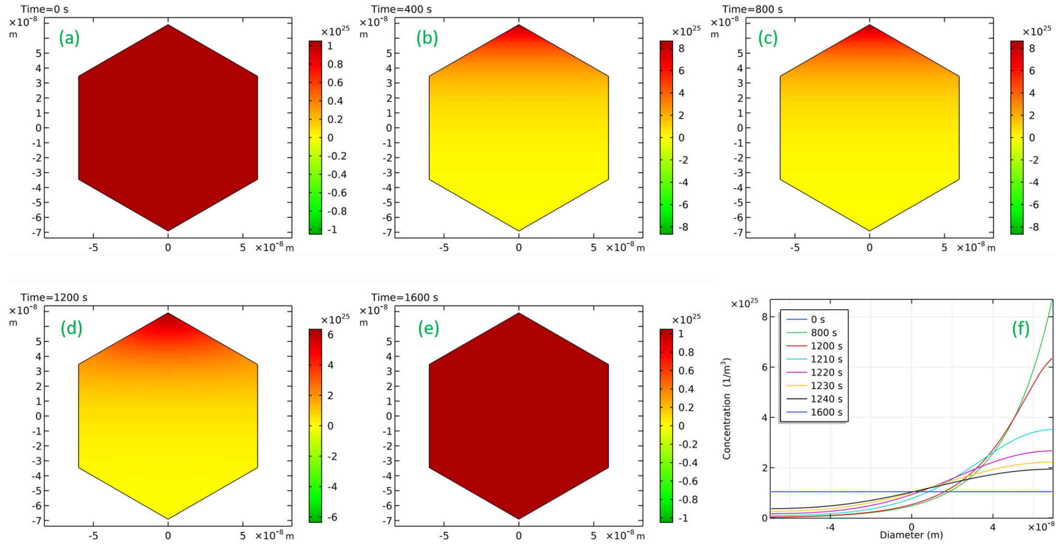

Figure 6.15: **a.** Uniformly distributed vacancies across the cross-section. **b.-c.** During the loading process, vacancies are drifted towards the higher compression in the NW. **d.** The NW is released by removing the initial bending strain.**e.** Redistribution of vacancies to the original composition profile, after relaxation. **f.** Vertical line profiles measured at the center of the cross section as function of time.

strain is highly sensitive to the diameter of the NW. NWs with smaller diameter exhibit higher anelastic strain values, while the diameter of the NW is inversely related to anelastic strain which is also consistent with physical suggestion that all mechanical effects are "smaller but stronger" at nanoscale. The average relaxation time varies as squared function diameter of the NW which is a direct indicative of a relaxation mechanism driven by the the Gorsky effect i.e. $\tau \propto d^2/D$. Initial bending strain, $\varepsilon_i = \kappa \times d$ is estimated as function of the diameter while keeping the κ constant. It shows a direct correlation to the anelastic strain and it is varied as inverse function of the diameter . On the other hand, initial concentration of point defects, c, and their corresponding partial molar volume ,Ω, varies linearly with the anelastic strain which is reasonable, given the fact that both are related to the defect strain, $\varepsilon_{defects} = \frac{1}{3}c \times \Omega$. FEM model predicts that the NW shows higher anelasitc strain if it is kept hold under the initial strain for longer periods while keeping the other parameters constant. Extended holding period will initiate further diffusion of point defects and consequently, once the stress is removed, these point defects require additional time to diffuse back to a homogeneous distribution. As mentioned earlier that the qualitative agreement with experimental data is not possible as long as only one type of point defects is considered. Therefore it is necessary to add two types of point defects minimum. It is evident from **(f)** that the diffusion coefficient introduces the nonlinear behavior of the anelastic strain while the remaining parameters have a linear relation with the anelastic curve. In **(f)**, the nonlinear behavior is attributed to the two kinds of diffusing species, i.e. slow and fast diffusing point defects. Thus, the visual agreement of FEM model to the experimental results is achieved by tuning the initial concentration and diffusion coefficients. Radius of the NW, initial bending strain and holding time are considered and modeled as in the experiment. By adjusting the initial concentration of point defects quantitative agreement to the experimental anelastic

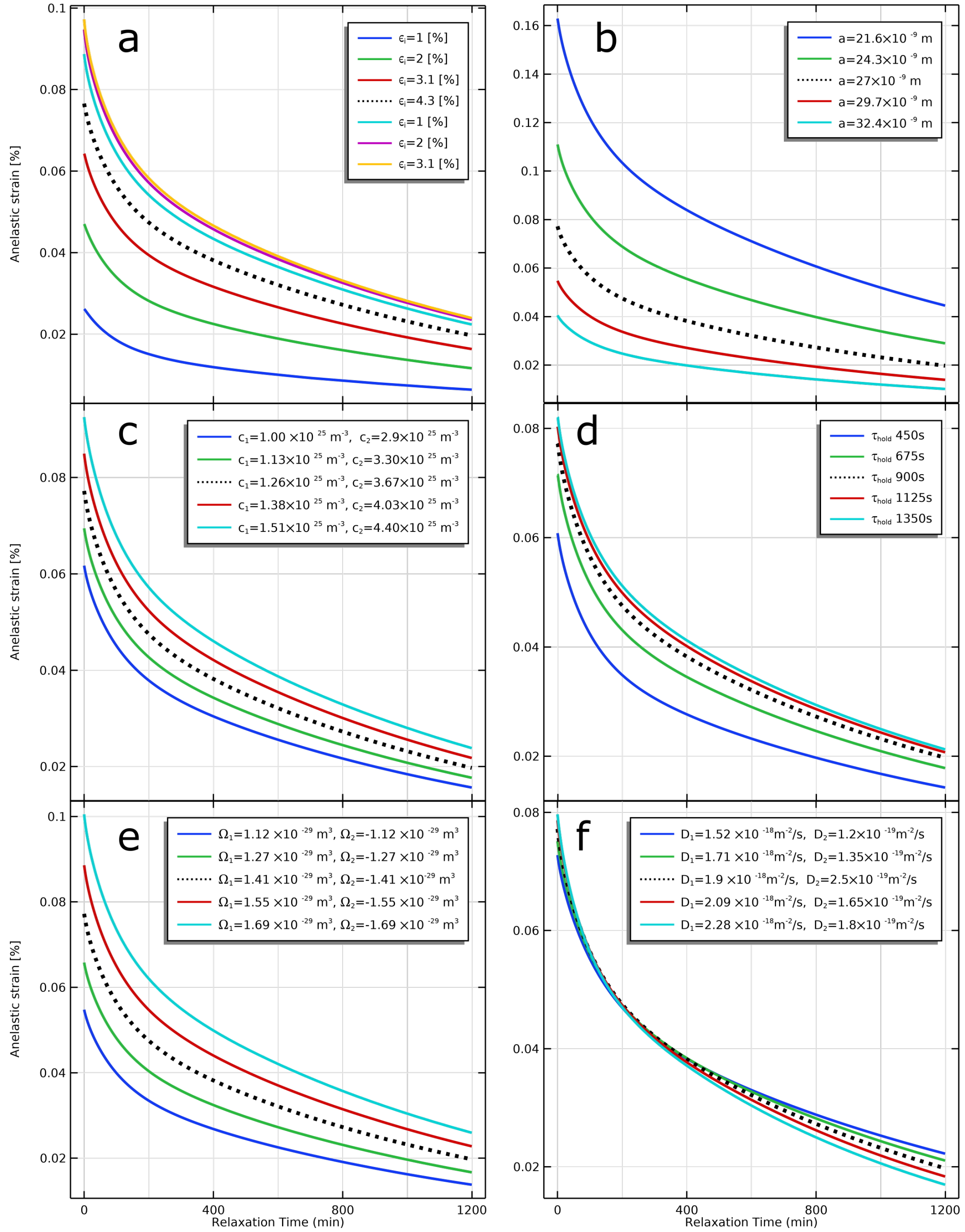

Figure 6.16: a. Anelastic strain as a function of recovery time for different initial bending strain **b.** radius **c.** initial concentration **d.** holding time, **e.** partial molar volume and **f.** diffusion coefficients.The holding time was 900 s in every case study except **d** where the holding time was varied ($\pm 50\%$).

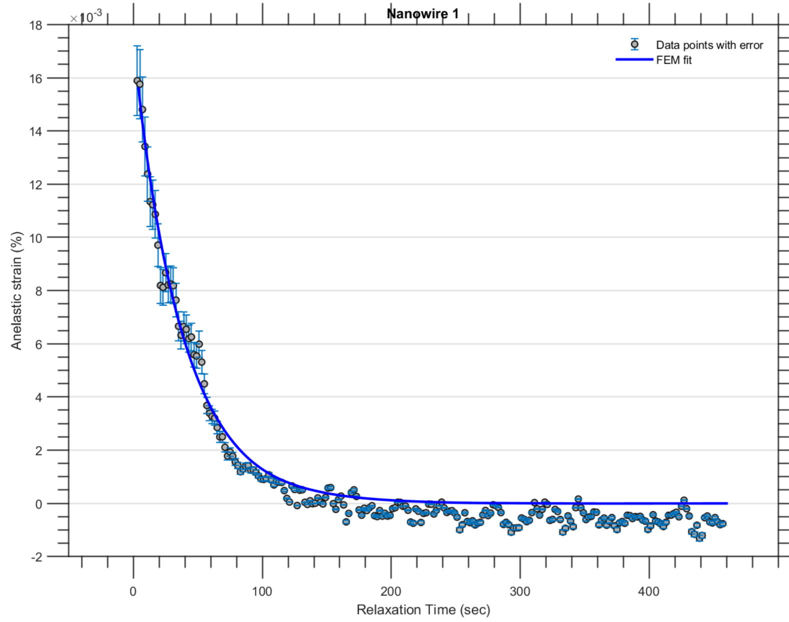

Figure 6.17: After releasing the initial bending strain, the time dependent curvature of the NW compared with FEM result.

strain was achieved, while qualitative agreement was met by the fine-tuning of diffusion coefficients.

6.5 Results and discussion

In this section, the experimental results for the three NWs, NW1, NW2, and NW3 presented in section 6.2 are compared/modeled with the FEM model. In Fig. 6.17, we compared the experimental results with the FEM model for curvature as a function of relaxation time. By varying the diffusion coefficients of the point defects, the visual agreement between FEM model and the experimental data was achieved. The best fit is obtained when the diffusivity of both kinds of point defects is considered $30 \times 10^{-14} [cm^2/s]$ with an initial concentration of $1 \times 10^{19} [1/cm^3]$ which is the nominal doping concentration of Be atoms. Results from NW2 and NW3 are depicted in Fig. 6.18. These NWs were bent in semi-circle shape. Fitting to the anelastic strain shows a good agreement with the FEM model for both NWs as shown in Fig. 6.18. The correlation of anelastic strain of both NWs with different parameters are imaged in Fig. 6.18. It can be concluded that the recovery of the anelastic strain depends on the holding time, i.e., recovery will be faster if the holding time is shorter since the point defects have less time to diffuse in the strain gradient to generate an inhomogeneous concentration profile. The maximum anelastic strain in the NW is a function of the initial bending strain. Higher initial bending strain leads to higher maximum anelastic strain. These findings are in agreement with predictions of the mathematical model for the Gorsky effect. Our results on Be doped GaAs nanowires, where the nominal doping concentration is considered as the initial defect concentration, agree with the findings reported by Cheng et al.[151] on ZnO nanowires. From the fitting results, it is evident that the point defects, during the bending tend

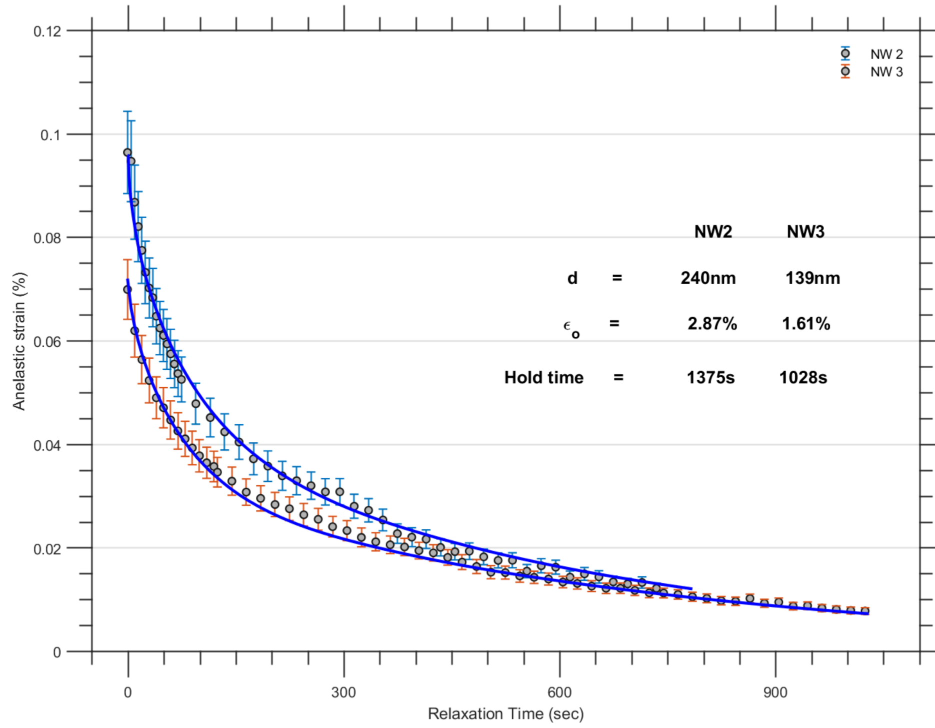

Figure 6.18: Time dependent anelastic strain recovery of Be doped GaAs NWs.

to diffuse towards the compressed and tensile sections of the NW due to the stress gradients that induce a chemical potential gradient. Once released, the point defects diffuse back to restore a homogeneous composition profile. The diffusion coefficient and other parameters used to fit the experimental results by FEM are listed in Table 6.1. The coupling between the stress gradient and Be atoms is assigned to the Gorsky effect, a slow process that controls the time-dependence of the NW curvature. The fact that the anelastic strain response is related to the doping concentration of the GaAs NWs provides additional prospects to exploit the NWs for the strain scalability and strain engineering.

In Fig. 6.19 - (a) the experimental anelastic damping as a function of relaxation time is plotted on

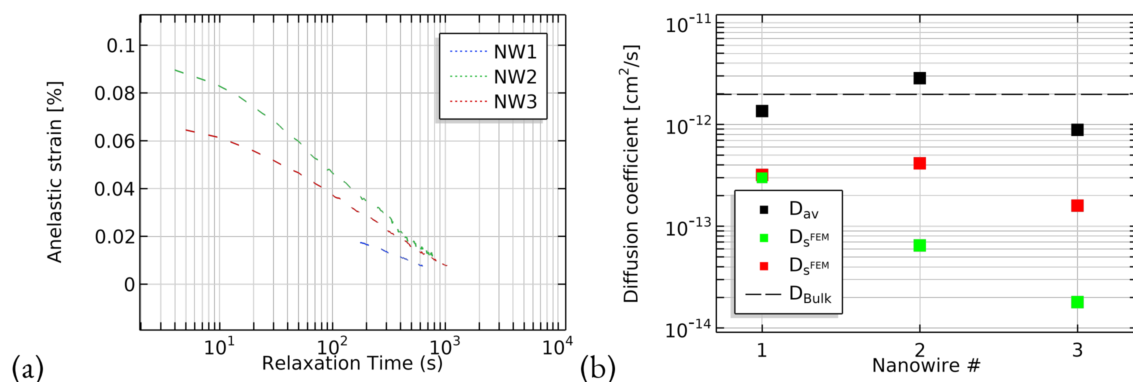

Figure 6.19: a. Anelastic strain relaxation plotted on semi-log scale to extract an average time for the complete relaxation by the extrapolation of the curve. **b.** The average diffusion coefficients are compared with the FEM simulation.

semi-log scale. An estimation of completely relaxed NW, i.e., time at zero anelastic strain, is possible to obtain from the extrapolation of the anelastic curves. The estimated relaxation time is exploited to approximate the average diffusion coefficient from the Gorsky model, see Fig. 6.19 - (b). Black dashed line represents the diffusion coefficient of Be in bulk GaAs. The average diffusion coefficients, represented by the black rectangles, have the same order of magnitude as for the diffusion of Be in bulk GaAs. On the other hand, the diffusion coefficients obtained from the theoretical FEM model agrees, both qualitatively and quantitatively, to anelastic strain relaxation via the diffusion of two types of species. NW1 has smaller initial bending strain in comparison to NW2 and NW3, thus the diffusion coefficients for NW1 are practically similar. Once the external stress is released on NW1, the point defects induce anelastic relaxation by diffusing back completely during the first 100[s]. NW2 and NW3 display more prominent anelastic relaxation where the relaxation is initially dominated by the by the fast diffusing point defects and later by slow moving defects. The diffusion coefficient extracted from the FEM model are $10 - 10^2$ orders faster then the diffusion coefficients of Be in bulk GaAs. The average diffusion coefficients estimated from the measured data and FEM model varies from each other, but both identify the long-range diffusion as driving mechanism for the anelastic relaxation. Thus, the observed anelasticity in Be doped GaAs is attributed to the nonlinear Gorsky relaxation that involves the diffusion of two types of point defect under an inhomogeneous stress field.

It must be noted that the diffusion coefficient of Be in GaAs is extremely small, in order of $10^{-42}[cm^2/s]$, at room temperature. Our estimated diffusion coefficients, as shown in Fig. 6.19 - (b), are 10^{-28} orders of magnitude greater than their room temperature value and in the close to the diffusion coefficient at the growth temperature. Cheng et al. [151] also encounter with a similar massive difference between the diffusion coefficient extracted from fitting the anelastic relaxation and the one extrapolated from high temperature bulk values. One possible explanation they presented for such an unorthodox behavior is the presence of a significant fraction of atoms, with different atomic bonding that in the bulk, near the free surface of the nanowire. It may introduce surface-mediated bulk diffusion. Second, the reduced activation energy under ultrahigh stress (on the order of GPa) leads to higher diffusivity. It is worth noting that our present understanding of the diffusivity of native point defects at room-temperature in GaAs nanowires and Be-doped GaAs is very limited. Furthermore, it is crucial to identify the source of such an augmented accelerated diffusion coefficient. This can be accomplished via electric or optical measurement of doping gradient in bent NWs as well as in NWs under ultrahigh stress by employing Raman spectroscopy or photoluminescence analysis.

	Diameter (nm)	D_1 $\times 10^{-14}$ (cm^2/s)	c_1 $\times 10^{19}$ $1/cm^3$	Ω_1 $\times 10^{-24}$ (cm^3)	D_2 $\times 10^{-14}$ (cm^2/s)	c_2 $\times 10^{19}$ $1/cm^3$	Ω_2 $\times 10^{-24}$ (cm^3)
NW1	138	30	15	4.05	32	15	4.05
NW2	240	6.5	34	4.05	41.6	34	4.05
NW3	139	1.8	45	4.05	16	45	4.05

Table 6.2: Summary of the parameters used in fitting model.

7

Three point bending test on Be doped GaAs nanowires

In this chapter, we discuss the mechanical properties of Be doped GaAs NWs by employing Scanning Force Microscope for in situ Nanofocused X-ray diffraction (SFINX) and XRD using focused synchrotron radiation. The nanomechanical testing on NWs was carried out in three-point bending configuration at the microfocus end-station of beamline P23 at the 3rd generation synchrotron radiation source PETRA III. In this chapter, the objectives are firstly introduced, followed by the description of the sample preparation and the experimental results obtained by *in-situ* three-point bending tests and post-mortem SEM imaging.

7.1 Introduction and objective

As stated earlier, the characterization and controlling of the mechanical properties of semiconductor NWs is important for their implementation in future devices and the mechanical properties are strongly influenced by the structural parameters such as phase and lattice strain. As mentioned in Chapter 6 the bending of NW generates both compression and tension at the opposite sides of the cross-section. In principle, cantilever bending tests on free-standing NWs with SFINX are possible but may lead to various uncertainties such as misalignment, non-planar bending of the NW and contact slip and slide between AFM tip and the NW. Hence we aim on studying the mechanical properties of individual Be doped

GaAs NWs and the influence of size effects by *in-situ* three-point bending tests in combination with nXRD.Contrary to lateral bending test, three point bending test require additional sample preparation which is provided in the next section.

In-situ three-point bending tests were designed to study the elastic and plastic response of the NWs. In the past, various uniaxial mechanical tests have shown twinning-mediated plastic deformation and deformation via dislocation slip where the nucleated dislocation glides quickly through the nanostructure to the surface of the NW. Contrary to uniaxial mechanical study, storage of dislocations has been reported via bending tests. Thus, three-point bending tests on Be-doped GaAs NWs were designed to test whether NWs may show plasticity or whether they fail by fracture. Finally, the nonlinear torsion relaxation, anelastic relaxation as a function of time, will be determined by loading the NWs with SFINX tip and holding them for a predefined period of time (1-5[min]). After unloading, the relaxation process will be monitored by iterative 2D X-ray diffraction mapping, providing access to the NW deformation and its relaxation as a function of time (with a time resolution of a few minutes). Crystal structure of the selected NWs will be compared before and after the mechanical loading by recording the RSM.

7.2 Sample preparation: Be-doped GaAs Nanowires

All experiments reported in this chapter were exclusively carried out on Be-doped GaAs NWs, details provided somewhere in Chapter 2. Typical diameter of the NWs is ranging from 150 to 250[nm] and the length ranges from 10 to 24[µm]. Three samples with different doping concentrations, with a nominal Be doping between $10^{18} - 10^{20}[cm^{-3}]$., are grown by Molecular Beam Epitaxy (MBE) on a Si (111) substrate. For preparing nanowires for three-point bending tests, these NWs are firstly being detached from the growth substrate by ultrasonication in a solvent and then dispersed on a Si substrate patterned with 10[µm] wide and 1.5[µm] deep micro-trenches by drop-casting. The sample was cleaved and then immersed in dilute CH_2Cl_2 dichloromethane solution. Later, the sample was carefully placed and exposed to an ultrasonic bath for a few seconds. It helps the embedded NWs to detached from the substrate. Few drops of this solution were then droped on the paterned Si susbtrate. Some of the NWs cross the micro-trenches, thus forming self-suspended nanobridges facilitating three-point bending tests, as illustrated in Fig. 7.1 - (a) . After sample preparation, the NWs in their pristine form were imaged by SEM. To avoid any movement and slipping of the NWs during mechanical bending or to stick to the AFM tip during AFM imaging, the nanowires were glued on the Si substrate by depositing platinum or carbon from the residual gas present in the FIB/SEM system as shown in Fig. 7.1 - (c). Fortunately, the $2\bar{2}0$ side facet of GaAsNW lies perfectly parallel to the surface of the Silicon substrate, see Fig. 7.1 - (b,d).

7.3 Lateral three-point bending test by symmetric X-ray diffraction experiment

The nXRD experiments were performed at beamline P23 of PETRA III (DESY, Hamburg) synchrotron station, with a photon energy of 18[keV] (λ = 0.6797[Å]). The incident X-ray beam was focused down

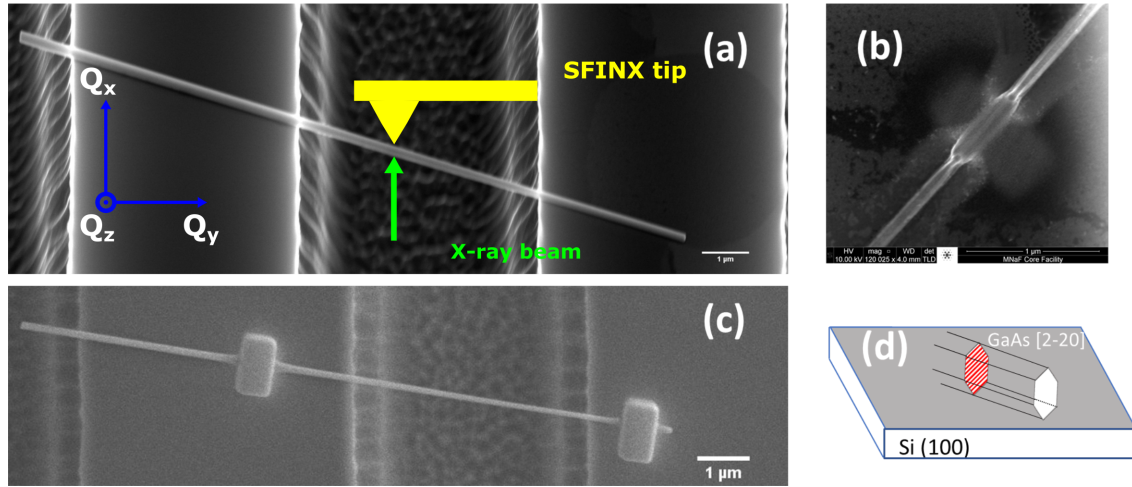

Figure 7.1: a. Scanning electron micrograph of Be-doped GaAs NW laying across the Si micro trenches after dispersion of mixture by drop casting. Green arrow represents the direction of beam. The displacement of SFINX tip was along Q_x during the bending of the NW. **c.** Self suspended NWs are glued at their two supports by depositing platinum in the FIB/SEM system. **b.** Scanning Electron Microscopy image of the $2\bar{2}0$ side facets of GaAsNW sitting parallel to the surface of Silicon substrate. **d.** Illustrates the affixing of the $2\bar{2}0$ side facets to the surface of substrate schematically.

to a size of 20[µm] using Be compound refractive lenses. The aim of this experiment was to study the relaxation process of three-point bent nanowires by recording 3D-RSMs before and after mechanical loading. The incident x-ray beam was localized on the sample and in the region of interest by setting the angle of incidence to the symmetric GaAs $(2\bar{2}0)$ Bragg reflection and the diffracted signal was recorded by a two-dimensional LAMBDA detector with a pixel size of 55×55 $[\mu m^2]$. The detector was mounted 1122[mm] downstream from the sample position. The nanowires were firstly located by optical microscopy. They were then localized by scanning X-ray diffraction mapping at the GaAs $[2\bar{2}0]$ Bragg reflection. The prepared NWs were far from each other avoiding any contributions from neighbouring nanowires despite the comparatively large beam size of 20[µm] in horizontal and vertical directions. The beam size of such an order was significant to record the entire NW in the reciprocal space but it also diminished the initial plan of probing the NW's curvature at point of loading and subsequent bending gradients by using a sub-micron focused x-ray beam.

The experimental geometry of a NW crossing Si micro-trenches is illustrated in Fig 7.1 (a). The 3D RSM of the $(2\bar{2}0)$ Bragg reflection recorded in reciprocal space is defined by three reciprocal space vectors Q_x, Q_y and Q_z where Q_x is along the direction of the X-ray beam and is along to the micro-trenches probing GaAs $[2\bar{2}0]$ planes whereas Q_y and Q_z are the vectors perpendicular to Q_x and are defined along [111] and $(2\bar{2}0)$, respectively. Instead of contacting the top side facet of the laying NW via lowering the SFINX tip and bending the $[2\bar{2}0]$ planes downward we opted for the lateral bending of the NW due to unexpected sample behavior. Although the SFINX tip was navigating without any hindrance and obstruction, for unknown reasons, it jammed into the surface as soon as it contacted the Si substrate, e.g., during AFM topography. To avoid undesirable damage or contamination of the NW during the

SFINX tip to the NW alignment process we chose to position the SFINX tip next to the NW rather than on top of it as shown in Fig. 7.1 - (a). After that, the SFINX tip was systematically lowered into the desired Si trench and translated towards the NW with a speed of $2 - 50[nm/s]$. A contact between SFINX tip and NW creates a change in the shape of Bragg peak. After the successful alignment, the SFINX tip was retracted by 10[μm]. It provides safety to avoid crashing until the actual lateral three point bending test. Despite being able to perform the lateral three-point bending test on the NW, the movement of SFINX tip along Q_x direction restrict the access of the in-plane bending profile of the NW. The Bragg reflection was localized at $Q_z = 31.4[nm^{-1}]$ as shown in Fig. 7.4 - (c). In this symmetric Bragg geometry the bending of the NW around the trench axis, i.e., with the SFINX tip movement along z direction provokes a lateral movement of the Bragg peak on the detector. On the other hand, the lateral movement of the tip makes the NW bend around z axis. The probed $[2\bar{2}0]$ planes have the normal around the bending axis, which cannot be detected. In this later configuration, the lateral movement of the Bragg peak on the detector corresponds to the torsion in the NW.

As mentioned earlier, the beam was focused by a series of CRL and thus scanning the energy of the incident beam [3] by using KB mirrors can not be employed here given the fact that the focal distance changes when changing the energy. Therefore we had to use monochromatic beam. We prefer to follow a single cut of the Bragg (detector plane) peak during the loading and unloading of the NW. It eliminates the risk of external factors such as vibrations induced by diffractometer during the rocking curve scan by staying at the same spot on the rocking curve. The relaxation after unloading was recorded via time scan. Prior to the lateral three-point bending tests 3D RSM were recorded for each NW. After loading and unloading 3D RSMs were recorded to have insight whether the NW was deformed elastically or plastically.

We performed lateral three-point bending tests on three NWs, NW1, NW2 and NW3. we used Be-doped GaAs (111)-oriented NWs, with a nominal Be doping of order $10^{19}[cm^{-3}]$, nominal diameter of around 150 - 250[nm] and height of about 20 - 24[μm] grown on silicon(111) substrate by self-catalyzed MBE [53] by Dr. Jesus Herranz from PDI. The results from these NWs are presented in the next section.

7.4 Results and postmortem of nanowires in FIB/SEM

7.4.1 NW1: Fracture and plastic deformation

The SEM image of NW1 used for *in-situ* lateral three-point bending test is presented in Fig. 7.2 - (a). The NW is sitting on two Si micro-trenches. On the right trench, it is facilitating self-suspended bridge for three-point bending test after the deposition of platinum glue. While on the left micro trench it allowed the possibility of NW cantilever based testing. The cantilever end of the NW was fractured during the SFINX tip alignment with respect to the free end of NW1. Before performing the lateral three-point bending test 3D RSMs were recorded by rocking the $[2\bar{2}0]$ planes. Fig. 7.3 shows a three-dimensional isointensity surface graph of the recorded RSM just before the nano-mechanical test. The

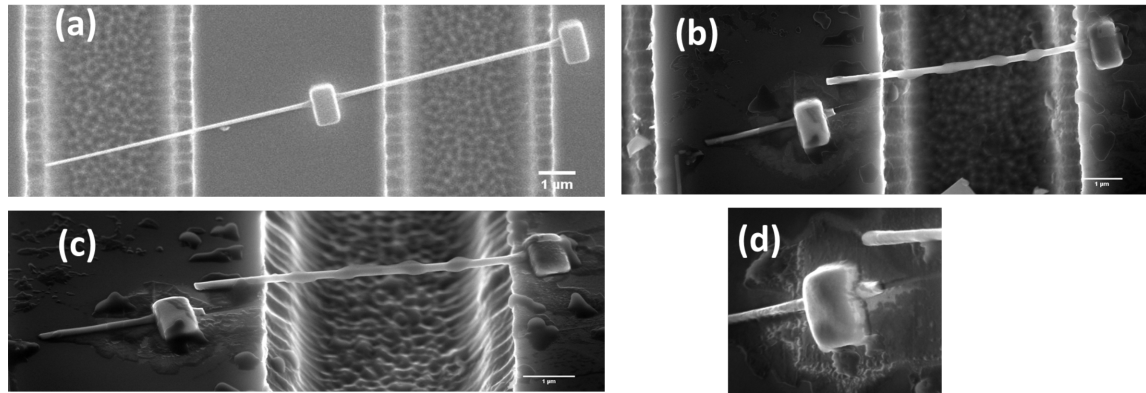

Figure 7.2: a. SEM image of a self suspended NWs1 laying across two micro trenches and glued by depositing in FIB/SEM system.SEM image captured after the nanomechanical testing at **b.** 0° and **c.** 52° tilt. **d.** During loading, the NW1 Fractured close to the Platinum clamping where the maximum stresses are present.

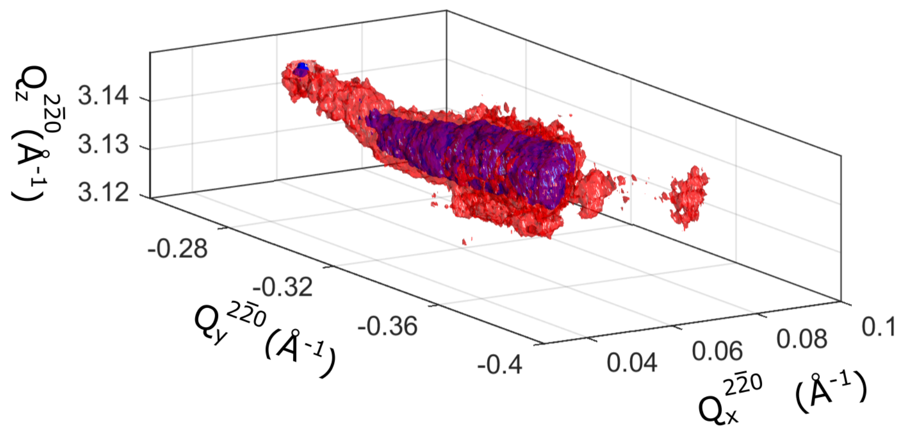

Figure 7.3: Three dimensional iso-surface of diffracted intensity in reciprocal space before lateral three point bending test.

two-dimensional integrated diffracted signals in three different Q-directions are displayed in Fig. 7.4. The Bragg peak was localized at $Q_z = 31.4[nm^{-1}]$ which agrees with the theoretical GaAs $2\bar{2}0$ Bragg position.

The observed Q_y reflection shows a strongly diffuse Bragg peak which indicates the possible presence of strain, defects, or nanowire deformation. It was reported for Au nanowires that the Bragg reflections are strongly elongated and exhibit diffuse scattering for nanowire positions crossing the Si supports. On the other hand, excess deposition of platinum, see Fig. 7.2 - (a), as the adhesive may cause significant compressive strain to the NW thus becoming an additional factor to promote the diffused Bragg peak.

By using an optical microscope at P23, the SFINX tip was coarsely aligned with respect to the NW1. The excitation of the cantilever as well as the feedback loop were turned off and the piezo stage connected to the SFINX tip was displaced with a constant speed of 50[nm/s]. During the loading, we monitor and

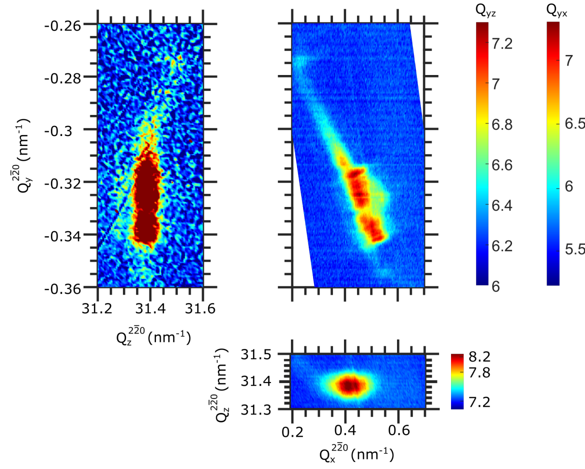

Figure 7.4: RSMs of the $2\bar{2}0$ Bragg reflection of the NW1 recorded by rocking scan.

record the 2D diffraction patterns of the $[2\bar{2}0]$ GaAs Bragg peak to observe any deformation by updating the scan per three seconds. Six consecutive diffraction patterns recorded during the mechanical loading of the nanowire and their corresponding integrated intensities along Q_x are displayed in Fig. 7.5. (c) shows the splitting of the Bragg peak which is an indicator of the tip to NW contact. In the next three scans (d−f), Bragg peak started to drift in positive Q_x direction. It indicates that the NW is rotating, i.e., torsion with the increasing SFINX tip displacement. Surprisingly, the Bragg peak was completely vanished during the next three scans (d−f), which was a clear sign of NW fracture. Although the scan speed could be improved, the low intensity of the diffracted signal was a limiting factor for increasing the scan speed. On the other hand, the speed of SFINX tip was fast too as every scan was recorded after 15[nm] SFINX tip displacement.

After nXRD experiment, NW1 was examined in the FIB/SEM to evidence visible structural differences. As displayed in Fig. 7.2 - (b-c) the NW is not only fractured but also plastically deformed. Fracture site is at the lower platinum clamps as depicted in (d). Qualitatively, plastic deformation is also observed at the broken edge of the NW, near the platinum clamping where the highest stresses are reported[155]. FIB/SEM post-mortem analysis reveals round shaped blobs on the NWs. Similar morphological variations have been reported before[156] where such modifications are attributed to the x-ray beam damage. These contamination blobs may contribute to the local strain in the suspended NW and thus lead to the diffused diffraction signal.

7.4.2 NW2: Elastic deformation

The torsion increases as SFINX tip moves along Q_x, due to non-horizontal components of the applied force given the fact that the NW is not lying perpendicular to the trenches (instead of 90 the nanowire is tilted by 42.5° respect to the Si support) as shown in Fig. 7.6 - (a). Another factor that contributes to the torsion is the scenario where the SFINX tip does not contact the center of the NW for nanomechanical

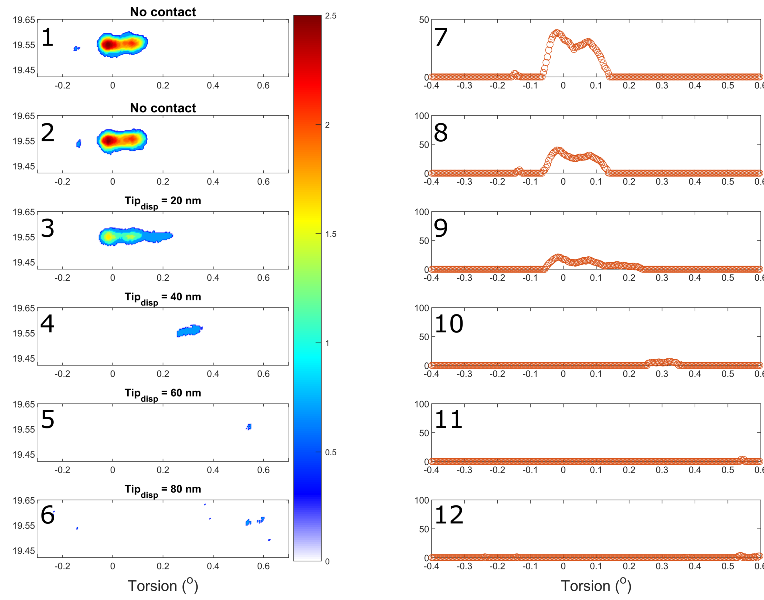

Figure 7.5: 1.-6. 2θ vs torsion plot. NW was contacted by the SFINX tip at (3) where the Bragg peak splitting is observed. **7.-12.** corresponds to the integrated intensity plot of the torsion.

testing.

The elastic response of the Be-doped GaAs NW was investigated by *in-situ* lateral three-point bending test on NW2. As mentioned in previously, the first step for *in-situ* nanomechanical test is the positioning of the SFINX tip and the NW with respect to the micrometer focused X-ray beam. Before alignment, a three-dimensional Reciprocal space mapping was recorded and was later used as a reference, see Fig. 7.9 - (1 & 5). In this experiment, the first coarse alignment was obtained with the optical microscope which positions the SFINX tip in the field of interest with a precision of around 10[μm]. Further refinement was accomplished by lowering the tip about 10[μm] and moving it along Q_x at the speed of 2[nm] per second and simultaneously capturing 2 θ vs θ scan. The recorded scans are presented in Fig.7.7. As soon as the SFINX tip contacts the NW,indicated by the peak splitting in Fig. 7.7 - (d), the movement of SFINX tip was interrupted. Afterward, SFINX tip was displaced in small steps, see (e-i), while bending the NW. The total displacement of the tip was around 10[nm]. The center position of Bragg peak was evaluated by fitting the 2D plots with a Gaussian. The fitting result shows that, with increasing load, Bragg peak shifts by 0.65° in θ with respect to its initial position. A shift in θ corresponds to torsion in the NW and at maximum displacement of the SFINX tip (i), NW has a torsion of 0.65°. Fig. 7.7 - (g-k) displays the unloading of the NW while the SFINX tip was retracted at the speed of 2[nm/s]. After unloading, the Bragg peak elongates along Q_z which may be a consequence of the sticking of the SFINX-tip to the NW leading to the dragging of NW during retraction.Torsion as a function of time is plotted in Fig. 7.8. Fig. 7.9 - (a) shows the recorded three-dimension RSMs of NW before and after the *in-situ* lateral three-point bending test. Sub-graph (1) was captured before bending while sub-graph

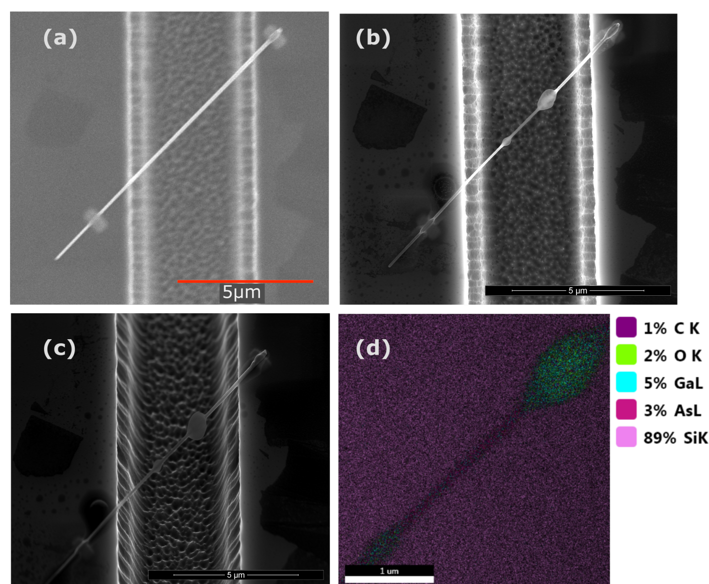

Figure 7.6: a. SEM image of self suspended NW2 before nanomechanical testing. **b.-c.** SEM image taken after nXRD and nanomechanical testing **b.** 0° and (c) 52° tilt. Analogous to NW1, round shaped blobs were observed for NW2 which was further investigated by Energy-dispersive X-ray spectroscopy (EDX). **d.** Elemental composition of round blobs determined by EDX.

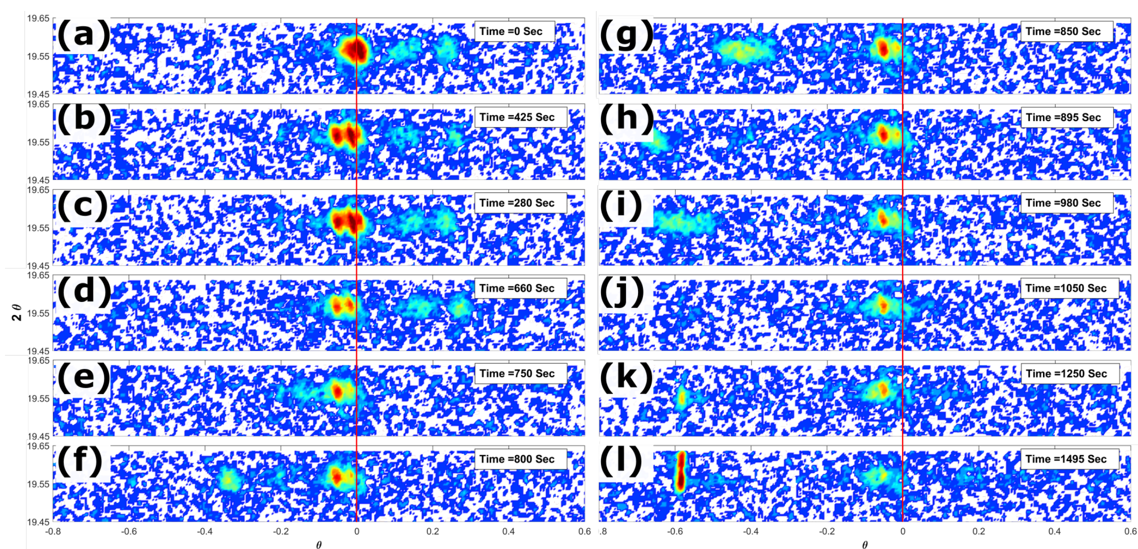

Figure 7.7: 2 θ vs θ plot. Relative movement of the Bragg peak in θ with respect to zero corresponds to the rotation or the torsion of the NW. **a.-c.** Scans during the SFINX alignment in the vicinity of the NW **d.** NW comes in contact with the SFINX tip. **e.-i.** SFINX tip moved and bend the NW along Q_x at the speed of 2[nm/s]. **j.-l.** SFINX tip was retracted at the speed of 2[nm/s].

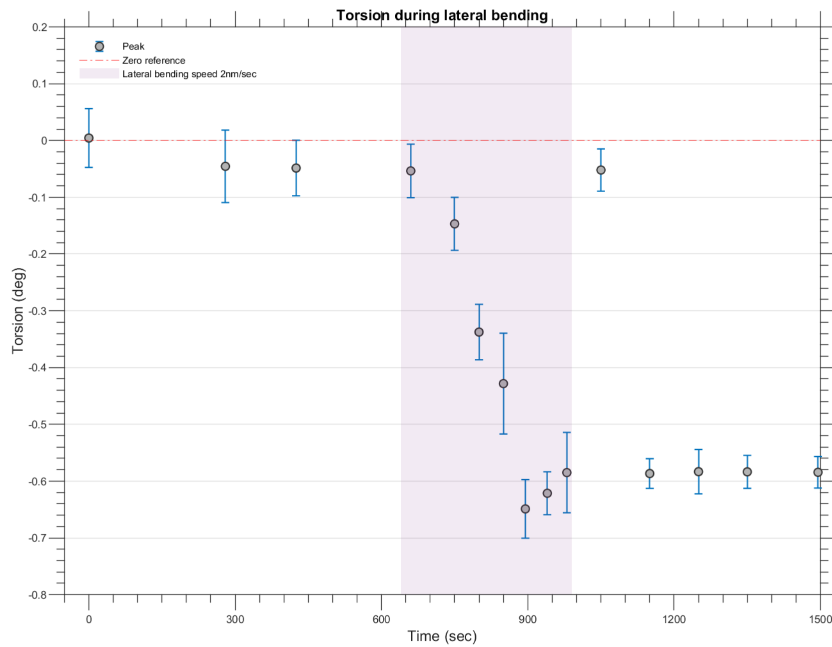

Figure 7.8: Torsion induced in NW2 is plotted as function of time. The NW was bent during 645[s] to 990[s] with SFINX tip for total displacement of 10[nm] with the steps of 2[nm]. Red dotted line is the reference for zero torsion.

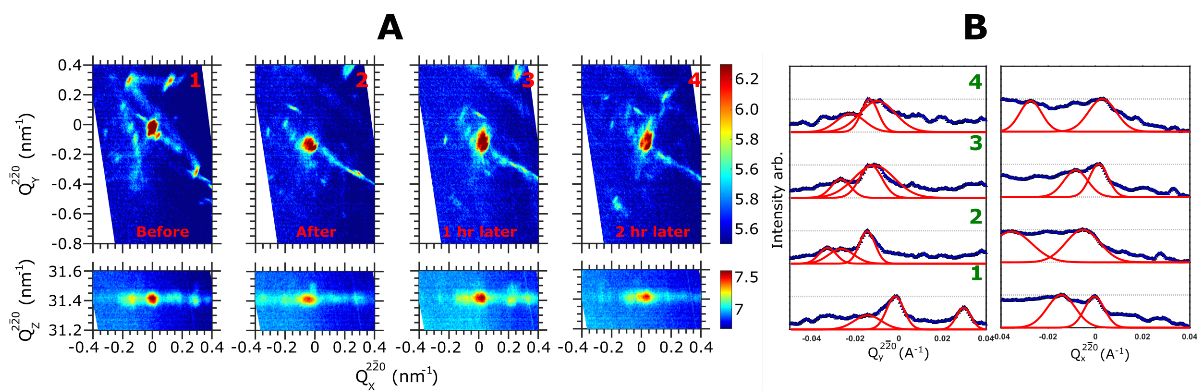

Figure 7.9: A. Two dimensional cuts from the three dimensional RSMs taken before (1) and after $(2\text{-}4)$ the *in-situ* lateral three point bending test. **B.** 2D cuts from (**A.**) were integrated along Q_x and Q_y and fitted with Gaussian to extract the Bragg peak position.

(2-4) were recorded after 5[min], 1 [hr], and 2 [hr] after the nanomechanical testing, respectively. The 2D cuts from 3D diffraction patterns are fitted with 2D Gaussians to localize the Bragg peak position and the fitting results are presented in Fig. 7.9 - (b). Since Q_x and Q_y are sensitive to torsion and bending, respectively, and the Bragg peak exclusively moves in these Q_{xy} plane it is reasonable to measure the peak displacement at fixed Q_z. For better understanding and comparison, the maximum intensity of the RSM recorded before the lateral three-point bending test along Q_x and Q_y is positioned at zero, as depicted in Fig. 7.9 - (1). Relative displacement of Q_x and Q_y of the Bragg peak with respect to the reference is depicted in Fig. 7.9 - (2-4). Although time scans recording of the Bragg peak during the loading and unloading of NW does not show a full elastic relaxation, the RSMs measured later revealed that the NW is actually elastically relaxed. Fig. 7.9 - (2-4) qualitatively shows that the Bragg peak is approximately located at the same Q_x and Q_y for all three RSMs which is verified by the fitting results presented in their respective sub-graphs. NW2 was further investigated in SEM/FIB for structural variations. As shown in Fig. 7.6 - (c) there is no visible change in the shape and form of NW but similar to NW1 multiple round shaped blobs attached to NW were found. In order to investigate the chemical composition of these blobs attached to the NW, site specific Energy-dispersive X-ray spectroscopy (EDX) was performed on them. EDX reveals the presence of oxygen with gallium on these blobs, which may be identified as Ga_2O_3 as previously reported[156]. The remaining elemental composition is displayed in Fig. 7.6 - (d).

7.4.3 NW3: Torsion relaxation

In this experiment, we tried to detect and visualize the anelastic relaxation in Be-doped GaAs NW, NW3, by *in-situ* lateral three-point bending test. The SEM image of the pristine NW3 is presented in Fig. 7.10 - (a). A three-dimensional RSM was recorded before bending to register the pristine condition of NW in the reciprocal space as reference. After the alignment, the SFINX were moved along Q_x and simultaneously following the Bragg peak as mentioned in the previous subsection. 2 θ vs θ scan recorded during the loading and unloading of the NW are presented in Fig. 7.11. The piezo motor was interrupted as soon as the SFINX tip comes in contact with the NW which is visible in Fig. 7.11 - (b) by the elongation of the Bragg peak. Small Bragg peak on the left side disappears once the SFINX tip makes contact with the NW. As mentioned earlier, torsion is induced as soon as the SFINX tip touches the NW given the fact that the SFINX tip is not perfectly align with respect to the center of the NW and non-horizontal component of applied force cause a torque in NW thus inducing twist.

The speed of the SFINX tip was 10[nm/s] and given the scan rate of one scan per 3 second, the SFINX tip was moved approximately 30[nm] after the contact. As depicted in Fig. 7.11 - (c-f) & 7.12, the NW was kept bent for approximately 6[min]. During the loading, the Bragg peak shifts by 0.4° in Q_x, and remains at this position. This shift represents the bending induced rotation of the NW, i.e., torsion, and it was the only assessable parameter for two reasons. First, a rocking scan was not an option to record the three-dimensional RSM as it may induce vibrations into the system that can cause damage to the NW

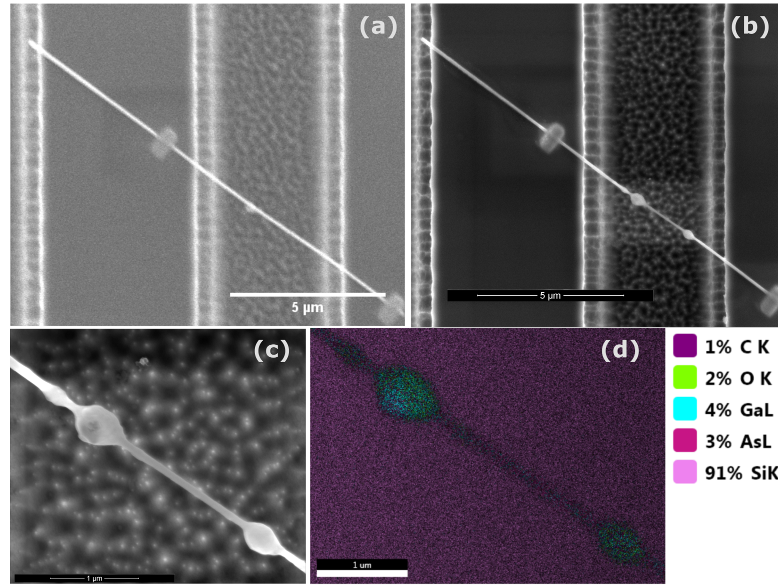

Figure 7.10: **a.** SEM image of self suspended pristine NWs, NWs2, before *in-situ* three-point bending test. **b.** SEM image taken after nXRD and nanomechanical testing 0° tilt. Analogous to NW1 and NW2, round shaped blobs were observed for NW3 which was further investigated by Energy-dispersive X-ray spectroscopy (EDX). **c.** SEM image containing the section of NW and contamination for the site-specific EDX spectroscopy **d.** Elemental composition of round blobs determined by EDX in a overlaying map with subplot **c**.

or crash the SFINX tip into the substrate. Second, assuming that the SFINX tip was perfectly placed at the center of the NW and the bending profile was symmetric, then Bragg peak position along Q_y is fixed. Thus, the in-plane bending is only sensitive to the bending gradient rather than bending itself, and as discussed earlier, the displacement of SFINX tip along Q_x aligns the bending axis of the NW around the normal of $[2\bar{2}0]$ planes thus hindering the information about the bending. The NW was released after keeping it bent for approximately 6[min]. After release, the primary peak gradually went back to zero torsion in approximately 2[min]. Once the SFINX tip is completely retracted, the small peak on the left starts to reappear. A full evolution of both Bragg peaks are presented as a function of time in Fig. 7.12. The result shows that the torsion or rotation of the NW does not completely relax once the applied stress is removed but the relaxation is rather time dependent as witnessed previously in section 6.2. The relaxation was further verified by the RSMs measured after the retraction of the SFINX tip. Fig. 7.13 presents the RSMs and their respective Gaussian fits before Fig. 7.13 - (1) and after Fig. 7.13 - (2-4) the *in-situ* lateral three-point bending tests. RSM in sub-graph 2, 3 and 4 were measured 5[min], 1.5[hr] and 2[hr] after the nano-mechanical test. To measure the relative position of the Bragg peak after unloading, the maximum intensity of Q_{xy} and Q_{xz} reflections in RSMs measured before nanomechanical testing is placed at zero. It is clear from the RSMs in (b-c) that the Bragg peak is moving along Q_y which indicates relaxation of NW as bending gradient, approximately $-0.1[nm^{-1}]$. Simultaneously, the Bragg peak drifts to $-0.15[nm^{-1}]$ in Q_x. Given the fact that the bending and torsion in NW3 have not completely relaxed, even two hours later, and time dependent torsion relaxation of NW immediately after

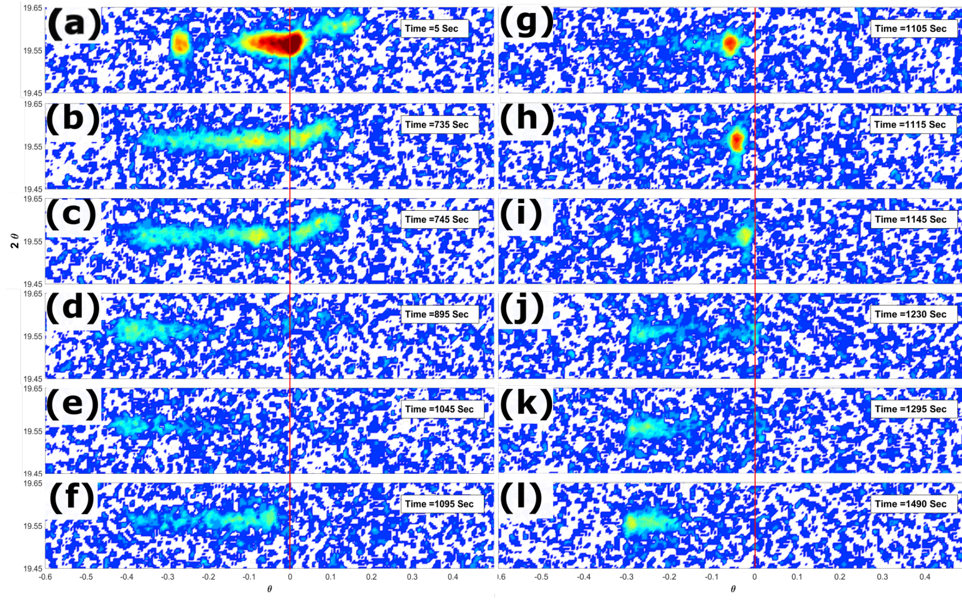

Figure 7.11: $2\,\theta$ vs θ plot. Relative movement of the Bragg peak in θ with respect to zero corresponds to the rotation or the torsion of the NW. **a.** Scans during the alignment SFINX and the NW alignment **b.** NW comes in contact with the SFINX tip when moving it along Q_x at the speed of 10[nm/s]. **c.** SFINX tip was interrupted and the NW kept under the stress from **e.** The SFINX tip was retracted and the NW was released. **f.-j.** The torsion in the NW relaxes as function of time. **k.-l.** Full retraction of the SFINX tip.

unloading incorporates the idea of anelastic relaxation of NW. Although the bending profile was not accessible during this experiment, torsion in the NW is not sufficient to predict the presence of anelastic relaxation due to the fact that it may be influenced by other factors such as SFINX tip alignment, contact point on the NW, non-symmetric bending angle, applied force direction and influence of SFINX during the retraction. Analogous to NW1 and NW2, NW3 is also found with round shape Ga_2O_3 contamination, identified by EDX in SEM/FIB. Elemental composition of the round shape blob is listed in Fig. 7.10 - (c-d).

The primary aim of the *in-situ* three-point bending test on Be-doped GaAs NWs was to examine the elastic to plastic transition and to quantify the anelastic relaxation as function of time with a submicrometer focused x-ray beam. Multiple factors such as a very large beam size, low intensity of x-ray beam, and equipment restrictions effectively constraint the required results and information. We registered elastic and time depend torsion relaxation in the NW but without access to the actual bending profile, a numerical estimation by FEM model is not beneficial either. The observed relaxation time supports the idea of long range diffusion of the point defects in the NW, which is characteristic to the Gorsky effect. By using the Gorsky model the diffusion coefficient, D, can be estimated.

$$\tau = \frac{d^2}{\pi^2 D} \tag{7.1}$$

Here the diameter, $d = 190$[nm], and the relaxation time $\tau = 135$[s] yields a diffusion coefficient

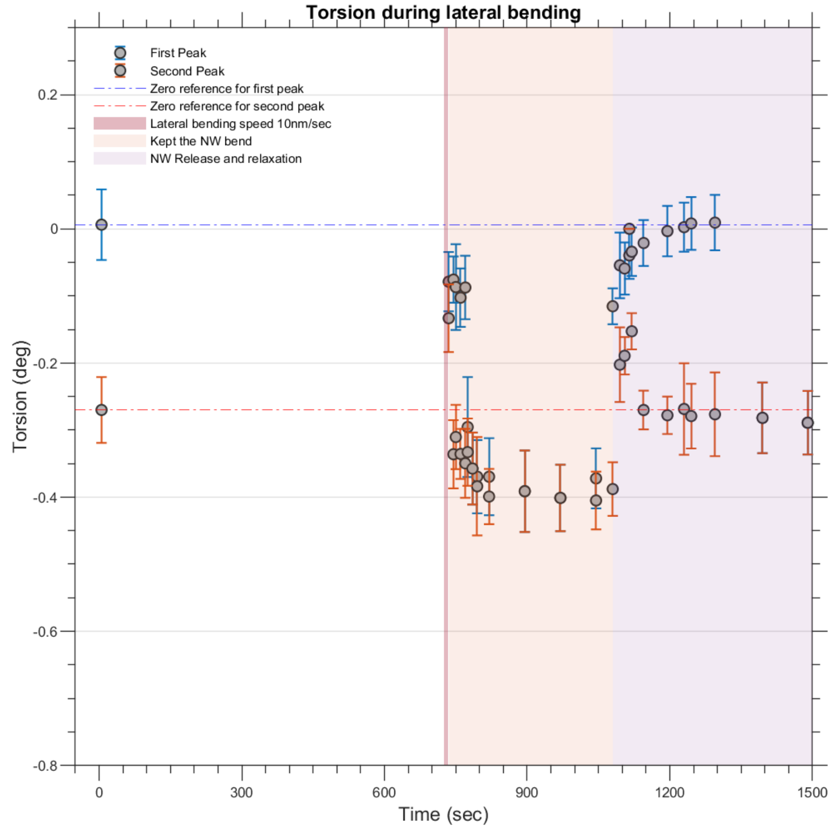

Figure 7.12: Torsion induced in NW3 is plotted as function of time. The NW was contacted at 745[s] and kept under the applied force until 1085[s] with SFINX tip for total displacement of 30 [nm]. Blue dotted line is the reference for zero torsion for the main peak, which shows the time dependent torsion relaxation.

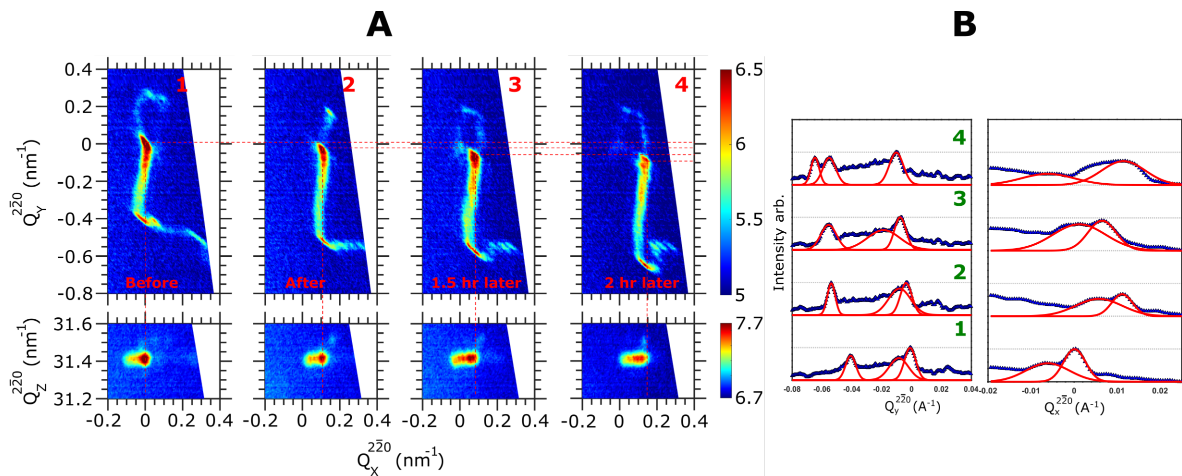

Figure 7.13: A. Two dimensional cuts from the three dimensional RSMs taken before (1) and after (2-4) the *in-situ* lateral three point bending test. **B.** 2D cuts from **A.** were integrated along Q_x and Q_y and fitted with Gaussian to extract the Bragg peak position. Drifting of Bragg peak in Q_{xy} represents the time bending and torsion relaxation of the NW after the *in-situ* lateral three point bending test.

$2.71 \times 10^{-13} [cm^2/s]$ which is consistent with the diffusion coefficient estimated by using FEM in the previous chapter. Regardless of end-station setbacks, the findings from the experiment contributed to the understanding of mechanics at the nanoscale. It conclusively establishes that a three-point bending test is feasible after few technical improvements at the end-station. The focusing mechanics at P23 promise to deliver a stable and sub micrometer focused beam in the vertical direction, which is essential to monitor the deformation of the NW at the point of contact. During the bending of the NW, it is possible to record the diffraction maps by a lateral translation of the Be CRLs, thus scanning the focused x-ray beam across the sample surface. It will also help to avoid the vibrations induced by the movement of the diffractometer during the angular scans.

8 Conclusion

In this dissertation, we have studied the dynamical mechanical behavior of semiconductor based GaAs Nanowires (NWs) by employing conventional *in-situ* X-ray scattering methods for the structural characterization and a specially designed Atomic Force Microscopy (AFM) called "Scanning Force Microscope for in situ Nanofocused X-ray diffraction (SFINX)" for nanomechanical testing. This included the nanoscale mechanical perturbation of NW in FIB/SEM and the development of the analysis strategies e.g., Finite Element Method (FEM) and Digital image correlation (DIC). These experimental tools provided valuable insights into mechanics of the semiconductor NWs at the fundamental level. In particular, we extract information about the anelastic strain as a consequency of the Gorsky effect in Be-doped GaAs NW in their as-grown geometry.

1. Targeted investigations have been performed on high quality GaAs NWs prepared by using, self-catalyzed GaAs NWs, with diameters ranging from150 to 200 nm and lengths of 6 to 8 μm, were grown on Si(111) pre-patterned substrate by Molecular Beam Epitaxy (MBE) via vapor-liquid-solid mechanism (VLS). We applied systematic dynamic loading, i.e., electromechanically induced vibrations on single NWs, either by increasing the amplitude of resonance or the dwell time. We planned to examine the crystalline structure and phases of these vibrated NWs by using *ex-situ* Bragg Coherent X-rays Diffraction Imaging (BCDI) at beamline CRISTAL, SOLEIL in order to understand the impact of the deformation and mechanical behavior induced by the dynamic loading. The *ex-situ* experiment was planned for March 2020 but due to the COVID-19 pandemic spread the experiment has been cancelled and shifted twice by the synchrotron facility.

2. Using W-probes inside FIB/SEM chamber, we demonstrated the lateral bending and buckling tests on the free standing Be-doped GaAs NWs, with diameters ranging from 150 to 200 nm and lengths of 20 to 25 μm, grown on Si(111) substrate. After bending, the NWs were kept under a constant stress for an extended period of time. The NWs exhibit anelastic relaxation after the spontaneous elastic strain relaxation as soon as the external stress was removed. We extract the anelastic strain relaxation from FIB/SEM experiment by using a DIC algorithm. Additionally, we developed a mathematical model, a system of highly coupled nonlinear Partial Differential Equations (PDE) and by employing FEM capabilities in a numerical analysis software *COMSOL Multiphysics*, we extract the anelastic strain profiles as a function relaxation time of the NW. This mathematical model is based on the diffusion of Be atoms inside Be-doped GaAs NWs. We further found that the results from the mathematical model conclusively fits to the experimental results when considering initial concentration of the Be-atoms equal to nominal doping concentration of the NWs. The drifting of Be atoms under stress is a very nice evidence of "Gorsky Effect" in the NW.

3. After the successful identification of the Gorsky Effect by characterization in FIB/SEM chamber the mechanical properties of Be doped GaAs NWs was further investigated by employing Scanning Force Microscope for in situ Nanofocused X-ray diffraction (SFINX) and XRD using focused synchrotron radiation . The nano-mechanical testing on NWs was carried out in lateral three point bending configuration at the microfocus station beamline P23at the 3rd generation synchrotron radiation source PETRA III. The sample was prepared by detaching the NWs from substrate by immersing in dilute CH_2Cl_2 dichloromethane solution, later placing them into an ultrasonication bath and then transferring them into Si-micro trenches by drop casting method. The bending was induced in NWs by the lateral movement of the SFINX and thus blocking the access to the bending profile of the NW. Despite the experimental diffiulties we demonstrate fracture, elastic and plastic deformation, and time dependent anelastic torsion relaxation in Be-doped GaAs. The maximum value of the torsion achieved was $0.65°$. The relaxation time for this anelastic relaxation yields a diffusion coefficient $2.71 \times 10^{-13} [cm^2/s]$ which is consistent with the FEM model.

In summary, within this thesis, by two kinds of mechanical tests, we verified the Gorsky effect in the semiconductor Be doped GaAs NWs i.e., three-point bending tests and cantilever-based lateral bending test. NWs also exhibit elastic plastic response to the external mechanical loading. Additional understanding of the plastic behavior in NWs requires FEM simulations followed by Bragg Coherent X-rays Diffraction Imaging (BCDI). It will facilitate the structural analysis of the fractured and plastically deformed NW. Thus providing information about the stored dislocation in NW and the mechanisms responsible for room temperature plastic deformation in GaAs NWs. Consequently, a sub-micrometer focused x-ray beam Bragg Coherent X-rays Diffraction Imaging (BCDI) will provide structural information after the impact of the systemic and dynamic loading on the NWs. It will be worthwhile to employ

other simulation techniques with the potential to explain plastic deformation such as molecular dynamics and discrete dislocation dynamics. Apart from the FEM simulations, these techniques will provide a deeper insight into the plastic deformation. In addition to FEM and other simulation methods, TEM and STEM based structural characterization will certainly provide a direct and discrete understanding of the mechanism.

Finally, there are no reports, except Cheng et al. [151], regarding the investigation of Gorsky effect in semiconductor NW. In order to get more controlled deformation conditions one may imagine using SFINX in three point bending configuration and in conjunction with micro Laue diffraction as has been done in the past [27]. Thee great sensitivity of Laue diffraction to lattice rotation could yield a very detailed anelastic relaxation experiment.

For future investigations, a few minor upgrades to FIB/SEM will improve the nanomechenical testing capabilities significantly. First, a nanomanipulator with piezomotors will increase the control during the bending by absolute movement in xyz rather than angular span. It will provide the planar bending of the NW and consequently reduce the unwanted transformations to perceive the actual bending of the NW. Secondly, a navigation camera will increase the precision of alignment as well as provide access to three-dimensional information during scanning.

References

[1] M. S. Rodrigues, T. W. Cornelius, T. Scheler, C. Mocuta, A. Malachias, R. Magalhães-Paniago, O. Dhez, F. Comin, T. H. Metzger, and J. Chevrier. In situ observation of the elastic deformation of a single epitaxial SiGe crystal by combining atomic force microscopy and micro x-ray diffraction. *Journal of Applied Physics*, 106(10):103525, nov 2009.

[2] M. Dupraz, G. Beutier, T. W. Cornelius, G. Parry, Z. Ren, S. Labat, M.-I. Richard, G. A. Chahine, O. Kovalenko, M. De Boissieu, E. Rabkin, M. Verdier, and O. Thomas. 3d imaging of a dislocation loop at the onset of plasticity in an indented nanocrystal. *Nano Letters*, 17(11):6696–6701, oct 2017.

[3] Anton Davydok, Thomas Cornelius, Zhe Ren, Cedric Leclere, Gilbert Chahine, Tobias Schülli, Florian Lauraux, Gunther Richter, and Olivier Thomas. In situ coherent x-ray diffraction during three-point bending of a au nanowire: Visualization and quantification. *Quantum Beam Science*, 2(4):24, nov 2018.

[4] Friso van der Veen and Franz Pfeiffer. Coherent x-ray scattering. *Journal of Physics: Condensed Matter*, 16(28):5003–5030, jul 2004.

[5] L. A. Giannuzzi. *Introduction to Focused Ion Beams*. Springer-Verlag GmbH, 2005.

[6] Nanosensors self-sensing and self-actuating akiyama probe. https://www.nanosensors.com/blog/self-sensing-self-actuating-akiyama-probe-screencast-has-1500-views. Accessed: 2020-09-30.

[7] Beamline p23, desy. https://photon-science.desy.de/facilities/petra_iii/beamlines/p23_in_situ_and_nano_x_ray_diffraction/beamline_layout/index_eng.html. Accessed: 2010-09-30.

[8] M. D. Uchic. Sample dimensions influence strength and crystal plasticity. *Science*, 305(5686):986–989, aug 2004.

[9] Jiangwei Wang, Zhi Zeng, Christopher R. Weinberger, Ze Zhang, Ting Zhu, and Scott X. Mao. In situ atomic-scale observation of twinning-dominated deformation in nanoscale body-centred cubic tungsten. *Nature Materials*, 14(6):594–600, mar 2015.

[10] Yongke Sun, Scott E. Thompson, and Toshikazu Nishida. *Strain Effect in Semiconductors*. Springer US, 2010.

[11] Amit Banerjee, Daniel Bernoulli, Hongti Zhang, Muk-Fung Yuen, Jiabin Liu, Jichen Dong, Feng Ding, Jian Lu, Ming Dao, Wenjun Zhang, Yang Lu, and Subra Suresh. Ultralarge elastic deformation of nanoscale diamond. *Science*, 360(6386):300–302, apr 2018.

[12] Hongti Zhang, Jerry Tersoff, Shang Xu, Huixin Chen, Qiaobao Zhang, Kaili Zhang, Yong Yang, Chun-Sing Lee, King-Ning Tu, Ju Li, and Yang Lu. Approaching the ideal elastic strain limit in silicon nanowires. *Science Advances*, 2(8):e1501382, aug 2016.

[13] D. Kiener, W. Grosinger, G. Dehm, and R. Pippan. A further step towards an understanding of size-dependent crystal plasticity: In situ tension experiments of miniaturized single-crystal copper samples. *Acta Materialia*, 56(3):580–592, feb 2008.

[14] Michael D. Uchic and Dennis M. Dimiduk. A methodology to investigate size scale effects in crystalline plasticity using uniaxial compression testing. *Materials Science and Engineering: A*, 400-401:268–278, jul 2005.

[15] Robert Maaß, Steven Van Petegem, Helena Van Swygenhoven, Peter M. Derlet, Cynthia A. Volkert, and Daniel Grolimund. Time-resolved laue diffraction of deforming micropillars. *Physical Review Letters*, 99(14), oct 2007.

[16] H. Van Swygenhoven and S. Van Petegem. The use of laue microdiffraction to study small-scale plasticity. *JOM*, 62(12):36–43, dec 2010.

[17] Xiaodong Li and Bharat Bhushan. A review of nanoindentation continuous stiffness measurement technique and its applications. *Materials Characterization*, 48(1):11–36, feb 2002.

[18] W.C. Oliver and G.M. Pharr. An improved technique for determining hardness and elastic modulus using load and displacement sensing indentation experiments. *Journal of Materials Research*, 7(6):1564–1583, jun 1992.

[19] Claus-Christian Röhlig, Merten Niebelschütz, Klemens Brueckner, Katja Tonisch, Oliver Ambacher, and Volker Cimalla. Elastic properties of nanowires. *physica status solidi (b)*, 247(10):2557–2570, sep 2010.

[20] C. Kirchlechner, D. Kiener, C. Motz, S. Labat, N. Vaxelaire, O. Perroud, J.-S. Micha, O. Ulrich, O. Thomas, G. Dehm, and J. Keckes. Dislocation storage in single slip-oriented cu micro-tensile samples: new insights via x-ray microdiffraction. *Philosophical Magazine*, 91(7-9):1256–1264, mar 2011.

[21] Lihua Wang, Ze Zhang, and Xiaodong Han. In situ experimental mechanics of nanomaterials at the atomic scale. *NPG Asia Materials*, 5(2):e40–e40, feb 2013.

[22] Bin Chen, Qiang Gao, Yanbo Wang, Xiaozhou Liao, Yiu-Wing Mai, Hark Hoe Tan, Jin Zou, Simon P. Ringer, and Chennupati Jagadish. Anelastic behavior in GaAs semiconductor nanowires. *Nano Letters*, 13(7):3169–3172, jun 2013.

[23] A. M. Minor, E. T. Lilleodden, E. A. Stach, and J. W. Morris. In-situ transmission electron microscopy study of the nanoindentation behavior of al. *Journal of Electronic Materials*, 31(10):958–964, oct 2002.

[24] C. Kirchlechner, J. Keckes, C. Motz, W. Grosinger, M.W. Kapp, J.S. Micha, O. Ulrich, and G. Dehm. Impact of instrumental constraints and imperfections on the dislocation structure in micron-sized cu compression pillars. *Acta Materialia*, 59(14):5618–5626, aug 2011.

[25] J. Gamcová, G. Mohanty, Š. Michalik, J. Wehrs, J. Bednarčík, C. Krywka, J. M. Breguet, J. Michler, and H. Franz. Mapping strain fields induced in zr-based bulk metallic glasses during in-situ nanoindentation by x-ray nanodiffraction. *Applied Physics Letters*, 108(3):031907, jan 2016.

[26] Angelika Zeilinger, Juraj Todt, Christina Krywka, Martin Müller, Werner Ecker, Bernhard Sartory, Michael Meindlhumer, Mario Stefenelli, Rostislav Daniel, Christian Mitterer, and Jozef Keckes. In-situ observation of cross-sectional microstructural changes and stress distributions in fracturing TiN thin film during nanoindentation. *Scientific Reports*, 6(1), mar 2016.

[27] Zhe Ren, Francesca Mastropietro, Anton Davydok, Simon Langlais, Marie-Ingrid Richard, Jean-Jacques Furter, Olivier Thomas, Maxime Dupraz, Marc Verdier, Guillaume Beutier, Peter Boesecke, and Thomas W. Cornelius. Scanning force microscope forin situnanofocused x-ray diffraction studies. *Journal of Synchrotron Radiation*, 21(5):1128–1133, aug 2014.

[28] Cédric Leclere, Thomas W. Cornelius, Zhe Ren, Anton Davydok, Jean-Sébastien Micha, Odile Robach, Gunther Richter, Laurent Belliard, and Olivier Thomas. In situbending of an au nanowire monitored by micro laue diffraction. *Journal of Applied Crystallography*, 48(1):291–296, jan 2015.

[29] M. Stefenelli, R. Daniel, W. Ecker, D. Kiener, J. Todt, A. Zeilinger, C. Mitterer, M. Burghammer, and J. Keckes. X-ray nanodiffraction reveals stress distribution across an indented multilayered CrN–cr thin film. *Acta Materialia*, 85:24–31, feb 2015.

[30] T. Scheler, M. Rodrigues, T. W. Cornelius, C. Mocuta, A. Malachias, R. Magalhães-Paniago, F. Comin, J. Chevrier, and T. H. Metzger. Probing the elastic properties of individual nanostructures by combining in situ atomic force microscopy and micro-x-ray diffraction. *Applied Physics Letters*, 94(2):023109, jan 2009.

[31] Marcus C. Newton, Steven J. Leake, Ross Harder, and Ian K. Robinson. Three-dimensional imaging of strain in a single ZnO nanorod. *Nature Materials*, 9(2):120–124, dec 2009.

[32] Mark A. Pfeifer, Garth J. Williams, Ivan A. Vartanyants, Ross Harder, and Ian K. Robinson. Three-dimensional mapping of a deformation field inside a nanocrystal. *Nature*, 442(7098):63–66, jul 2006.

[33] Allison Yau, Wonsuk Cha, Matthew W. Kanan, G. Brian Stephenson, and Andrew Ulvestad. Bragg coherent diffractive imaging of single-grain defect dynamics in polycrystalline films. *Science*, 356(6339):739–742, may 2017.

[34] N. Vaxelaire, S. Labat, T.W. Cornelius, C. Kirchlechner, J. Keckes, T. Schulli, and O. Thomas. New insights into single-grain mechanical behavior from temperature-dependent 3-d coherent x-ray diffraction. *Acta Materialia*, 78:46–55, oct 2014.

[35] J. Shin, T. W. Cornelius, S. Labat, F. Lauraux, M.-I. Richard, G. Richter, N. P. Blanchard, D. S. Gianola, and O. Thomas. In situ bragg coherent x-ray diffraction during tensile testing of an individual au nanowire. *Journal of Applied Crystallography*, 51(3):781–788, may 2018.

[36] Maxime Dupraz, Guillaume Beutier, David Rodney, Dan Mordehai, and Marc Verdier. Signature of dislocations and stacking faults of face-centred cubic nanocrystals in coherent x-ray diffraction patterns: a numerical study. *Journal of Applied Crystallography*, 48(3):621–644, apr 2015.

[37] A. A. Minkevich, T. Baumbach, M. Gailhanou, and O. Thomas. Applicability of an iterative inversion algorithm to the diffraction patterns from inhomogeneously strained crystals. *Physical Review B*, 78(17), nov 2008.

[38] A. A. Minkevich, E. Fohtung, T. Slobodskyy, M. Riotte, D. Grigoriev, M. Schmidbauer, A. C. Irvine, V. Novák, V. Holý, and T. Baumbach. Selective coherent x-ray diffractive imaging of displacement fields in (ga,mn)as/GaAs periodic wires. *Physical Review B*, 84(5), aug 2011.

[39] Ravi Agrawal and Horacio D. Espinosa. Giant piezoelectric size effects in zinc oxide and gallium nitride nanowires. a first principles investigation. *Nano Letters*, 11(2):786–790, feb 2011.

[40] Thomas Mikolajick, André Heinzig, Jens Trommer, Sebastian Pregl, Matthias Grube, Gianaurelio Cuniberti, and Walter M. Weber. Silicon nanowires - a versatile technology platform. *physica status solidi (RRL) - Rapid Research Letters*, 7(10):793–799, jul 2013.

[41] Peidong Yang, Ruoxue Yan, and Melissa Fardy. Semiconductor nanowire: What's next? *Nano Letters*, 10(5):1529–1536, may 2010.

[42] Jun Zhou, Yudong Gu, Peng Fei, Wenjie Mai, Yifan Gao, Rusen Yang, Gang Bao, and Zhong Lin Wang. Flexible piezotronic strain sensor. *Nano Letters*, 8(9):3035–3040, sep 2008.

[43] Garrett J. Hayes and Bruce M. Clemens. Laser liftoff of gallium arsenide thin films. *MRS Communications*, 5(1):1–5, feb 2015.

[44] R. S. Wagner and W. C. Ellis. VAPOR-LIQUID-SOLID MECHANISM OF SINGLE CRYSTAL GROWTH. *Applied Physics Letters*, 4(5):89–90, mar 1964.

[45] A.Y. Cho and J.R. Arthur. Molecular beam epitaxy. *Progress in Solid State Chemistry*, 10:157–191, jan 1975.

[46] B A Joyce. Molecular beam epitaxy. *Reports on Progress in Physics*, 48(12):1637–1697, dec 1985.

[47] Kimberly A. Dick. A review of nanowire growth promoted by alloys and non-alloying elements with emphasis on au-assisted III–v nanowires. *Progress in Crystal Growth and Characterization of Materials*, 54(3-4):138–173, sep 2008.

[48] Premila Mohan, Rajesh Bag, Sunita Singh, Anand Kumar, and Renu Tyagi. Mechanism of self-assembled growth of ordered GaAs nanowire arrays by metalorganic vapor phase epitaxy on GaAs vicinal substrates. *Nanotechnology*, 23(2):025601, dec 2011.

[49] Kimberly A. Dick, Knut Deppert, Magnus W. Larsson, Thomas Mårtensson, Werner Seifert, L. Reine Wallenberg, and Lars Samuelson. Synthesis of branched 'nanotrees' by controlled seeding of multiple branching events. *Nature Materials*, 3(6):380–384, may 2004.

[50] Werner Seifert, Magnus Borgström, Knut Deppert, Kimberly A. Dick, Jonas Johansson, Magnus W. Larsson, Thomas Mårtensson, Niklas Sköld, C. Patrik T. Svensson, Brent A. Wacaser, L. Reine Wallenberg, and Lars Samuelson. Growth of one-dimensional nanostructures in MOVPE. *Journal of Crystal Growth*, 272(1-4):211–220, dec 2004.

[51] Kimberly A. Dick, Knut Deppert, Magnus W. Larsson, Thomas Mårtensson, Werner Seifert, L. Reine Wallenberg, and Lars Samuelson. Synthesis of branched 'nanotrees' by controlled seeding of multiple branching events. *Nature Materials*, 3(6):380–384, may 2004.

[52] Yury Berdnikov, Igor Ilkiv, Nickolay Sibirev, Evgeniy Ubyivovk, and Alexei Bouravleuv. Comparison of GaAs nanowire growth seeded by ag and au colloidal nanoparticles on silicon. *Nanotechnology*, 31(37):374005, jun 2020.

[53] C. Colombo, D. Spirkoska, M. Frimmer, G. Abstreiter, and A. Fontcuberta i Morral. Ga-assisted catalyst-free growth mechanism of GaAs nanowires by molecular beam epitaxy. *Physical Review B*, 77(15), apr 2008.

[54] A. Fontcuberta i Morral, C. Colombo, G. Abstreiter, J. Arbiol, and J. R. Morante. Nucleation mechanism of gallium-assisted molecular beam epitaxy growth of gallium arsenide nanowires. *Applied Physics Letters*, 92(6):063112, feb 2008.

[55] U. Jahn, J. Lähnemann, C. Pfüller, O. Brandt, S. Breuer, B. Jenichen, M. Ramsteiner, L. Geelhaar, and H. Riechert. Luminescence of GaAs nanowires consisting of wurtzite and zinc-blende segments. *Physical Review B*, 85(4), jan 2012.

[56] Peter Krogstrup, Jun Yamasaki, Claus B. Sørensen, Erik Johnson, Jakob B. Wagner, Robert Pennington, Martin Aagesen, Nobuo Tanaka, and Jesper Nygård. Junctions in axial III-v heterostructure nanowires obtained via an interchange of group III elements. *Nano Letters*, 9(11):3689–3693, nov 2009.

[57] Sébastien Plissard, Kimberly A Dick, Guilhem Larrieu, Sylvie Godey, Ahmed Addad, Xavier Wallart, and Philippe Caroff. Gold-free growth of GaAs nanowires on silicon: arrays and polytypism. *Nanotechnology*, 21(38):385602, aug 2010.

[58] D. Spirkoska, J. Arbiol, A. Gustafsson, S. Conesa-Boj, F. Glas, I. Zardo, M. Heigoldt, M. H. Gass, A. L. Bleloch, S. Estrade, M. Kaniber, J. Rossler, F. Peiro, J. R. Morante, G. Abstreiter, L. Samuelson, and A. Fontcuberta i Morral. Structural and optical properties of high quality zinc-blende/wurtzite GaAs nanowire heterostructures. *Physical Review B*, 80(24), dec 2009.

[59] Chin-Yu Yeh, Z. W. Lu, S. Froyen, and Alex Zunger. Zinc-blende–wurtzite polytypism in semiconductors. *Physical Review B*, 46(16):10086–10097, oct 1992.

[60] Kimberly A Dick, Philippe Caroff, Jessica Bolinsson, Maria E Messing, Jonas Johansson, Knut Deppert, L Reine Wallenberg, and Lars Samuelson. Control of III–v nanowire crystal structure by growth parameter tuning. *Semiconductor Science and Technology*, 25(2):024009, jan 2010.

[61] Masanari Koguchi, Hiroshi Kakibayashi, Masamitsu Yazawa, Kenji Hiruma, and Toshio Katsuyama. Crystal structure change of GaAs and InAs whiskers from zinc-blende to wurtzite type. *Japanese Journal of Applied Physics*, 31(Part 1, No. 7):2061–2065, jul 1992.

[62] Toru Akiyama, Kosuke Sano, Kohji Nakamura, and Tomonori Ito. An empirical potential approach to wurtzite-zinc-blende polytypism in group III-v semiconductor nanowires. *Japanese Journal of Applied Physics*, 45(No. 9):L275–L278, feb 2006.

[63] S. Breue. *Molecular Beam Epitaxy of GaAs Nanowires and their Suitability for Optoelectronic Applications*. PhD thesis, Humboldt-Universität zu Berlin, 2011.

[64] Torsten Rieger, Mihail Ion Lepsa, Thomas Schäpers, and Detlev Grützmacher. Controlled wurtzite inclusions in self-catalyzed zinc blende III–v semiconductor nanowires. *Journal of Crystal Growth*, 378:506–510, sep 2013.

[65] Jonas Johansson, Lisa S. Karlsson, Kimberly A. Dick, Jessica Bolinsson, Brent A. Wacaser, Knut Deppert, and Lars Samuelson. Effects of supersaturation on the crystal structure of gold seeded III-v nanowires. *Crystal Growth & Design*, 9(2):766–773, feb 2009.

[66] Peter Krogstrup, Stefano Curiotto, Erik Johnson, Martin Aagesen, Jesper Nygård, and Dominique Chatain. Impact of the liquid phase shape on the structure of III-v nanowires. *Physical Review Letters*, 106(12), mar 2011.

[67] Frank Glas, Jean-Christophe Harmand, and Gilles Patriarche. Why does wurtzite form in nanowires of III-v zinc blende semiconductors? *Physical Review Letters*, 99(14), oct 2007.

[68] Steffen Breuer, Lou-Fé Feiner, and Lutz Geelhaar. Droplet bulge effect on the formation of nanowire side facets. *Crystal Growth & Design*, 13(7):2749–2755, jun 2013.

[69] V. G. Dubrovskii, N. V. Sibirev, G. E. Cirlin, I. P. Soshnikov, W. H. Chen, R. Larde, E. Cadel, P. Pareige, T. Xu, B. Grandidier, J.-P. Nys, D. Stievenard, M. Moewe, L. C. Chuang, and C. Chang-Hasnain. Gibbs-thomson and diffusion-induced contributions to the growth rate of si, InP, and GaAs nanowires. *Physical Review B*, 79(20), may 2009.

[70] Frank Glas, Jean-Christophe Harmand, and Gilles Patriarche. Nucleation antibunching in catalyst-assisted nanowire growth. *Physical Review Letters*, 104(13), mar 2010.

[71] Frank Glas, Mohammed Reda Ramdani, Gilles Patriarche, and Jean-Christophe Harmand. Predictive modeling of self-catalyzed III-v nanowire growth. *Physical Review B*, 88(19), nov 2013.

[72] M. Piccin, G. Bais, V. Grillo, F. Jabeen, S. De Franceschi, E. Carlino, M. Lazzarino, F. Romanato, L. Businaro, S. Rubini, F. Martelli, and A. Franciosi. Growth by molecular beam epitaxy and electrical characterization of GaAs nanowires. *Physica E: Low-dimensional Systems and Nanostructures*, 37(1-2):134–137, mar 2007.

[73] Joseph Dufouleur, Carlo Colombo, Tonko Garma, Bernt Ketterer, Emanuele Uccelli, Marco Nicotra, and Anna Fontcuberta i Morral. P-doping mechanisms in catalyst-free gallium arsenide nanowires. *Nano Letters*, 10(5):1734–1740, may 2010.

[74] G. E. Cirlin, A. D. Bouravleuv, I. P. Soshnikov, Yu. B. Samsonenko, V. G. Dubrovskii, E. M. Arakcheeva, E. M. Tanklevskaya, and P. Werner. Photovoltaic properties of p-doped GaAs nanowire arrays grown on n-type GaAs(111)b substrate. *Nanoscale Research Letters*, 5(2):360–363, nov 2009.

[75] M. Hilse, M. Ramsteiner, S. Breuer, L. Geelhaar, and H. Riechert. Incorporation of the dopants si and be into GaAs nanowires. *Applied Physics Letters*, 96(19):193104, may 2010.

[76] R. J. Malik. Doping limits of c, be, and si in GaAs grown by solid source molecular-beam epitaxy with a thermally cracked as2 source. *Journal of Vacuum Science & Technology B: Microelectronics and Nanometer Structures*, 10(2):850, mar 1992.

[77] Alberto Casadei, Peter Krogstrup, Martin Heiss, Jason A. Röhr, Carlo Colombo, Thibaud Ruelle, Shivendra Upadhyay, Claus B. Sørensen, Jesper Nygård, and Anna Fontcuberta i Morral. Doping incorporation paths in catalyst-free be-doped GaAs nanowires. *Applied Physics Letters*, 102(1):013117, jan 2013.

[78] M. Ilegems. Beryllium doping and diffusion in molecular-beam epitaxy of GaAs and AlxGa1-xAs. *Journal of Applied Physics*, 48(3):1278–1287, mar 1977.

[79] Kazuya Masu, Makoto Konagai, and Kiyoshi Takahashi. Diffusion of beryllium into GaAs during liquid phase epitaxial growth ofp-ga0.2al0.8as. *Journal of Applied Physics*, 54(3):1574–1578, mar 1983.

[80] D. T. J. Hurle. A thermodynamic analysis of native point defect and dopant solubilities in zinc-blende III–v semiconductors. *Journal of Applied Physics*, 107(12):121301, jun 2010.

[81] Georg Alefeld and Johann Völkl, editors. *Hydrogen in Metals I*. Springer Berlin Heidelberg, 1978.

[82] Yu Diao, Lei Liu, and Sihao Xia. Exploration the p-type doping mechanism of GaAs nanowires from first-principles study. *Physics Letters A*, 383(2-3):202–209, jan 2019.

[83] N Isik Goktas, E M Fiordaliso, and R R LaPierre. Doping assessment in GaAs nanowires. *Nanotechnology*, 29(23):234001, apr 2018.

[84] Thomas Gniiupel-HeroldlJ, P. C. Brand, and H. Prask. Accessing the elastic properties of cubic materials with diffraction methods.

[85] M. Eckert. Max von laue and the discovery of x-ray diffraction in 1912. *Annalen der Physik*, 524(5):A83–A85, may 2012.

[86] Michael Eckert. Disputed discovery: the beginnings of x-ray diffraction in crystals in 1912 and its repercussionsThis laue centennial article has also been published inZeitschrift für kristallographie[eckert (2012).z. kristallogr.227, 27–35]. *Acta Crystallographica Section A Foundations of Crystallography*, 68(1):30–39, dec 2011.

[87] B. E. Warren. *X-Ray Diffraction*. Dover Publications Inc., 1990.

[88] Andreas Biermanns, Anton Davydok, Hendrik Paetzelt, Ana Diaz, Volker Gottschalch, Till Hartmut Metzger, and Ullrich Pietsch. Individual GaAs nanorods imaged by coherent x-ray diffraction. *Journal of Synchrotron Radiation*, 16(6):796–802, sep 2009.

[89] D.W. Hogan and D.J. Dyson. Angles between planes in the hexagonal and tetragonal crystal systems. *Micron (1969)*, 2(1):59–61, jan 1970.

[90] Jens Als-Nielsen Des Mcmorrow. *Elements of Modern X-Ray Physics*. WILEY, 2011.

[91] Martin Schmidbauer. *X-Ray Diffuse Scattering from Self-Organized Mesoscopic Semiconductor Structures*. Springer Berlin Heidelberg, 2004.

[92] A. Guinier. *X-Ray Diffraction: In Crystals, Imperfect Crystals, and Amorphous Bodies*. Dover Books on Physics Series. Dover Publications, Incorporated, 2013.

[93] Julian Stangl, Cristian Mocuta, Virginie Chamard, and Dina Carbone. *Nanobeam X-Ray Scattering*. Wiley VCH Verlag GmbH, 2013.

[94] E. Prince. *International Tables for Crystallography, Volume C, 3rd Edition, Mathematical, Physical and Chemical Tables*. Wiley, 2004.

[95] I A Vartanyants and I K Robinson. Partial coherence effects on the imaging of small crystals using coherent x-ray diffraction. *Journal of Physics: Condensed Matter*, 13(47):10593–10611, nov 2001.

[96] Ulrich Pietsch, Vaclav Holy, and Tilo Baumbach. *High-Resolution X-Ray Scattering*. Springer-Verlag GmbH, 2004.

[97] G. J. Williams, M. A. Pfeifer, I. A. Vartanyants, and I. K. Robinson. Three-dimensional imaging of microstructure in au nanocrystals. *Physical Review Letters*, 90(17), apr 2003.

[98] T. W. Cornelius, D. Carbone, V. L. R. Jacques, T. U. Schülli, and T. H. Metzger. Three-dimensional diffraction mapping by tuning the x-ray energy. *Journal of Synchrotron Radiation*, 18(3):413–417, mar 2011.

[99] Max Born, Emil Wolf, A. B. Bhatia, P. C. Clemmow, D. Gabor, A. R. Stokes, A. M. Taylor, P. A. Wayman, and W. L. Wilcock. *Principles of Optics*. Cambridge University Press, October 1999.

[100] Paul Kirkpatrick and A. V. Baez. Formation of optical images by x-rays. *Journal of the Optical Society of America*, 38(9):766, sep 1948.

[101] A. Snigirev. The recent development of bragg–fresnel crystal optics. experiments and applications at the ESRF (invited). *Review of Scientific Instruments*, 66(2):2053–2058, feb 1995.

[102] A. A. Minkevich, M. Gailhanou, J.-S. Micha, B. Charlet, V. Chamard, and O. Thomas. Inversion of the diffraction pattern from an inhomogeneously strained crystal using an iterative algorithm. *Physical Review B*, 76(10), sep 2007.

[103] P. Godard, G. Carbone, M. Allain, F. Mastropietro, G. Chen, L. Capello, A. Diaz, T.H. Metzger, J. Stangl, and V. Chamard. Three-dimensional high-resolution quantitative microscopy of extended crystals. *Nature Communications*, 2(1), sep 2011.

[104] Arman Davtyan, Andreas Biermanns, Otmar Loffeld, and Ullrich Pietsch. Coherent x-ray diffraction from single nanowires. *Acta Crystallographica Section A Foundations of Crystallography*, 69(a1):s148–s148, aug 2013.

[105] Jianwei Miao, Pambos Charalambous, Janos Kirz, and David Sayre. Extending the methodology of x-ray crystallography to allow imaging of micrometre-sized non-crystalline specimens. *Nature*, 400(6742):342–344, jul 1999.

[106] I. K. Robinson, I. A. Vartanyants, G. J. Williams, M. A. Pfeifer, and J. A. Pitney. Reconstruction of the shapes of gold nanocrystals using coherent x-ray diffraction. *Physical Review Letters*, 87(19), oct 2001.

[107] F. Lauraux, T. W. Cornelius, S. Labat, M.-I. Richard, S. J. Leake, T. Zhou, O. Kovalenko, E. Rabkin, T. U. Schülli, and O. Thomas. Multi-wavelength bragg coherent x-ray diffraction imaging of au particles. *Journal of Applied Crystallography*, 53(1):170–177, feb 2020.

[108] Tobias U. Schülli and Steven J. Leake. X-ray nanobeam diffraction imaging of materials. *Current Opinion in Solid State and Materials Science*, 22(5):188–201, oct 2018.

[109] Kathryn Grandfield and Håkan Engqvist. Focused ion beam in the study of biomaterials and biological matter. *Advances in Materials Science and Engineering*, 2012:1–6, 2012.

[110] Dermot Brabazon. Nanocharacterization techniques for dental implant development. In *Emerging Nanotechnologies in Dentistry*, pages 327–354. Elsevier, 2018.

[111] David M. Wright, John J. Rickard, Nigel H. Kyle, Tevor G. Gard, Harald Dobberstein, Michael Motskin, Athene M. Donald, and Jeremy N. Skepper. The use of dual beam ESEM FIB to reveal the internal ultrastructure of hydroxyapatite nanoparticle-sugar-glass composites. *Journal of Materials Science: Materials in Medicine*, 20(1):203–214, aug 2008.

[112] Sergio Lozano-Perez. A guide on FIB preparation of samples containing stress corrosion crack tips for TEM and atom-probe analysis. *Micron*, 39(3):320–328, apr 2008.

[113] S. Lipp, L. Frey, C. Lehrer, E. Demm, S. Pauthner, and H. Ryssel. A comparison of focused ion beam and electron beam induced deposition processes. *Microelectronics Reliability*, 36(11-12):1779–1782, nov 1996.

[114] Nan Yao, editor. *Focused Ion Beam Systems*. Cambridge University Press, 2007.

[115] V. G. M. SIVEL, J. VAN DEN BRAND, W. R. WANG, H. MOHDADI, F. D. TICHELAAR, P. F. A. ALKEMADE, and H. W. ZANDBERGEN. Application of the dual-beam FIB/SEM to metals research. *Journal of Microscopy*, 214(3):237–245, jun 2004.

[116] Terunobu Akiyama, Nicolaas F. de Rooij, Urs Staufer, Manfred Detterbeck, Dominik Braendlin, Simon Waldmeier, and Martin Scheidiger. Implementation and characterization of a quartz tuning fork based probe consisted of discrete resonators for dynamic mode atomic force microscopy. *Review of Scientific Instruments*, 81(6):063706, jun 2010.

[117] T. Akiyama, U. Staufer, N. F. de Rooij, P. Frederix, and A. Engel. Symmetrically arranged quartz tuning fork with soft cantilever for intermittent contact mode atomic force microscopy. *Review of Scientific Instruments*, 74(1):112–117, jan 2003.

[118] M. M. J. Treacy, T. W. Ebbesen, and J. M. Gibson. Exceptionally high young's modulus observed for individual carbon nanotubes. *Nature*, 381(6584):678–680, jun 1996.

[119] P. Poncharal. Electrostatic deflections and electromechanical resonances of carbon nanotubes. *Science*, 283(5407):1513–1516, mar 1999.

[120] T. Barois, S. Perisanu, P. Poncharal, P. Vincent, S. T. Purcell, and A. Ayari. Quality-factor enhancement of nanoelectromechanical systems by capacitive driving beyond resonance. *Physical Review Applied*, 6(1), jul 2016.

[121] A. Descombin, S. Perisanu, P. Poncharal, P. Vincent, S. T. Purcell, and A. Ayari. Sensing and cooling of a nanomechanical resonator with an electron beam stimulated internal feedback and a capacitive force. *Journal of Applied Physics*, 124(6):064304, aug 2018.

[122] P. Vincent, A. Descombin, S. Dagher, T. Seoudi, A. Lazarus, O. Thomas, A. Ayari, S. T. Purcell, and S. Perisanu. Nonlinear polarization coupling in freestanding nanowire/nanotube resonators. *Journal of Applied Physics*, 125(4):044302, jan 2019.

[123] Yujie Chen, Tim Burgess, Xianghai An, Yiu-Wing Mai, H. Hoe Tan, Jin Zou, Simon P. Ringer, Chennupati Jagadish, and Xiaozhou Liao. Effect of a high density of stacking faults on the young's modulus of GaAs nanowires. *Nano Letters*, 16(3):1911–1916, feb 2016.

[124] Yujie Chen, Qiang Gao, Yanbo Wang, Xianghai An, Xiaozhou Liao, Yiu-Wing Mai, H. Hoe Tan, Jin Zou, Simon P. Ringer, and Chennupati Jagadish. Determination of young's modulus of ultrathin nanomaterials. *Nano Letters*, 15(8):5279–5283, jul 2015.

[125] Yan-Bo Wang, Li-Feng Wang, Hannah J. Joyce, Qiang Gao, Xiao-Zhou Liao, Yiu-Wing Mai, Hoe H. Tan, Jin Zou, Simon P. Ringer, Hua-Jian Gao, and Chennupati Jagadish. Super deformability and young's modulus of GaAs nanowires. *Advanced Materials*, 23(11):1356–1360, feb 2011.

[126] Edmund Pickering, Arixin Bo, Haifei Zhan, Xiaozhou Liao, Hark Hoe Tan, and YuanTong Gu. In situ mechanical resonance behaviour of pristine and defective zinc blende GaAs nanowires. *Nanoscale*, 10(5):2588–2595, 2018.

[127] Chang-Yong Nam, Papot Jaroenapibal, Douglas Tham, David E. Luzzi, Stephane Evoy, and John E. Fischer. Diameter-dependent electromechanical properties of GaN nanowires. *Nano Letters*, 6(2):153–158, feb 2006.

[128] Andrew N. Cleland. *Foundations of Nanomechanics*. Springer Berlin Heidelberg, 2002.

[129] DR. P. M. MORSE. Vibration and sound. *Nature*, 163(4137):232–232, feb 1949.

[130] Jerry H. Gindberg Ginsberg. *Mechanical and Structural Vibrations*. John Wiley & Sons, 2001.

[131] Matthias Imboden and Pritiraj Mohanty. Dissipation in nanoelectromechanical systems. *Physics Reports*, 534(3):89–146, jan 2014.

[132] T. Rocheleau, T. Ndukum, C. Macklin, J. B. Hertzberg, A. A. Clerk, and K. C. Schwab. Preparation and detection of a mechanical resonator near the ground state of motion. *Nature*, 463(7277):72–75, dec 2009.

[133] A. Naik, O. Buu, M. D. LaHaye, A. D. Armour, A. A. Clerk, M. P. Blencowe, and K. C. Schwab. Cooling a nanomechanical resonator with quantum back-action. *Nature*, 443(7108):193–196, sep 2006.

[134] C. Zener, W. Otis, and R. Nuckolls. Internal friction in solids III. experimental demonstration of thermoelastic internal friction. *Physical Review*, 53(1):100–101, jan 1938.

[135] M. C. Cross and Ron Lifshitz. Elastic wave transmission at an abrupt junction in a thin plate with application to heat transport and vibrations in mesoscopic systems. *Physical Review B*, 64(8), aug 2001.

[136] P.-L. Yu, T. P. Purdy, and C. A. Regal. Control of material damping in high-QMembrane microresonators. *Physical Review Letters*, 108(8), feb 2012.

[137] I. Wilson-Rae. Intrinsic dissipation in nanomechanical resonators due to phonon tunneling. *Physical Review B*, 77(24), jun 2008.

[138] Douglas M. Photiadis and John A. Judge. Attachment losses of high q oscillators. *Applied Physics Letters*, 85(3):482–484, jul 2004.

[139] B. S. Berry. Mechanical relaxation behavior of hydrogenated metallic glasses, in g. bombakidis and r.c. bowman (eds.), hydrogen in disordered and amorphous solids. *Plenum Publishing Corporation (1986) pp. 215-236*, 1986.

[140] T. Barois, A. Ayari, A. Siria, S. Perisanu, P. Vincent, P. Poncharal, and S. T. Purcell. Ohmic electromechanical dissipation in nanomechanical cantilevers. *Physical Review B*, 85(7), feb 2012.

[141] Genziana Bussone, Emmanouil Dimakis, Raphael Grifone, Andreas Biermanns, Abbes Tahraoui, Dina Carbone, Lutz Geelhaar, Tobias U. Schülli, and Ullrich Pietsch. Impact of strain induced by polymer curing in benzocyclobutene embedded semiconductor nanostructures. *physica status solidi (RRL) - Rapid Research Letters*, 8(12):1007–1010, sep 2014.

[142] R. Modlinski. Creep as a reliability problem in MEMS. *Microelectronics Reliability*, 44(9-11):1733–1738, sep 2004.

[143] W Merlijn van Spengen. MEMS reliability from a failure mechanisms perspective. *Microelectronics Reliability*, 43(7):1049–1060, jul 2003.

[144] Clarence Zener. *Elasticity and Anelasticity of Metals*. 1956.

[145] Arthur S. Nowick and B. S. Berry. *Anelastic Relaxation in Crystalline Solids*. Academic Press, 1972.

[146] Huaping Sheng, He Zheng, Fan Cao, Shujing Wu, Lei Li, Chun Liu, Dongshan Zhao, and Jianbo Wang. Anelasticity of twinned CuO nanowires. *Nano Research*, 8(11):3687–3693, sep 2015.

[147] Yasuro Ikuma and Ronald S. Gordon. Effects of anelastic deformation on high-temperature stress relaxation of polycrystalline MgO and al2o3. *Journal of Materials Science*, 17(4):1066–1078, apr 1982.

[148] D. Nagarajan. Anelasticity in cast mg-gd alloys. *Materials Science and Engineering: A*, 695:14–19, may 2017.

[149] L. David, R. Quinson, C. Gauthier, and J. Perez. The role of anelasticity in high stress mechanical response and physical properties of glassy polymers. *Polymer Engineering & Science*, 37(10):1633–1640, oct 1997.

[150] L. Lu. Ultrahigh strength and high electrical conductivity in copper. *Science*, 304(5669):422–426, apr 2004.

[151] Guangming Cheng, Chunyang Miao, Qingquan Qin, Jing Li, Feng Xu, Hamed Haftbaradaran, Elizabeth C. Dickey, Huajian Gao, and Yong Zhu. Large anelasticity and associated energy dissipation in single-crystalline nanowires. *Nature Nanotechnology*, 10(8):687–691, jul 2015.

[152] G. Schaumann, J. Völki, and G. Alefeld. The diffusion coefficients of hydrogen and deuterium in vanadium, niobium, and tantalum by gorsky-effect measurements. *physica status solidi (b)*, 42(1):401–413, 1970.

[153] G. Schaumann, J. Völkl, and G. Alefeld. Relaxation process due to long-range diffusion of hydrogen and deuterium in niobium. *Physical Review Letters*, 21(13):891–893, sep 1968.

[154] Etienne Navarro. Python code for mechanical digital image correlation (dic). https://github.com/xdze2/stretchablecorr, 2020.

[155] Stéphane Labat, Marie-Ingrid Richard, Maxime Dupraz, Marc Gailhanou, Guillaume Beutier, Marc Verdier, Francesca Mastropietro, Thomas W. Cornelius, Tobias U. Schülli, Joël Eymery, and Olivier Thomas. Inversion domain boundaries in GaN wires revealed by coherent bragg imaging. *ACS Nano*, 9(9):9210–9216, sep 2015.

[156] Ali Al Hassan, Jonas Lähnemann, Arman Davtyan, Mahmoud Al-Humaidi, Jesús Herranz, Danial Bahrami, Taseer Anjum, Florian Bertram, Arka Bikash Dey, Lutz Geelhaar, and Ullrich Pietsch. Beam damage of single semiconductor nanowires during x-ray nanobeam diffraction experiments. *Journal of Synchrotron Radiation*, 27(5):1200–1208, aug 2020.

Acronyms

AC Alternating Current

AFM Atomic Force Microscopy

BC Boundary Conditions

BCC body-Centred Cubic

BCDI Bragg Coherent X-rays Diffraction Imaging

BSE Back Scattered Electrons

CRL Compound Refractive Lenses

CTRs Crystal Truncation Rods

DC Direct Current

DIC Digital image correlation

EDX Energy-dispersive X-ray spectroscopy

FCC Face-Centred Cubic

FEM Finite Element Method

FFT Fast Fourier Transformation

FIB Focused Ion Beam

FWHM Full Width at Half Maximum

IFT Inverse Fourier Transformation

LMIS Liquid Metal Ion Source

MBE Molecular Beam Epitaxy

MEMS Micro-electromechincal systems

MNaF Micro-and Nanoanalytics Facility

MOVPE metal-organic vapor phase epitaxy

NEMS Nano-electromechincal systems

NW Nanowire

NWs Nanowires

nXRD Nano X-rays Diffraction

PDE Partial Differential Equations

QF Quality Factor

RSM Reciprocal space mapping

SA selective area growth

SE Secondary Electrons

SEM Scanning Electron Microscopy

SF Stacking faults

SFINX Scanning Force Microscope for in situ Nanofocused X-ray diffraction

SXDM Scanning x-ray diffraction microscopy

TED Thermo-elastic damping

TEM Transmission Electron Microscopy

TZB twinned zinc-blende

UHV ultra high vacuum

VLS vapor-liquid-solid mechanism

WZ wurtzite crystal structure

XRD X-rays Diffraction

ZB zinc-blende crystal structure